Project:

opticAlly puMped mAgnetometers foR EarTh observaTiOn (AMARETTO)

Title:

Final report

DOCUMENT N°	:	**AMA.CSE.TN.0002**
ISSUE	:	**1/2**
DATE	:	**31.08.2025**
CSEM PROJECT N°	:	**271-ES.2935**
CONTRACT N°	:	**4000145835/24/NL/FFi**
AUTHORS°	:	**S. KARLEN, E. BATORI (CSEM)** **G. KERVALISHVILI, M. KORTE, I. MICHAELIS, M. ROTHER (GFZ)** **M. MITCHELL, A. SIERANT, C. KIEHL, D. MENDEZ-AVALOS (ICFO)**

MODIFICATION LIST

ISSUE	DATE	PAGES	MODIFICATIONS
1/0	25.07.2025	All	1st draft
1/1	31.08.2025	All	Initial version
1/2	19.09.2025	All	As per FR RID

DISTRIBUTION LIST

COMPANY	NAME	FORMAT
ESA	A. Strangfeld	pdf
CSEM	Authors	pdf
ICFO	Authors	pdf
GFZ	Authors	pdf

TABLE OF FIGURES

TABLE OF TABLES

SCOPE OF THE DOCUMENT

This document is the mid-term review report of the AMARETTO project which goal is to study the potential of new OPM sensor technologies for magnetic field measurement in the frame of scientific earth observation. It contains the technical output of the two first tasks of the project: the state-of-the-art review of the OPM technology (WP110) and of scientific spaceborne earth observation magnetometry (WP120)and the sensor requirement definition (WPs 210, 220 and 230).

ABBREVIATIONS

ACRONYM	MEANING
AMARETTO	opticAlly puMped mAgnetometers foR EarTh observaTiOn
AMPERE	Active Magnetosphere and Planetary Electrodynamics Response Experiment
AOCS	Attitude and Orbit Control System
ASM	Absolute Scalar Magnetometer
ASIC	Application Specific Integrated Circuit
BOA	Booster Optical Amplifier
CHAMP	Challenging Mini-Satellite Payload
CME	Coronal Mass Ejection
CPT	Coherent Population Trapping
CSC	Compact Spherical Coil
DAC	Digital to Analog Converter
EEJ	Equatorial Electrojet
EIT	Electromagnetically Induced Transparency
ESA	European Space Agency
FAC	Field-Aligned Current
FID	Free Induction Decay
FPGA	Field Programmable Gate Array
HFD	High frequency discharge
HFS	Hyper-Fine Structure
HK	Housekeeping data
IHFAC	Inter-Hemispheric FAC
LEO	Low Earth Orbit
ML	Machine Learning
mW	microwave
NASA	National Aeronautics and Space Administration
NLZ	Nonlinear Zeeman
NMOR	Nonlinear Magneto-Optical Rotation
NR	Not reported
OGO	Orbiting Geophysical Observatories
OPM	Optically Pumped Magnetometer
OVM	Overhauser Magnetometer

ACRONYM	MEANING
POGO	Polar OGO
RC	Ring Current
RQS	Requirement Scalar
RQV	Requirement Vector
SAC-C	Satellite de Aplicaciones Cientifico-C
S/C	Spacecraft
SERF	Spin Exchange Relaxation-Free
SOA	Semiconductor Optical Amplifier
SSO	Sun-Synchronous Orbit
Sq	Solar quiet
SV	Secular Variation
SWaP	Size, Weight and Power
TEC	Total Electron Content
TBC	To Be Confirmed
TBD	To Be Defined
TIA	Trans-Impedance Amplifier
VCSEL	Vertical-Cavity Surface-Emitting Laser
VFM	Vector Field Magnetometer

APPLICABLE DOCUMENTS

Applicable Documents		
Doc. Id.	**Document Nr.**	**Document Title**
[AD 1]	ECSS-E-ST-10-03	Space engineering - Testing
[AD 2]	ECSS-E-ST-10-12C	Methods for the calculation of radiation received and its effects, and a policy for design margins

REFERENCE DOCUMENTS

Acosta, V., Ledbetter, M. P., Rochester, S. M., Budker, D., Kimball, D. F. J., Hovde, D. C., Gawlik, W., Pustelny, S., Zachorowski, J., & Yashchuk, V. V. (2006). Nonlinear magneto-optical rotation with frequency-modulated light in the geophysical field range. *Physical Review A - Atomic, Molecular, and Optical Physics*, *73*(5). https://doi.org/10.1103/PhysRevA.73.053404

Acosta, V. M., Auzinsh, M., Gawlik, W., Grisins, P., Higbie, J. M., Kimball, D. F. J., Krzemien, L., Ledbetter, M. P., Pustelny, S., Rochester, S. M., Yashchuk, V. V., & Budker, D. (2007). *Production and detection of atomic hexadecapole at Earth's magnetic field*. https://doi.org/10.1364/OE.16.011423

Afach, S., Ban, G., Bison, G., Bodek, K., Chowdhuri, Z., Grujić, Z. D., Hayen, L., Hélaine, V., Kasprzak, M., Kirch, K., Knowles, P., Koch, H.-C., Komposch, S., Kozela, A., Krempel, J., Lauss, B., Lefort, T., Lemière, Y., Mtchedlishvili, A., … Zsigmond, G. (2015a). Highly stable atomic vector magnetometer based on free spin precession. *Optics Express*, *23*(17), 22108. https://doi.org/10.1364/oe.23.022108

Afach, S., Ban, G., Bison, G., Bodek, K., Chowdhuri, Z., Grujić, Z. D., Hayen, L., Hélaine, V., Kasprzak, M., Kirch, K., Knowles, P., Koch, H.-C., Komposch, S., Kozela, A., Krempel, J., Lauss, B., Lefort, T., Lemière, Y., Mtchedlishvili, A., … Zsigmond, G. (2015b). Highly stable atomic vector magnetometer based on free spin precession. *Optics Express*, *23*(17), 22108. https://doi.org/10.1364/oe.23.022108

Aleksandrov, E. B., Vershovskiĭ, A. K., & Pazgalev, A. S. (2006). Magnetometer based on a pair of symmetric transitions in the 87 Rb hyperfine structure. *Technical Physics*, *51*(7), 919–923. https://doi.org/10.1134/S1063784206070176

Alem, O., Benison, A. M., Barth, D. S., Kitching, J., & Knappe, S. (2014). Magnetoencephalography of Epilepsy with a Microfabricated Atomic Magnetrode. *The Journal of Neuroscience*, *34*(43), 14324–14327. https://doi.org/10.1523/JNEUROSCI.3495-14.2014

Alexandrov, E. B. (2003). Recent Progress in Optically Pumped Magnetometers. *Physica Scripta*, *T105*(1), 27. https://doi.org/10.1238/Physica.Topical.105a00027

Alexandrov, E. B., Balabas, M. V., Kulyasov, V. N., Ivanov, A. E., Pazgalev, A. S., Rasson, J. L., Vershovski, A. K., & Yakobson, N. N. (2004). Three-component variometer based on a scalar potassium sensor. *Measurement Science and Technology*, *15*(5), 918–922. https://doi.org/10.1088/0957-0233/15/5/020

Algarra, P., Domínguez, I., Nieto, J., Fayos, J., Wilkinson, J., Cornwall, T., Leger, J.-M., & Jager, T. (2023). *NanoMagSsat deployable amagnetic boom*. https://cea.hal.science/cea-04304161

Alken, P., Olsen, N., & Finlay, C. C. (2020). Co-estimation of geomagnetic field and in-orbit fluxgate magnetometer calibration parameters. *Earth, Planets and Space*, *72*(1), 49. https://doi.org/10.1186/s40623-020-01163-9

Alldredge, L. R. (1960). A proposed automatic standard magnetic observatory. *Journal of Geophysical Research*, *65*(11), 3777–3786. https://doi.org/10.1029/JZ065i011p03777

Anderson, B. J., Takahashi, K., & Toth, B. A. (2000). Sensing global Birkeland currents with iridium® engineering magnetometer data. *Geophysical Research Letters*, *27*(24), 4045–4048. https://doi.org/10.1029/2000gl000094

Andryushkov, V., Radnatarov, D., & Kobtsev, S. (2022). Vector magnetometer based on the effect of coherent population trapping. *Applied Optics*, *61*(13), 3604. https://doi.org/10.1364/ao.457087

Auster, H. U., Glassmeier, K. H., Magnes, W., Aydogar, O., Baumjohann, W., Constantinescu, D., Fischer, D., Fornacon, K. H., Georgescu, E., Harvey, P., Hillenmaier, O., Kroth, R., Ludlam, M., Narita, Y., Nakamura, R., Okrafka, K., Plaschke, F., Richter, I., Schwarzl, H., … Wiedemann, M. (2009). The THEMIS Fluxgate Magnetometer. In *The THEMIS Mission* (pp. 235–264). Springer New York. https://doi.org/10.1007/978-0-387-89820-9_11

Auzinsh, M., Budker, D., Kimball, D. F., Rochester, S. M., Stalnaker, J. E., Sushkov, A. O., & Yashchuk, V. V. (2004). Can a Quantum Nondemolition Measurement Improve the Sensitivity of an Atomic Magnetometer? *Physical Review Letters*, *93*(17), 173002. https://doi.org/10.1103/PhysRevLett.93.173002

Baerenzung, J., Holschneider, M., Saynish-Wagner, J., & Thomas, M. (2022). Kalmag: A high spatio-temporal model of the geomagnetic feld. *Earth Planets and Space*, *74, 139*. https://doi.org/10.1186/s40623-022-01692-5

Bak, T. (1999). *Spacecraft Attitude Determination; A Magnetometer Approach*.

Balogh, A., Carr, C. M., Acuña, M. H., Acuña, A., Dunlop, M. W., Beek, T. J., Brown, P., Fornacon, K.-H., Georgescu, E., Glassmeier, K.-H., Harris, J., Musmann, G., Oddy, T., & Schwingenschuh, K. (2001). The Cluster Magnetic Field Investigation: overview of in-flight performance and initial results. In *Annales Geophysicae* (Vol. 19).

Baluktsian, T., Urban, C., Bublat, T., Giessen, H., Löw, R., & Pfau, T. (2010). Fabrication method for microscopic vapor cells for alkali atoms. *Optics Letters*, *35*(12), 1950. https://doi.org/10.1364/OL.35.001950

Bao, G., Kanta, D., Antypas, D., Rochester, S., Jensen, K., Zhang, W., Wickenbrock, A., & Budker, D. (2022). All-optical spin locking in alkali-metal-vapor magnetometers. *Physical Review A*, *105*(4). https://doi.org/10.1103/PhysRevA.105.043109

Bao, G., Wickenbrock, A., Rochester, S., Zhang, W., & Budker, D. (2018). Suppression of the Nonlinear Zeeman Effect and Heading Error in Earth-Field-Range Alkali-Vapor Magnetometers. *Physical Review Letters*, *120*(3). https://doi.org/10.1103/PhysRevLett.120.033202

Batori, E., Affolderbach, C., Pellaton, M., Gruet, F., Violetti, M., Su, Y., Skrivervik, A. K., & Mileti, G. (2022). ? POP Clock: A Microcell Atomic Clock Based on a Double-Resonance Ramsey Scheme. *Physical Review Applied*, *18*(5). https://doi.org/10.1103/PhysRevApplied.18.054039

Ben-Kish, A., & Romalis, M. V. (2010). Dead-zone-free atomic magnetometry with simultaneous excitation of orientation and alignment resonances. *Physical Review Letters*, *105*(19). https://doi.org/10.1103/PhysRevLett.105.193601

Bennett, J. S., Vyhnalek, B. E., Greenall, H., Bridge, E. M., Gotardo, F., Forstner, S., Harris, G. I., Miranda, F. A., & Bowen, W. P. (2021). Precision magnetometers for aerospace applications: A review. In *Sensors* (Vol. 21, Issue 16). MDPI. https://doi.org/10.3390/s21165568

Bertrand, F., Jager, T., Boness, A., Fourcault, W., Le Gal, G., Palacios-Laloy, A., Paulet, J., & Léger, J. M. (2021a). A 4He vector zero-field optically pumped magnetometer operated in the Earth-field. *Review of Scientific Instruments*, *92*(10). https://doi.org/10.1063/5.0062791

Bertrand, F., Jager, T., Boness, A., Fourcault, W., Le Gal, G., Palacios-Laloy, A., Paulet, J., & Léger, J. M. (2021b). A 4He vector zero-field optically pumped magnetometer operated in the Earth-field. *Review of Scientific Instruments*, *92*(10). https://doi.org/10.1063/5.0062791

Beverini, N., Carmisciano, C., Alzetta, E., Faggioni, O., Francesconi, F., & Maccioni, E. (1998). A Potassium Vapor Magnetometer Optically Pumped By A Diode Laser. *12th EFTF (European Frequency and Time Forum)*.

Billings, S. D. (2004). Discrimination and classification of buried unexploded ordnance using magnetometry. *IEEE Transactions on Geoscience and Remote Sensing*, *42*(6), 1241–1251. https://doi.org/10.1109/TGRS.2004.826803

Bison, G., Bondar, V., Schmidt-Wellenburg, P., Schnabel, A., & Voigt, J. (2018). Sensitive and stable vector magnetometer for operation in zero and finite fields. *Optics Express*, *26*(13), 17350. https://doi.org/10.1364/oe.26.017350

Bison, G., Wynands, R., & Weis, A. (2003). A laser-pumped magnetometer for the mapping of human cardiomagnetic fields. *Applied Physics B: Lasers and Optics*, *76*(3), 325–328. https://doi.org/10.1007/s00340-003-1120-z

Budker, D., & Romalis, M. (2007). Optical magnetometry. *Nature Physics*, *3*(4), 227–234. https://doi.org/10.1038/nphys566

Bulatowicz, M., Tost, J., & Walker, T. G. (2023). Feedback Methods for Vector Measurements Using an All-Optical Atomic Magnetometer. *Sensors*, *23*(9). https://doi.org/10.3390/s23094263

Canciani, A., & Raquet, J. (2016). Absolute Positioning Using the Earth's Magnetic Anomaly Field. *Navigation, Journal of the Institute of Navigation*, *63*(2), 111–126. https://doi.org/10.1002/navi.138

Canciani, A., & Raquet, J. (2017). Airborne Magnetic Anomaly Navigation. *IEEE Transactions on Aerospace and Electronic Systems*, *53*(1), 67–80. https://doi.org/10.1109/TAES.2017.2649238

Chéron, B., Gilles, H., Hamel, J., Moreau, O., & Noël, E. (1997). Improvement of the Spatial Amplitude Isotropy of a 4He Magnetometer Using a Modulated Pumping Beam. *Journal de Physique III*, *7*(8), 1735–1740. https://doi.org/10.1051/jp3:1997215ï

Clarke, J. (1989). Principles and applications of SQUIDs. *Proceedings of the IEEE*, *77*(8), 1208–1223. https://doi.org/10.1109/5.34120

Coïsson, P., Chauvet, L., Jenner, M., Deborde, R., Hulot, G., Mlynarczyk, J., & Kubisz, J. (2024). 100 000 whistlers detected during ASM burst mode campaigns: uncovering seasonal and solar cycle dependencies. *Swarm 10 Year Anniversary & Science Conference*.

Connerney, J. E. P., Benn, M., Bjarno, J. B., Denver, T., Espley, J., Jorgensen, J. L., Jorgensen, P. S., Lawton, P., Malinnikova, A., Merayo, J. M., Murphy, S., Odom, J., Oliversen, R., Schnurr, R., Sheppard, D., & Smith, E. J. (2017). The Juno Magnetic Field Investigation. In *Space Science Reviews* (Vol. 213, Issues 1–4, pp. 39–138). Springer Netherlands. https://doi.org/10.1007/s11214-017-0334-z

Cutler, T. F., Hamlyn, W. J., Renger, J., Whittaker, K. A., Pizzey, D., Hughes, I. G., Sandoghdar, V., & Adams, C. S. (2020). Nanostructured alkali-metal vapor cells. *Physical Review Applied*, *14*(3). https://doi.org/10.1103/PhysRevApplied.14.034054

Dang, H. B., Maloof, A. C., & Romalis, M. V. (2010). Ultrahigh sensitivity magnetic field and magnetization measurements with an atomic magnetometer. *Applied Physics Letters*, *97*(15). https://doi.org/10.1063/1.3491215

Dantsker, E., Koelle, D., Miklich, A. H., Nemeth, D. T., Ludwig, F., Clarke, J., Longo, J. T., & Vinetskiy, V. (1994). High- *T c* three-axis dc SQUID magnetometer for geophysical applications. *Review of Scientific Instruments*, *65*(12), 3809–3813. https://doi.org/10.1063/1.1145169

Dougherty, M. K., Kellock, S., Southwood, D. J., Balogh, A., Smith, E. J., Tsurutani, B. T., Gerlach, B., Glassmeier, K.-H., Gleim, F., Russell, C. T., Erdos, G., Neubauer, F. M., & Cowley, S. W. H. (2004). The Cassini Magnetic Field Investigation. *Space Science Reviews*, *114*(1–4), 331–383. https://doi.org/10.1007/s11214-004-1432-2

Dunlop, M. W., Tan, X., Zhang, C.-M., Yang, J.-Y., Dong, X.-C., Wei, D., & Xiong, C. (2024). Multi-scale magnetospheric and ground currents from Swarm, Cluster and MMS. *Swarm 10 Year Anniversary & Science Conference*. https://www.swarm-anniversary-and-science.org

Ellmeier, M., Amtmann, C., Pollinger, A., Magnes, W., Hagen, C., Betzler, A., Jernej, I., Agú, M., Windholz, L., & Lammegger, R. (2023). Frequency shift compensation for single and dual laser beam pass sensors of a coherent population trapping resonance based coupled dark state magnetometer. *Measurement: Sensors*, *25*, 100606. https://doi.org/10.1016/j.measen.2022.100606

ESA Mission Experts Division. (2006). *ESA SP-1279(6) – Swarm – The Earth's Magnetic Field and Environment Explorers*.

European Space Agency. (2012, May 29). *CHAMP (Challenging Minisatellite Payload)*. EoPortal.

Fairweather, A. J., & Usher, M. J. (1972). A vector rubidium magnetometer. *Journal of Physics E: Scientific Instruments*, *5*(10), 986–990. https://doi.org/10.1088/0022-3735/5/10/018

Farthing, W. H., & Folz, W. C. (1967). Rubidium vapor magnetometer for near earth orbiting spacecraft. *Review of Scientific Instruments*, *38*(8), 1023–1030. https://doi.org/10.1063/1.1720960

Finlay, C. C., Velímský, J., Kloss, C., & Blangsbøll, R. M. (2024). Satellite monitoring of long period ocean-induced magnetic field variations. *Philosophical Transactions of the Royal Society A: Mathematical, Physical and Engineering Sciences*, *382*(2286), 20240077. https://doi.org/10.1098/rsta.2024.0077

Fratter, I., Léger, J. M., Bertrand, F., Jager, T., Hulot, G., Brocco, L., & Vigneron, P. (2016). Swarm Absolute Scalar Magnetometers first in-orbit results. *Acta Astronautica*, *121*, 76–87. https://doi.org/10.1016/j.actaastro.2015.12.025

Friis-Christensen, E., Lühr, H., & Hulot, G. (2006a). Swarm: A constellation to study the Earth's magnetic field. In *Earth Planets Space* (Vol. 58).

Friis-Christensen, E., Lühr, H., & Hulot, G. (2006b). Swarm: A constellation to study the Earth's magnetic field. *Earth, Planets and Space*, *58*(4), 351–358. https://doi.org/10.1186/BF03351933

Geometrics. (n.d.). *MFAM Developer Kit*. Https://Www.Geometrics.Com/Product/Mfam-Developer-Kit/.

Gonzalez Maldonado, M., Rollins, O., Toyryla, A., McKelvy, J. A., Matsko, A., Fan, I., Li, Y., Wang, Y.-J., Kitching, J., Novikova, I., & Mikhailov, E. E. (2024). Sensitivity of a vector atomic magnetometer based on electromagnetically induced transparency. *Optics Express*, *32*(14), 25062. https://doi.org/10.1364/OE.529276

Gravrand, O., Khokhlov, A., Le Mouël, J. L., & Léger, J. M. (2001). On the calibration of a vectorial 4He pumped magnetometer. *Earth, Planets and Space*, *53*(10), 949–958. https://doi.org/10.1186/BF03351692

Grayver, A., Finlay, C. C., & Olsen, N. (2024). Magnetic signals from oceanic tides: new satellite observations and applications. *Philosophical Transactions of the Royal Society A: Mathematical, Physical and Engineering Sciences*, *382*(2286). https://doi.org/10.1098/rsta.2024.0078

Groeger, S., Bison, G., Knowles, P. E., Wynands, R., & Weis, A. (2006). Laser-pumped cesium magnetometers for high-resolution medical and fundamental research. *Sensors and Actuators, A: Physical*, *129*(1-2 SPEC. ISS.), 1–5. https://doi.org/10.1016/j.sna.2005.09.036

Guttin, C., Leger, J., Stoeckel, F., Leger, J. M., & Stoeckel, E. (1994). An isotropic earth field scalar magnetometer using optically pumped helium 4. *Journal de Physique IV Proceedings*, *111*(C4), 1994. https://doi.org/10.1051/jp4:19944174ï

Haesler, J., Balet, L., Karlen, S., Overstolz, T., Gallinet, B., Lecomte, S., Droz, F., Kautio, K., Karioja, P., & Lahti, M. (2017). Ceramic based flat form factor miniature atomic clock physics package (C-MAC). *6th International Colloquium on Scientific and Fundamental Aspects of GNSS / Galileo*.

Heppner, J. P., Ness, N. F., Scearce, C. S., & Skillman, T. L. (1963). Explorer 10 magnetic field measurements. *Journal of Geophysical Research*, *68*(1), 1–46. https://doi.org/10.1029/JZ068i001p00001

Hewatt, D. P., Ellmeier, M., Kiehl, C., Menon, T. S., Pollock, J. W., Regal, C. A., & Knappe, S. (2024). *Investigating the hyperfine systematic error and relative phase in low spin-polarization alkali FID magnetometers*. http://arxiv.org/abs/2408.00898

Holme, R., James, M. A., & Lühr, H. (2005). Magnetic field modelling from scalar-only data: Resolving the Backus effect with the equatorial electrojet. *Earth, Planets and Space*, *57*(12), 1203–1209. https://doi.org/10.1186/BF03351905

Horrom, T., Singh, R., Dowling, J. P., & Mikhailov, E. E. (2012). Quantum-enhanced magnetometer with low-frequency squeezing. *Physical Review A*, *86*(2), 23803. https://doi.org/10.1103/PhysRevA.86.023803

Hulot, G., Léger, J. M., Jager, F. D. amd T., Clausen, L. B. N., Jørgensen, J. L., Nieto, P., Coïsson, P., Chauvet, L., & Ijssel, J. van den. (2024). *Latest News on NanoMagSat, the Big Picture*.

Hulot, G., Vigneron, P., Léger, J.-M., Fratter, I., Olsen, N., Jager, T., Bertrand, F., Brocco, L., Sirol, O., Lalanne, X., Boness, A., & Cattin, V. (2015). Swarm's absolute magnetometer experimental vector mode, an innovative capability for space magnetometry. *Geophysical Research Letters*, *42*(5), 1352–1359. https://doi.org/https://doi.org/10.1002/2014GL062700

Hunter, D., Dyer, T. E., & Riis, E. (2022). Accurate optically pumped magnetometer based on Ramsey-style interrogation. *Optics Letters*, *47*(5), 1230. https://doi.org/10.1364/ol.449180

Hunter, D., Mrozowski, M. S., McWilliam, A., Ingleby, S. J., Dyer, T. E., Griffin, P. F., & Riis, E. (2023). Optical pumping enhancement of a free-induction-decay magnetometer. *Journal of the Optical Society of America B*, *40*(10), 2664. https://doi.org/10.1364/josab.501086

Ingleby, S., Griffin, P., Dyer, T., Mrozowski, M., & Riis, E. (2022). A digital alkali spin maser. *Scientific Reports*, *12*(1), 12888. https://doi.org/10.1038/s41598-022-16910-z

Ingleby, S. J., O'Dwyer, C., Griffin, P. F., Arnold, A. S., & Riis, E. (2018). Vector Magnetometry Exploiting Phase-Geometry Effects in a Double-Resonance Alignment Magnetometer. *Physical Review Applied*, *10*(3). https://doi.org/10.1103/PhysRevApplied.10.034035

Jager, T., Boness, A., Bertrand, F., & Leger, J.-M. (2024). *ASM status after 10 years of operation on-board the Swarm satellites.*

Jensen, K., Acosta, V. M., Higbie, J. M., Ledbetter, M. P., Rochester, S. M., & Budker, D. (2009). Cancellation of nonlinear Zeeman shifts with light shifts. *Physical Review A - Atomic, Molecular, and Optical Physics*, *79*(2). https://doi.org/10.1103/PhysRevA.79.023406

Karsenty, A. (2020). A comprehensive review of integrated hall effects in macro-, micro-, nanoscales, and quantum devices. In *Sensors (Switzerland)* (Vol. 20, Issue 15, pp. 1–33). MDPI AG. https://doi.org/10.3390/s20154163

Kiehl, C. H. (2024). *Microwave-driven Rabi Magnetometry Implemented in Hot Atomic Vapor*.

Kiehl, C., Menon, T. S., Knappe, S., Thiele, T., & Regal, C. A. (2025). Accurate vector optically pumped magnetometer with microwave-driven Rabi frequency measurements. *Optica*, *12*(1), 77. https://doi.org/10.1364/OPTICA.542502

Knappe, S. A., Hughes, J., & Alem, O. (2023). Microfabricated optically-pumped magnetometers for imaging applications. In S. M. Shahriar & J. Scheuer (Eds.), *Quantum Sensing, Imaging, and Precision Metrology* (p. 29). SPIE. https://doi.org/10.1117/12.2657353

Koch, R. H., & Rozen, J. R. (2001). Low-noise flux-gate magnetic-field sensors using ring- and rod-core geometries. *Applied Physics Letters*, *78*(13), 1897–1899. https://doi.org/10.1063/1.1358852

Korth, H., Strohbehn, K., Tejada, F., Andreou, A. G., Kitching, J., Knappe, S., Lehtonen, S. J., London, S. M., & Kafel, M. (2016). Miniature atomic scalar magnetometer for space based on the rubidium isotope 87Rb. *Journal of Geophysical Research: Space Physics*, *121*(8), 7870–7880. https://doi.org/10.1002/2016JA022389

Kuzmich, A., Mølmer, K., & Polzik, E. S. (1997). Spin Squeezing in an Ensemble of Atoms Illuminated with Squeezed Light. *Physical Review Letters*, *79*(24), 4782–4785. https://doi.org/10.1103/PhysRevLett.79.4782

Langel, R., Ousley, G., & Berbert, J. (1982). THE MAGSAT MISSION. *Geophysical Research Letters*, *9*(4), 243–245.

Ledbetter, M. P., Savukov, I. M., Budker, D., Shah, V., Knappe, S., Kitching, J., Michalak, D. J., Xu, S., & Pines, A. (2008). *Zero-field remote detection of NMR with a microfabricated atomic magnetometer* (Vol. 105, Issue 7). www.pnas.orgcgidoi10.1073pnas.0711505105

Lee, W., Lucivero, V. G., Romalis, M. V., Limes, M. E., Foley, E. L., & Kornack, T. W. (2021). Heading errors in all-optical alkali-metal-vapor magnetometers in geomagnetic fields. *Physical Review A*, *103*(6), 063103. https://doi.org/10.1103/PhysRevA.103.063103

Léger, J. M., Jager, T., Bertrand, F., Hulot, G., Brocco, L., Vigneron, P., Lalanne, X., Chulliat, A., & Fratter, I. (2015). In-flight performance of the Absolute Scalar Magnetometer vector mode on board the Swarm satellites. *Earth, Planets and Space*, *67*(1). https://doi.org/10.1186/s40623-015-0231-1

Léger, J.-M., Bertrand, F., Boness, A., Fourcault, W., Jager, T., Josselin, V., Paulet, J., & Hulot, & G. (2022a). The NanoMagSat Magnetic Payload. *Living Planet Symposium*.

Léger, J.-M., Bertrand, F., Boness, A., Fourcault, W., Jager, T., Josselin, V., Paulet, J., & Hulot, & G. (2022b). The NanoMagSat Magnetic Payload. *Living Planet Symposium*.

Leger, J.-M., Bertrand, F., Jager, T., Prado, M. Le, Fratter, I., & Lalaurie, J.-C. (2009). Swarm Absolute Scalar and Vector Magnetometer Based on Helium 4 Optical Pumping. *Procedia Chemistry*, *1*(1), 634–637. https://doi.org/https://doi.org/10.1016/j.proche.2009.07.158

Li, R., Baynes, F. N., Luiten, A. N., & Perrella, C. (2020). Continuous High-Sensitivity and High-Bandwidth Atomic Magnetometer. *Physical Review Applied*, *14*(6). https://doi.org/10.1103/PhysRevApplied.14.064067

Liang, S.-Q., Yang, G.-Q., Xu, Y.-F., Lin, Q., Liu, Z.-H., & Chen, Z.-X. (2014). Simultaneously improving the sensitivity and absolute accuracy of CPT magnetometer. *Optics Express*, *22*(6), 6837. https://doi.org/10.1364/oe.22.006837

Lieb, G., Jager, T., Palacios-Laloy, A., & Gilles, H. (2019). All-optical isotropic scalar 4He magnetometer based on atomic alignment. *Rev. Sci. Instrum*, *90*, 75104. https://doi.org/10.1063/1.5093533ï

Liew, L.-A., Knappe, S., Moreland, J., Robinson, H., Hollberg, L., & Kitching, J. (2004a). Microfabricated alkali atom vapor cells. *Applied Physics Letters*, *84*(14), 2694–2696.

Liew, L.-A., Knappe, S., Moreland, J., Robinson, H., Hollberg, L., & Kitching, J. (2004b). Microfabricated alkali atom vapor cells. *Applied Physics Letters*, *84*(14), 2694–2696.

Liu, L. Y., Jiang, S. B., Yeh, T. L., Yeh, H. C., Liu, J. Y., Hsu, Y. H., & Peng, J. Y. (2012). The magneto-resistive magnetometer of BCU on the tatiana-2 satellite. *Terrestrial, Atmospheric and Oceanic Sciences*, *23*(3), 317–326. https://doi.org/10.3319/TAO.2011.11.07.01(AA)

Lucivero, V. G., Zanoni, A., Corrielli, G., Osellame, R., & Mitchell, M. W. (2022). Laser-written vapor cells for chip-scale atomic sensing and spectroscopy. *Optics Express*, *30*(15), 27149. https://doi.org/10.1364/oe.469296

Lühr, H., Rother, M., Häusler, K., Fejer, B., & Alken, P. (2012). Direct comparison of nonmigrating tidal signatures in the electrojet, vertical plasma drift and equatorial ionization anomaly. *Journal of Atmospheric and Solar-Terrestrial Physics*, *75–76*, 31–43. https://doi.org/https://doi.org/10.1016/j.jastp.2011.07.009

Mark Prouty. (2016). *Real-Time Hand-Held Magnetometer Array*.

McKelvy, J. A., Maldonado, M. A., Novikova, I., Mikhailov, E. E., & Matsko, A. B. (2023). Technical limits of sensitivity for EIT magnetometry. *Applied Optics*, *62*(24), 6518. https://doi.org/10.1364/ao.497368

Meilleroux, J. L. (1970). Progrès récents sur le magnétomètre à vapeur de césium type « asservi ». *Revue de Physique Appliquée*, *5*(1), 121–130. https://doi.org/10.1051/rphysap:0197000501012100

Meng, X., Zhang, Y., Zhang, X., Jin, S., Wang, T., Jiang, L., Xiao, L., Jia, S., & Xiao, Y. (2023). Machine learning assisted vector atomic magnetometry. *Nature Communications*, *14*(1). https://doi.org/10.1038/s41467-023-41676-x

Merayo, J. é M. G., Jørgensen, J. L., Friis-Christensen, E., Brauer, P., Primdahl, F., Jørgensen, P. S., Allin, T. H., & Denver, T. (2008). The Swarm Magnetometry Package. In *Small Satellites for Earth Observation* (pp. 143–151). Springer Netherlands. https://doi.org/10.1007/978-1-4020-6943-7_13

Merayo, J. M. G., Brauer, P., Primdahl, F., Petersen, J. R., & Nielsen, O. V. (2000). Scalar calibration of vector magnetometers. *Measurement Science and Technology*, *11*(2), 120–132. https://doi.org/10.1088/0957-0233/11/2/304

Michaelis, I., Styp-Rekowski, K., Rauberg, J., Stolle, C., & Korte, M. (2022). Geomagnetic data from the GOCE satellite mission. *Earth, Planets and Space*, *74*(1), 135. https://doi.org/10.1186/s40623-022-01691-6

Murilo, A., Peixoto, P. J. de D., Souza, L. C. G. de, & Lopes, R. V. (2021). Real-time implementation of a parameterized Model Predictive Control for Attitude Control Systems of rigid-flexible satellite. *Mechanical Systems and Signal Processing*, *149*, 107129. https://doi.org/https://doi.org/10.1016/j.ymssp.2020.107129

Nhalil, H., Givon, T., Das, P. T., Hasidim, N., Mor, V., Schultz, M., Amrusi, S., Klein, L., & Grosz, A. (2019). Planar Hall Effect Magnetometer With 5 pT Resolution. *IEEE Sensors Letters*, *3*(12), 1–4. https://doi.org/10.1109/LSENS.2019.2947681

Oelsner, G., Schultze, V., IJsselsteijn, R., & Stolz, R. (2019). Performance analysis of an optically pumped magnetometer in Earth's magnetic field. *EPJ Quantum Technology*, *6*(1). https://doi.org/10.1140/epjqt/s40507-019-0076-9

Oelsner, G., Schultze, V., Ijsselsteijn, R., Wittkämper, F., & Stolz, R. (2019). Sources of heading errors in optically pumped magnetometers operated in the Earth's magnetic field. *Physical Review A*, *99*(1). https://doi.org/10.1103/PhysRevA.99.013420

Olsen, N. (2021). Magnetometer data from the GRACE satellite duo. *Earth, Planets and Space*, *73*(1), 62. https://doi.org/10.1186/s40623-021-01373-9

Olsen, N., Albini, G., Bouffard, J., Parrinello, T., & Tøffner-Clausen, L. (2020). Magnetic observations from CryoSat-2: calibration and processing of satellite platform magnetometer data. *Earth, Planets and Space*, *72*(1), 48. https://doi.org/10.1186/s40623-020-01171-9

Olsen, N., & Stolle, C. (2012). Satellite Geomagnetism. *Annual Review of Earth and Planetary Sciences*, *40*(Volume 40, 2012), 441–465. https://doi.org/https://doi.org/10.1146/annurev-earth-042711-105540

Olsen, N., Tøffner-Clausen, L., Sabaka, T. J., Brauer, P., Merayo, J. M. G., Jørgensen, J. L., Léger, J.-M., Nielsen, O. V, Primdahl, F., & Risbo, T. (2003). Calibration of the Ørsted vector magnetometer. In *Earth Planets Space* (Vol. 55).

Park, J., Stolle, C., Yamazaki, Y., Rauberg, J., Michaelis, I., & Olsen, N. (2020). Diagnosing low-/mid-latitude ionospheric currents using platform magnetometers: CryoSat-2 and GRACE-FO. *Earth, Planets and Space*, *72*(1), 162. https://doi.org/10.1186/s40623-020-01274-3

Park, J., Yamazaki, Y., & Lühr, H. (2020). Latitude dependence of interhemispheric field-aligned currents (IHFACs) as observed by the Swarm constellation. *Journal of Geophysical Research: Space Physics*, *125*, e2019JA027694. https://doi.org/https://doi.org/10.1029/2019JA027694]

Patton, B., Zhivun, E., Hovde, D. C., & Budker, D. (2014). *All-Optical Vector Atomic Magnetometer*. https://doi.org/10.1103/PhysRevLett.113.013001

Petrenko, M. V., Pazgalev, A. S., & Vershovskii, A. K. (2023). All-Optical Nonzero-Field Vector Magnetic Sensor for Magnetoencephalography. *Physical Review Applied*, *20*(2). https://doi.org/10.1103/PhysRevApplied.20.024001

Peyrot, T., Beurthe, Ch., Coumar, S., Roulliay, M., Perronet, K., Bonnay, P., Adams, C. S., Browaeys, A., & Sortais, Y. R. P. (2019). Fabrication and characterization of super-polished wedged borosilicate nano-cells. *Optics Letters*, *44*(8), 1940. https://doi.org/10.1364/ol.44.001940

Pollinger, A., Lammegger, R., Magnes, W., Hagen, C., Ellmeier, M., Jernej, I., Leichtfried, M., Kürbisch, C., Maierhofer, R., Wallner, R., Fremuth, G., Amtmann, C., Betzler, A., Delva, M., Prattes, G., & Baumjohann, W. (2018a). Coupled dark state magnetometer for the China Seismo-Electromagnetic Satellite. *Measurement Science and Technology*, *29*(9). https://doi.org/10.1088/1361-6501/aacde4

Pollinger, A., Lammegger, R., Magnes, W., Hagen, C., Ellmeier, M., Jernej, I., Leichtfried, M., Kürbisch, C., Maierhofer, R., Wallner, R., Fremuth, G., Amtmann, C., Betzler, A., Delva, M., Prattes, G., & Baumjohann, W. (2018b). Coupled dark state magnetometer for the China Seismo-Electromagnetic Satellite. *Measurement Science and Technology*, *29*(9). https://doi.org/10.1088/1361-6501/aacde4

Pustelny, S., Gawlik, W., Rochester, S. M., Kimball, D. F. J., Yashchuk, V. V., & Budker, D. (2006). Nonlinear magneto-optical rotation with modulated light in tilted magnetic fields. *Physical Review A - Atomic, Molecular, and Optical Physics*, *74*(6). https://doi.org/10.1103/PhysRevA.74.063420

Pyragius, T., Florez, H. M., & Fernholz, T. (2018). *A Voigt effect based 3D vector magnetometer*. https://doi.org/10.1103/PhysRevA.100.023416

Raghavan, H., Tayler, M. C. D., Mouloudakis, K., Rae, R., Lähteenmäki, S., Zetter, R., Laine, P., Haesler, J., Balet, L., Overstolz, T., Karlen, S., & Mitchell, M. W. (2024). Functionalized millimeter-scale vapor cells for alkali-metal spectroscopy and magnetometry. *Physical Review Applied*, *22*(4), 044011. https://doi.org/10.1103/PhysRevApplied.22.044011

Rosenzweig, Y., Tokar, D., Shcerback, I., Givon, M., & Folman, R. (2023). *Heading Error Compensation in a Portable Optical Magnetometer Using a Double-Pass Single Beam Configuration*. http://arxiv.org/abs/2307.13982

Rother, M., Korte, M., Morschhauser, A., Vervelidou, F., Matzka, J., & Stolle, C. (2021). The Mag.num core field model as a parent for IGRF-13, and the recent evolution of the South Atlantic Anomaly. *Earth, Planets and Space*, *73*(1). https://doi.org/10.1186/s40623-020-01277-0

Rushton, L. M., Elson, L., Meraki, A., & Jensen, K. (2023). Alignment-Based Optically Pumped Magnetometer Using a Buffer-Gas Cell. *Physical Review Applied*, *19*(6). https://doi.org/10.1103/PhysRevApplied.19.064047

Rutkowski, J., Fourcault, W., Bertrand, F., Rossini, U., Gétin, S., Le Calvez, S., Jager, T., Herth, E., Gorecki, C., Le Prado, M., Léger, J. M., & Morales, S. (2014). Towards a miniature atomic scalar magnetometer using a liquid crystal polarization rotator. *Sensors and Actuators, A: Physical*, *216*, 386–393. https://doi.org/10.1016/j.sna.2014.05.003

Savukov, I. M., Seltzer, S. J., & Romalis, M. V. (2007). Detection of NMR signals with a radio-frequency atomic magnetometer. *Journal of Magnetic Resonance*, *185*(2), 214–220. https://doi.org/10.1016/j.jmr.2006.12.012

Schneider, M., Alken, P., & Chulliat, A. (2018). Modeling the 3-D Geomagnetic Field using Satellite Scalar Field Observations. *AGU Fall Meeting Abstracts*, *2018*, GP21C-0678.

Schwindt, P. D. D., Lindseth, B., Knappe, S., Shah, V., Kitching, J., & Liew, L. A. (2007). Chip-scale atomic magnetometer with improved sensitivity by use of the Mx technique. *Applied Physics Letters*, *90*(8). https://doi.org/10.1063/1.2709532

Seltzer, S. J., Meares, P. J., & Romalis, M. V. (2007). Synchronous optical pumping of quantum revival beats for atomic magnetometry. *Physical Review A - Atomic, Molecular, and Optical Physics*, *75*(5). https://doi.org/10.1103/PhysRevA.75.051407

Seltzer, S. J., & Romalis, M. V. (2004a). Unshielded three-axis vector operation of a spin-exchange-relaxation-free atomic magnetometer. *Applied Physics Letters*, *85*(20), 4804–4806. https://doi.org/10.1063/1.1814434

Seltzer, S. J., & Romalis, M. V. (2004b). Unshielded three-axis vector operation of a spin-exchange-relaxation-free atomic magnetometer. *Applied Physics Letters*, *85*(20), 4804–4806. https://doi.org/10.1063/1.1814434

Sewell, R. J., Koschorreck, M., Napolitano, M., Dubost, B., Behbood, N., & Mitchell, M. W. (2012). Magnetic Sensitivity Beyond the Projection Noise Limit by Spin Squeezing. *Physical Review Letters*, *109*(25), 253605. https://doi.org/10.1103/PhysRevLett.109.253605

Shen, X., Zhang, X., Yuan, S., Wang, L., Cao, J., Huang, J., Zhu, X., Piergiorgio, P., & Dai, J. (2018). The state-of-the-art of the China Seismo-Electromagnetic Satellite mission. *Science China Technological Sciences*, *61*(5), 634–642. https://doi.org/10.1007/s11431-018-9242-0

Soares, G., Yamazaki, Y., Morschhauser, A., Matzka, J., Pinheiro, K. J., Stolle, C., Alken, P., Yoshikawa, A., Hozumi, K., Kulkarni, A., & Supnithi, P. (2022). Using Principal Component Analysis of Satellite and Ground Magnetic Data to Model the Equatorial Electrojet and Derive Its Tidal Composition. *Journal of Geophysical Research: Space Physics*, *127*(9), e2022JA030691. https://doi.org/https://doi.org/10.1029/2022JA030691

Stolle, C., Michaelis, I., Xiong, C., Rother, M., Usbeck, T., Yamazaki, Y., Rauberg, J., & Styp-Rekowski, K. (2021a). Observing Earth's magnetic environment with the GRACE-FO mission. *Earth, Planets and Space*, *73*(1). https://doi.org/10.1186/s40623-021-01364-w

Stolle, C., Michaelis, I., Xiong, C., Rother, M., Usbeck, T., Yamazaki, Y., Rauberg, J., & Styp-Rekowski, K. (2021b). Observing Earth's magnetic environment with the GRACE-FO mission. *Earth, Planets and Space*, *73*(1). https://doi.org/10.1186/s40623-021-01364-w

Stolle, C., Olsen, N., Anderson, B., Doornbos, E., & Kuvshinov, A. (2021). Special issue "Characterization of the geomagnetic field and its dynamic environment using data from space-based magnetometers." In *Earth, Planets and Space* (Vol. 73, Issue 1). Springer Science and Business Media Deutschland GmbH. https://doi.org/10.1186/s40623-021-01409-0

Styp-Rekowski, K., Michaelis, I., Stolle, C., Baerenzung, J., Korte, M., & Kao, O. (2022). Machine learning-based calibration of the GOCE satellite platform magnetometers. *Earth, Planets and Space*, *74*(1), 138. https://doi.org/10.1186/s40623-022-01695-2

Styp-Rekowski, K., Stolle, C., Michaelis, I., & Kao, O. (2021). Calibration of the GRACE-FO Satellite Platform Magnetometers and Co-Estimation of Intrinsic Time Shift in Data. *2021 IEEE International Conference on Big Data (Big Data)*, 5283–5290. https://doi.org/10.1109/BigData52589.2021.9671977

Tayler, M. C. D., Mouloudakis, K., Zetter, R., Hunter, D., Lucivero, V. G., Bodenstedt, S., Parkkonen, L., & Mitchell, M. W. (2022a). Miniature Biplanar Coils for Alkali-Metal-Vapor Magnetometry. *Physical Review Applied*, *18*(1). https://doi.org/10.1103/PhysRevApplied.18.014036

Tayler, M. C. D., Mouloudakis, K., Zetter, R., Hunter, D., Lucivero, V. G., Bodenstedt, S., Parkkonen, L., & Mitchell, M. W. (2022b). Miniature Biplanar Coils for Alkali-Metal-Vapor Magnetometry. *Physical Review Applied*, *18*(1). https://doi.org/10.1103/PhysRevApplied.18.014036

Thébault, E., Hulot, G., Langlais, B., & Vigneron, P. (2021). A Spherical Harmonic Model of Earth's Lithospheric Magnetic Field up to Degree 1050. *Geophysical Research Letters*, *48*(21). https://doi.org/10.1029/2021GL095147

Thomsen, P. L., & Hansen, F. (1999). *Danish Ørsted Mission In-Orbit Experiences and Status of The Danish Small Satellite Programme*.

Troullinou, C., Jiménez-Martínez, R., Kong, J., Lucivero, V. G., & Mitchell, M. W. (2021). Squeezed-Light Enhancement and Backaction Evasion in a High Sensitivity Optically Pumped Magnetometer. *Physical Review Letters*, *127*(19). https://doi.org/10.1103/PhysRevLett.127.193601

Vershovskii, A. K., Balabas, M. V., Ivanov, A. É., Kulyasov, V. N., Pazgalev, A. S., & Aleksandrov, E. B. (2006). Fast three-component magnetometer-variometer based on a cesium sensor. *Technical Physics*, *51*(1), 112–117. https://doi.org/10.1134/S1063784206010166

Vigneron, P., Hulot, G., Léger, J.-M., & Jager, T. (2021). Using improved Swarm's experimental absolute vector mode data to produce a candidate Definitive Geomagnetic Reference Field (DGRF) 2015.0 model. *Earth, Planets and Space*, *73*(1), 197. https://doi.org/10.1186/s40623-021-01529-7

Wang, H., Wu, T., Xiao, W., Wang, H., Peng, X., & Guo, H. (2021). Dual-Mode Dead-Zone-Free Double-Resonance Alignment-Based Magnetometer. *Physical Review Applied*, *15*(2). https://doi.org/10.1103/PhysRevApplied.15.024033

Wang, T., Lee, W., Limes, M., Kornack, T., Foley, E., & Romalis, M. (2023a). *Pulsed Vector Atomic Magnetometer Using an Alternating Fast-Rotating Field*. http://arxiv.org/abs/2304.00214

Wang, T., Lee, W., Limes, M., Kornack, T., Foley, E., & Romalis, M. (2023b). *Pulsed Vector Atomic Magnetometer Using an Alternating Fast-Rotating Field*. http://arxiv.org/abs/2304.00214

Wang, X., Ye, M., Lu, F., Mao, Y., Tian, H., & Li, J. (2022). Recent progress on micro-fabricated alkali metal vapor cells. *Biosensors*, *12*(3), 165.

Weis, A., Bison, G., & Pazgalev, A. S. (2006). Theory of double resonance magnetometers based on atomic alignment. *Physical Review A - Atomic, Molecular, and Optical Physics*, *74*(3). https://doi.org/10.1103/PhysRevA.74.033401

Wilson, N., Light, P., Luiten, A., & Perrella, C. (2019). Ultrastable Optical Magnetometry. *Physical Review Applied*, *11*(4). https://doi.org/10.1103/PhysRevApplied.11.044034

Wilson, N., Perrella, C., Anderson, R., Luiten, A., & Light, P. (2020). Wide-bandwidth atomic magnetometry via instantaneous-phase retrieval. *Physical Review Research*, *2*(1). https://doi.org/10.1103/PhysRevResearch.2.013213

Wolfgramm, F., Cerè, A., Beduini, F. A., Predojević, A., Koschorreck, M., & Mitchell, M. W. (2010). Squeezed-Light Optical Magnetometry. *Physical Review Letters*, *105*(5), 53601. https://doi.org/10.1103/PhysRevLett.105.053601

Yamazaki, Y., Stolle, C., Xiong, C., Alken, P., Yang, Y., Zhima, Z., Harding, B., & Yan, R. (2024). Day-to-day and longitudinal variability of the equatorial electrojet as viewed from the Sun-synchronous CSES satellite. *Frontiers in Astronomy and Space Sciences*, *11*. https://doi.org/10.3389/fspas.2024.1460312

Yang, Y., Zhou, B., Hulot, G., Olsen, N., Wu, Y., Xiong, C., Stolle, C., Zhima, Z., Huang, J., Zhu, X., Pollinger, A., Cheng, B., Magnes, W., Zhao, X., & Shen, X. (2021). CSES High Precision Magnetometer Data Products and Example Study of an Intense Geomagnetic Storm. *Journal of Geophysical Research: Space Physics*, *126*(4), e2020JA028026. https://doi.org/https://doi.org/10.1029/2020JA028026

Yashchuk, V. V., Budker, D., Gawlik, W., Kimball, D. F., Malakyan, Y. P., & Rochester, S. M. (2003). Selective Addressing of High-Rank Atomic Polarization Moments. *Physical Review Letters*, *90*(25), 4. https://doi.org/10.1103/PhysRevLett.90.253001

Yin, F. (2009). *Mathematic Approaches for the Calibration of the CHAMP Satellite Magnetic Field Measurements*. http://nbn-resolving.org/urn:nbn:de:kobv:517-opus-41201

Yu, M., Chen, Y., Wang, Y., Han, X., Luo, G., Zhao, L., Wang, Y., Ma, Y., Lu, S., Yang, P., Lin, Q., Wang, K., & Jiang, Z. (2024). Microfabricated Atomic Vapor Cells with Multi-Optical Channels Based on an Innovative Inner-Sidewall Molding Process. *Engineering*, *35*, 46–55. https://doi.org/10.1016/j.eng.2023.08.016

Yudin, V. I., Taichenachev, A. V., Dudin, Y. O., Velichansky, V. L., Zibrov, A. S., & Zibrov, S. A. (2010). Vector magnetometry based on electromagnetically induced transparency in linearly polarized light. *Physical Review A - Atomic, Molecular, and Optical Physics*, *82*(3). https://doi.org/10.1103/PhysRevA.82.033807

Zhang, R., Kanta, D., Wickenbrock, A., Guo, H., & Budker, D. (2023). Heading-Error-Free Optical Atomic Magnetometry in the Earth-Field Range. *Physical Review Letters*, *130*(15), 153601. https://doi.org/10.1103/PhysRevLett.130.153601

Zhang, R., Mhaskar, R., Smith, K., Balasubramaniam, E., & Prouty, M. (2021). Vector measurements using all optical scalar atomic magnetometers. *Journal of Applied Physics*, *129*(4). https://doi.org/10.1063/5.0037991

Zhang Rahul Mhaskar Geometrics, R. (2019). *INTERIM REPORT Advanced Magnetometer System Task II*.

Zhivun, E., Wickenbrock, A., Patton, B., & Budker, D. (2014). Alkali-vapor magnetic resonance driven by fictitious radiofrequency fields. *Applied Physics Letters*, *105*(19). https://doi.org/10.1063/1.4902028

Zhou, Y.-L., Lühr, H., & Alken, P. (2020). Average Ionospheric Middle and Low Latitudes Nighttime Zonal Currents Deduced From CHAMP. *Journal of Geophysical Research: Space Physics*, *125*(8), e2019JA027702. https://doi.org/https://doi.org/10.1029/2019JA027702

Zhu, J., Jiang, L., Zhao, X., Liu, J., Fang, C., Shao, Q., Zou, Y., Xu, J., & Wang, Z. (2025). Phase-error-free atomic magnetometer and vector measurement method based on demodulated signal phase in geomagnetic environment. *Measurement: Journal of the International Measurement Confederation*, *242*. https://doi.org/10.1016/j.measurement.2024.116022

1 STATE-OF-THE-ART REVIEW

1.1 Optically pumped magnetometers

1.1.1 Introduction

Optically pumped magnetometers (OPMs) are highly sensitive atomic sensors that measure the magnetic field based on the interaction between the electron spin of each atom in a vapor and its magnetic environment. Due to their high sensitivity, accuracy, and portability, the possible application spans a variety of fields. In healthcare, OPMs are actively studied for mapping brain activity magnetoencephalography (MEG) with high temporal resolution (Borna et al., 2020; Boto et al., 2018; Gialopsou et al., 2021; Hamalainen et al., 1993; Kowalczyk et al., 2021; Petrenko et al., 2021; Tierney et al., 2019; Zhang et al., 2025) aiding in neurological research and clinical diagnostics, magnetomyography (Broser et al., 2018; Jensen et al., 2016), magnetocardiography (Batie et al., 2018; Belfi et al., 2007; Bison et al., 2003; Meng et al., 2023; Sander et al., 2020; Sulai et al., 2019) and magnetic field imaging (Lembke et al., 2014) and magnetic biomarkers (Bi et al., 2021; Bougas et al., 2018; Johnson et al., 2012). OPMs have also been used to study biomagnetism of plants (Corsini et al., 2011; Fabricant et al., 2021), and livestock, to record the heartbeat of cuttle (Sutter et al., 2020). In geophysics, OPMs are used for mineral exploration and magnetic anomaly detection offering a non-invasive means of studying subsurface features (Dang et al., 2010), including cave exploration (David Gibson, 2010). OPMs are also valuable tools in defense and security applications such as submarine detection and magnetic communication (Lipka et al., 2024; Page et al., 2021), magnetic anomaly-based navigation (Deans et al., 2018), electromagnetic induction imaging (Bevilacqua et al., 2021; Jensen et al., 2016; Maddox et al., 2022), and for unexploded ordnance detection. In fundamental research, OPMs have been used to study spin dynamics and in searches for physics beyond the Standard Model (Abel et al., 2020; Afach et al., 2024). On top of these, OPMs have also been used for Earth observation (Acuna, 1974; Bennett et al., 2021; Olsen et al., 2010) and are considered for extraterrestrial exploration (Fan et al., 2022).

One of the most interesting applications for magnetometry is related to the characterization of the outer space magnetic fields. As technology evolved, humanity managed to put different kinds of devices in space. The first one to put a magnetometer in a spacecraft was the Soviet Union in the Sputnik III mission. The satellite was launched on May 18th, 1958, and it carried a magnetometer among other apparatus for scientific research. The purpose of the mission was to obtain the spatial distribution of Earth’s magnetic field in the upper atmosphere. Given the requirements of the mission and the technical difficulties of measuring vector components, the device that could meet the requirements was either a nuclear-resonance magnetometer or a fluxgate. Although the former had advantages over other methods — such as being independent of the orientation of the detector and providing absolute measurements — the satellite’s intrinsic electrical and magnetic noise produced interference. This interference would not let the magnetometer measure as accurately as required, or it would need a 200W polarizing power. As a consequence, a self-oriented triaxial fluxgate was used as the magnetometer for the Sputnik III mission. The device's design was previously used during World War II in submarine detection and geophysical exploration, which gave background on reliability. The entire apparatus weighed around 12.5 kg and was designed to be accurate within 0.05% of the total field in a range of 15 μT to 60 μT (DOLGINOV et al., 1961).

The first non-fluxgate magnetometer used in space was aboard the Vanguard III satellite, launched in 1959. The device was a proton precession magnetometer with an accuracy of less than 1 nT and the total weight was 0.85 kg (Heppner et al., 1960). The device was telemetered from Earth so the battery power supply could meet the planned life. The detector employed a single cell filled with normal hexane, measuring 1 inch in diameter and 4 inches long (Ness, 1970). Regarding atomic magnetometers, the first one in space was in the Explorer X spacecraft in 1961 to measure the vector magnetic field and plasma flux. Together with a rubidium magnetometer, the satellite carried two fluxgates with its programmed sensitivity calibrator, and a system of 4-loop bias coils to convert the Rb magnetometer from a scalar device to a vector one in weak fields. The complete magnetometer weighed 1 kg and provided a fluxgate-data accuracy of ±0.25 nT in the range 3 nT to 10 µT. Two hours after the injection of the satellite, the oscillations of the atoms became intermittent. It was nevertheless used to calibrate the fluxgates in weak fields. The test performed after the flight showed that during launch, the overheating of the nose cone surface near the sphere caused outgassing, which deposited a film on the coils' support sphere. This film significantly increased the surface's ability to absorb heat, leading to temperatures rising over 55ºC and causing the electrodeless discharge of the lamp and the subsequent operational failure of the device (Heppner et al., 1963).

^{4}He magnetometers have been used in a variety of missions. They can be used as vector magnetometers, and as absolute scalar magnetometers, with little sensitivity to temperature. Helium magnetometers were first used aboard Mariner IV and V to measure the magnetic fields of Mars in 1964 and Venus in 1967, respectively. These sensors weighed 2.9 kg, and it had rms noise of 0.1 nT per axis in a range of ±204 nT (Connor, 1968). More recent space missions have mostly employed fluxgates, at times with an OPM as an absolute reference as in the JUICE mission, which uses fluxgates and a He-4 absolute scalar magnetometer (ASM). This device reached a noise floor of less than 10 pT/√Hz in a range of ±5000 nT, with a total weight of 440 g (Amtmann et al., 2024)

Depending on the satellite's mission, the magnetometer must meet specific operational requirements. Key constraints typically include size, weight, and power (SWaP) limitations inherent to satellite design. These requirements will be discussed in detail in Section 2. Additionally, mission-specific objectives dictate performance parameters such as measurement range, sensitivity, accuracy, and bandwidth. Furthermore, to qualify for space deployment, a magnetometer must undergo rigorous testing to ensure its resilience to radiation, vibration, and temperature variations. These stringent requirements significantly constrain the selection of suitable magnetometers for space applications.

1.1.1.1 OPM principle of operation

OPMs operate based on the interaction between light and the magnetic properties of atoms. The core principle is to optically measure the Zeeman splitting that occurs among the magnetic sublevels in the hyperfine structure of atoms. Zeeman splitting is directly proportional to the magnitude of the magnetic field B_{DC}, and is quantified by the Larmor precession frequency $\omega_L = \gamma B_{DC}$, where γ is the gyromagnetic ratio associated with the atomic spin. The spin precession can be detected by measuring changes in the optical properties of the gas, for example, by measuring the polarization rotation of probe light (angle ϑ_F) due to the Faraday effect or measuring the change in absorption of resonant probe light. By analyzing the state of the light, for example with a set of polarization optics and detectors, the magnetometer can determine the strength (and sometimes the direction) of the magnetic field with high precision.

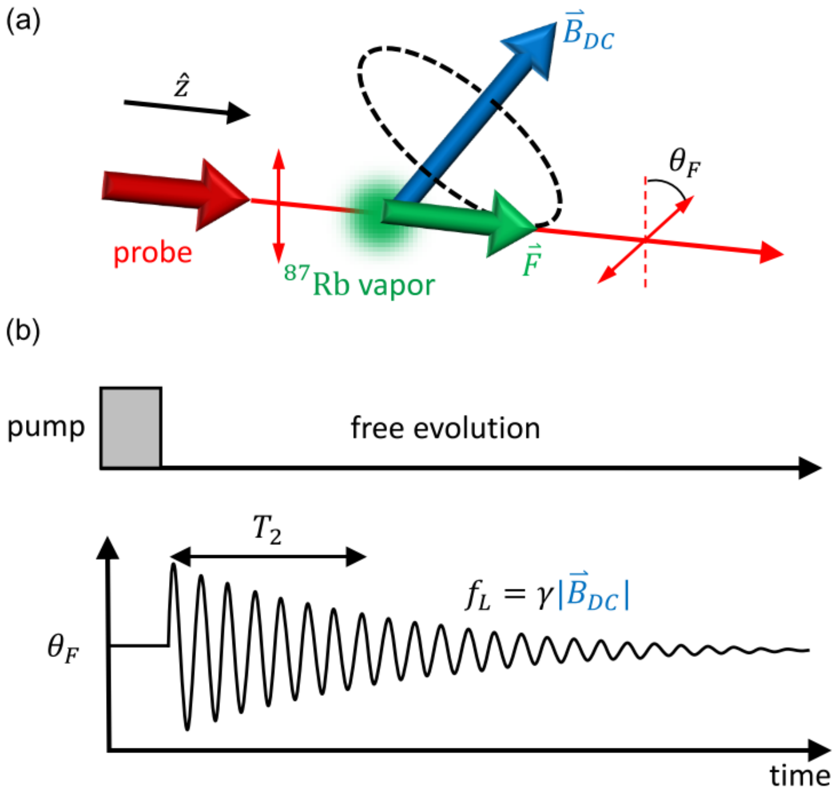

Figure 1-1. Operational schematic of an OPM using Faraday rotation readout based on the free induction decay (FID) technique. (a) Initially polarized spin **F** is aligned along the z axis, and precesses about the magnetic field B_{DC}, which is detected by a linearly polarized probe beam with the Faraday rotation readout of the rotation angle θ_F. (b) FID pump and measurement timing diagram. The decay of the FID signal oscillating at the Larmor frequency is characterized by the coherence time T_2.

A representative OPM mode of operation is the free-induction-decay (FID) magnetometer, illustrated in Figure 1-1. In the FID OPM, an optically-addressable atomic gas, (e.g. metastable helium, or alkali metal vapors such as rubidium vapor or cesium vapor), is exposed to polarized light resonant to an optical transition. This (pump) light polarizes the atoms, which means that their spin **F** becomes polarized in a particular direction. The presence of an external magnetic field B_{DC} causes a precession of these spins, which gradually decay over time due to spin relaxation mechanisms at a rate Γ, with spin dynamics well described by the Bloch equation:

$$\frac{dF}{dt}=\gamma B_{DC}\times F\text{-}\Gamma F.$$

The ultimate sensitivity that atomic magnetometers can reach is limited by atomic spin projection noise, fundamentally set by the uncertainty relation:

$$\Delta F_y \Delta F_z \geq \frac{\langle F_x \rangle}{2}$$

where ΔF_i denotes the uncertainty in the macroscopic spin component F_i, for i = x, y, z. One can notice that it is possible to improve the sensitivity of the magnetometer by implementing a technique called spin squeezing - namely by reducing the uncertainty in one component of the atomic spin ΔF_x or ΔF_y (but not both simultaneously) (Kuzmich et al., 1997; Sewell et al., 2012) , This technique redistributes spin projection noise, enabling more precise measurements of magnetic fields without increasing the number of atoms. Moreover, squeezing of the probing light may also be used to beat the sensitivity limits set by the photon shot noise (Horrom et al., 2012; Troullinou et al., 2021; Wolfgramm et al., 2010). Such squeezing-enhanced atomic magnetometry together with other quantum-enhancing techniques such as quantum non-demolition and measurement backaction evading measurements (Troullinou et al., 2021) allow to surpass the standard quantum limit for OPMs' sensitivity (Auzinsh et al., 2004).

Leaving aside the possibility of spin squeezing, the quantum-limited precision δB of atomic magnetometers after a measurement time t is set by the number of atoms N being probed and the coherence time T_2 of the Zeeman transitions, as given by the so-called “Equation 1,” defining the fundamental sensitivity limitations of an atomic sensor (Budker & Romalis, 2007):

$$\delta B = \frac{1}{\gamma\sqrt{N T_2 t}}$$

This equation indicates the advantages of using larger cell sizes: the number of atoms N increases, while the number of collisions with the cell walls decreases, enhancing the coherence time T_2. In fact, the highest sensitivity in all types of atomic magnetometers has been achieved using cells with volumes of a few cubic centimeters (Dang et al., 2010). However, larger cells imply also more decoherence due to magnetic gradients, lower spatial resolution, and higher SWAP. These considerations motivated large efforts toward miniaturization of vapor cells and OPMs. A significant advancement in this regard was the development of microfabricated vapor cells using silicon micromachining in the early 2000s (Liew et al., 2004a), which is expected to be essential in reducing OPM production costs and facilitating mass production. MEMS cells, with volumes as small as 1 mm^3, have enabled the spatial mapping of magnetic fields with millimeter resolution (X. Wang et al., 2022). Since wall collisions are one of the main decoherence mechanisms in most vapor-based instruments, mitigation techniques such as buffer gases and anti-relaxation wall coatings have been developed.

Decoherence in vapor cells stems from various factors, including spin-exchange collisions, buffer gas and wall collisions, light scattering, and spatial variations of the magnetic field across the vapor cell. In the most sensitive OPMs, which utilize high atomic densities, spin-exchange collisions typically emerge as the dominant source of decoherence.

1.1.2 Scalar OPMs

The most common operation of an OPM is as a scalar magnetometer because the fundamental operating principle is to measure the Zeeman splitting of magnetic sublevels proportional to the magnetic field strength. Over the past six decades a diverse range of techniques have been developed based on this principle, each optimized for specific sensing applications. Table 1-1 provides a comprehensive overview of scalar OPM techniques reported in the literature, summarizing key performance parameters relevant to magnetometry, including sensitivity, accuracy, bandwidth, whether the technique is fully optical, and whether it exhibits sensing deadzones.

Table 1-1. Summary of the main optically pumped magnetometer technologies categorized based on the sensor configuration.

Method	Sensitivity (fT/√Hz)	Accuracy (nT)	Bandwidth (kHz)	Dead zones	All optical ?	Sensor Volume [Cell Volume]
Mz 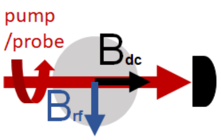	10 (Schultze et al., 2017)	2 (Skillman et al., 1958)	1 (Schultze et al., 2017)	Probing ⊥B	No	69 × 69 × 167 mm^3 (Oelsner et al., 2022)
In the M_z mode, circularly polarized light parallel to the bias magnetic field B_{DC} polarizes atoms along the magnetic field direction. An orthogonally resonant RF field drives the atomic spins into resonance at Larmor frequency, which induces a narrow absorption resonance in the transmitted light, detected by the photodetector.						
Mx 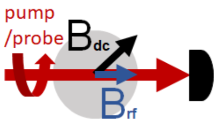	10 (Groeger, Bison, Schenker, et al., 2006)	0.1 (Scholtes et al., 2011)	1 (Groeger, Bison, Knowles, et al., 2006; Yang et al., 2020)	No	No	25mm^3 [2mm^3] (Schwindt et al., 2007)
In the M_x mode, the direction of circularly polarized light which polarizes the atoms, and the bias magnetic field are inclined by 45 degrees. The RF field is aligned in parallel with the pump orientation. The transmitted light is modulated to be in resonance with the Larmor frequency. The measured light absorption is affected by the transverse magnetization component.						
FID 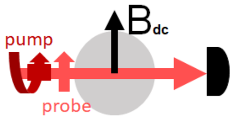	10 (Limes et al., 2020)	0.1 (Lee et al., 2021)	0.5 (Hunter et al., 2023)	Probing IIB	Yes	6.5 × 1.8 ×1.8 cm^3 [8 × 8 × 12.5 mm^3] (Limes et al., 2020)
FID magnetometers measure free decay of the atomic polarization, after being driven by a resonant pulse of a circularly polarized pump. The relaxation of spin states in the absence of the driving pump light generates an oscillating signal at the Larmor frequency, with the decay characterized by the coherence time T_2.						
Bell-Bloom	70	NR	1	Probing IIB	Yes	16 mm^3 (Gergino

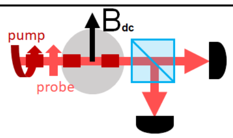	(Gerginov et al., 2020)		(Gerginov et al., 2017)			v et al., 2017)
Bell-Bloom magnetometer uses stroboscopic optical pumping, with pump light being intensity or frequency modulated at the Larmor frequency, to polarize atomic spins continuously, what prevents rapid depolarization. Readout is realized by detection of the linearly polarized, continuous probe light with a balanced polarimeter.						
SERF (+ compensation coils) 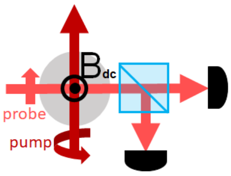	1000 (Seltzer & Romalis, 2004)	NR	0.05 (Seltzer & Romalis, 2004)	Probing IIB	No	7.3 cm × 7.3 cm × 8.3 cm (Seltzer & Romalis, 2004)
Spin exchange relaxation free magnetometers operate at low magnetic fields, where the effects of spin exchange relaxation are suppressed. Strong circularly polarized pump sets the atomic spin orientation, atomic spins precess in the bias magnetic field, which is probed through the polarization rotation of the weak probe light. Currently the most sensitive optical magnetometers.						
NMOR 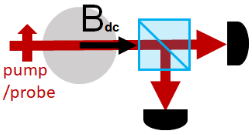	70 (Lucivero et al., 2014)	NR	100 (Li et al., 2020)	NR	Yes	7×10^{-4} mm^3 (Sebbag et al., 2021)
Linearly polarized light produces spin alignment along the polarization direction. A bias field rotates this alignment to produce linear dichroism and thus optical polarization rotation, which is detected a balanced polarimeter. Light is typically phase or amplitude modulated, which enables detection of nonzero magnetic fields.						
CPT/EIT 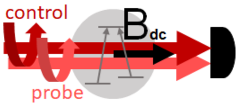	4000 (Stähler et al., 2001)	0.2 (Pati et al., 2023)	0.1 (Pati et al., 2023)	No	Yes	0.94 cm^3 (Hong et al., 2021)
Atoms are prepared in non-interacting coherent superposition of hyperfine sublevels (sensitive to magnetic field) via coherent population trapping (so called ‘dark states’), followed by the detection of the transmission resonance, which due to electromagnetically induced transparency indicates the magnitude of the measured magnetic field.						
^{4}He	340 (Yi et al., 2024)	0.05 (Shifrin et al., 2008)	5 (Yi et al., 2024)	Probing IIB	Yes	NR

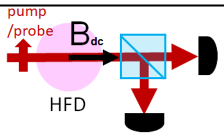						
Typically based on NMOR configuration. Helium gas is excited using high frequency discharge, moving some atoms to a metastable state that can be pumped and probed with NIR wavelengths.						
μW HFS 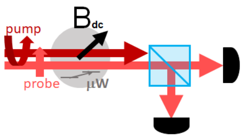	6000 (Aleksandrov et al., 2006)	0.5 (Aleksandrov et al., 2006)	NR	No	Yes	NA
μW HFS magnetometer uses the resonances in the hyperfine structure of the ground state of an alkali atom driven by microwave field. With special tailoring of the μWs, the magnetometer can function at any angles between the pump direction and magnetic field vector (deadzone free).						
Self-Oscillating 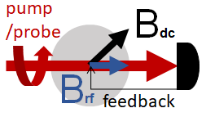	50000 (STUART et al., 1964)	10 (STUART et al., 1964)	0.005 (STUART et al., 1964)	No	Yes	
Self-oscillating magnetometers are close in operation to the Mx-based OPMs, with additional feed-back loop, dynamically adjusting the driving signal to match the resonance condition.						
M_x-M_z tandem 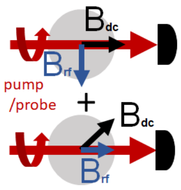	900 (H. Wang et al., 2021)	NR	0.1 (H. Wang et al., 2021)	No	No	22 cm^3 [1mm^3] (Korth et al., 2016)
Implements both Mz and Mx mode operation, allowing to combine the accuracy of the Mz magnetometer with higher sampling rate of the Mx based OPM.						

Each technique in Table 1-1 offers distinct advantages and trade-offs, depending on the specific sensing requirements. For instance, hyperfine structure (HFS) magnetometers, such as those based on coherent population trapping (CPT) or microwave detection, achieve high accuracy (< 0.5 nT) and are free of deadzones but generally exhibit lower sensitivity (~ few pT). Conversely, methods like free-induction decay (FID), Mx, and Bell-Bloom magnetometers provide state-of-the-art sensitivity but are susceptible to deadzones that can limit their applicability in applications where the magnetic field direction can vary such as in magnetic navigation. Some techniques, including Bell-Bloom, self-oscillating, Mx, and Mz, operate in a closed-loop configuration, which offers advantages for real-time readout, but can be susceptible to inaccuracies arising from phase errors.

The most widely used OPMs contain an alkali vapor, typically rubidium (Rb), cesium (Cs), or potassium (K), due to their ability to achieve high sensitivity, their compatibility with infrared laser wavelengths, and their potential for miniaturization. To maintain sufficient vapor pressure, these sensors typically operate at temperatures between 70°C and 120°C. In rare cases, when the vapor cell is sufficiently large, an OPM can function at room temperature. This heating requirement is a key consideration for space applications: on one hand, it increases power consumption, while on the other, heat dissipation in space is more challenging than in Earth's atmosphere.

Metastable ^{4}He-based OPMs form a distinct category due to their unique operational requirements. Unlike alkali OPMs, these sensors rely on a high-frequency discharge (HFD) to generate plasma to excite metastable helium atoms, which contain magnetically sensitive electron spin states that can be optically pumped and probed similarly to alkali atoms. The primary advantage of ^{4}He OPMs is that they do not require heating, and their purely electronic magnetically sensitive states are immune to nonlinear Zeeman (NLZ) effects, which introduce systematic errors in alkali-based OPMs. However, they do not typically achieve the same sensitivity levels as alkali-based OPMs. In addition, miniaturization using silicon micromachining technology has proven difficult due to oxygen contamination, which degrades the effectiveness of the HFD process. Table 1-2 provides a comparative analysis of alkali-based and ^{4}He-based OPMs, while Figure 1-2 illustrates their respective energy level structures and transitions involved during optical pumping/probing.

The remainder of this section reviews key parameters of scalar OPMs relevant for space and geomagnetic applications reported in the literature, including sensitivity, bandwidth, accuracy, deadzone-free operation, and size, weight, and power (SWaP). Where relevant, we also discuss emerging technologies with the potential to advance the current state-of-the-art.

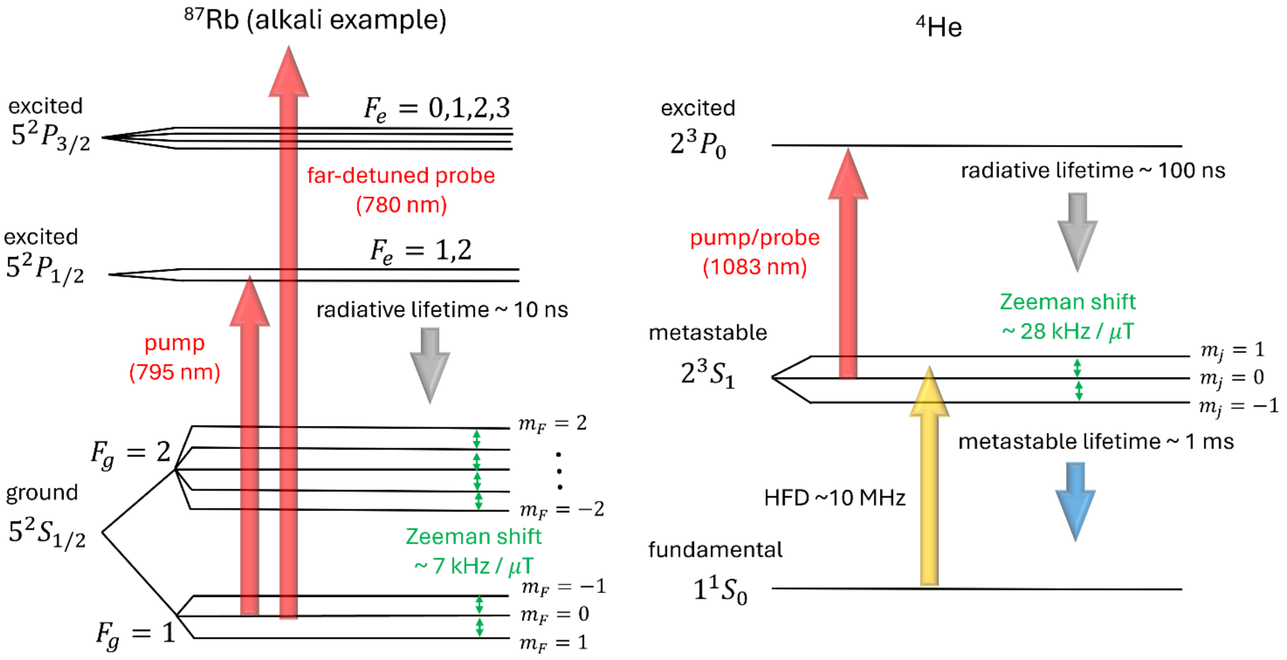

Figure 1-2. ^{87}Rb (alkali) vs ^{4}He energy–level diagram.

Table 1-2. Comparison of Alkali vs ^{4}He OPMs.

	Alkali OPMs	**^{4}He OPMs**
vapor cell heating?	Yes (70ºC – 120ºC)	No
Scalar accuracy	0.1 nT – 10 nT	~0.05 nT
HFD?	No	Yes
State-of-the-art sensitivity	1-10 fT/ √Hz	100 fT/ √Hz
Miniaturization?	Yes, silicon microfabrication well-established (1 mm^3)	No, used glass-blown cells smallest are 0.1 cm^3

1.1.2.1 Sensitivity

In this section, we review the sensitivity of scalar OPMs reported in the literature over the past six decades. While the Introduction defines a fundamental sensitivity limit based on atomic density, vapor cell volume, coherence time (T_2), and the gyromagnetic ratio, reaching this theoretical limit in practical implementations remains challenging. This is evident in the sensitivity plots shown in Figure 1-3, where no clear correlation is observed between sensitivity and vapor cell size across the wide range of scalar OPM techniques. However, a general trend of sensitivity improvements has been apparent over the past six decades. Notably, laboratory-based OPMs currently demonstrate significantly higher precision than those deployed in space.

We also discuss ongoing research aimed at further enhancing sensitivity, which remains primarily laboratory-based and not yet ready for field deployment. These approaches can be categorized into three main types:

1. Enhancing the light-atom interaction: These methods aim to increase the measured atomic signal relative to photon shot noise. Strategies include the use of multi-pass cells (Cai et al., 2020; Lucivero et al., 2022; Sheng et al., 2013; Yi et al., 2024) and optical cavity enhancement (Crepaz et al., 2015; Hernández Ruiz et al., 2024; Mazzinghi et al., 2021), which effectively amplify the interaction between light and atoms.

2. Extending coherence time (T_2): Techniques in this category focus on prolonging atomic coherence, thereby improving sensitivity. Examples include light-narrowing effects in alkali OPMs (Bhaskar et al., 1981; Oelsner et al., 2022; Scholtes et al., 2011), the use of nuclear spin ensembles such as noble gases such as ^{3}He (Grosz et al., 2017) and Xe (Yashchuk et al., 2004), and optically addressable nuclear spins, such as Hg (Ban et al., 2018).

3. Quantum enhancement techniques: These methods leverage quantum squeezing to reduce quantum fluctuations in either atomic spin (Colangelo et al., 2017; Madsen & Mølmer, 2004; Trail et al., 2010) or light (Troullinou et al., 2021) beyond the standard quantum limit imposed by the Heisenberg uncertainty principle. Quantum non-demolition (QND) and back-action evasion (BAE) schemes are particularly relevant, as they suppress quantum noise in an unobserved variable, ensuring that the measurement process does not introduce back-action noise that degrades subsequent measurements (Marlan O. Scully et al., 1991).

Each of these approaches holds promise for pushing OPM sensitivity closer to fundamental limits, though further development is needed before they can be integrated into practical sensing applications.

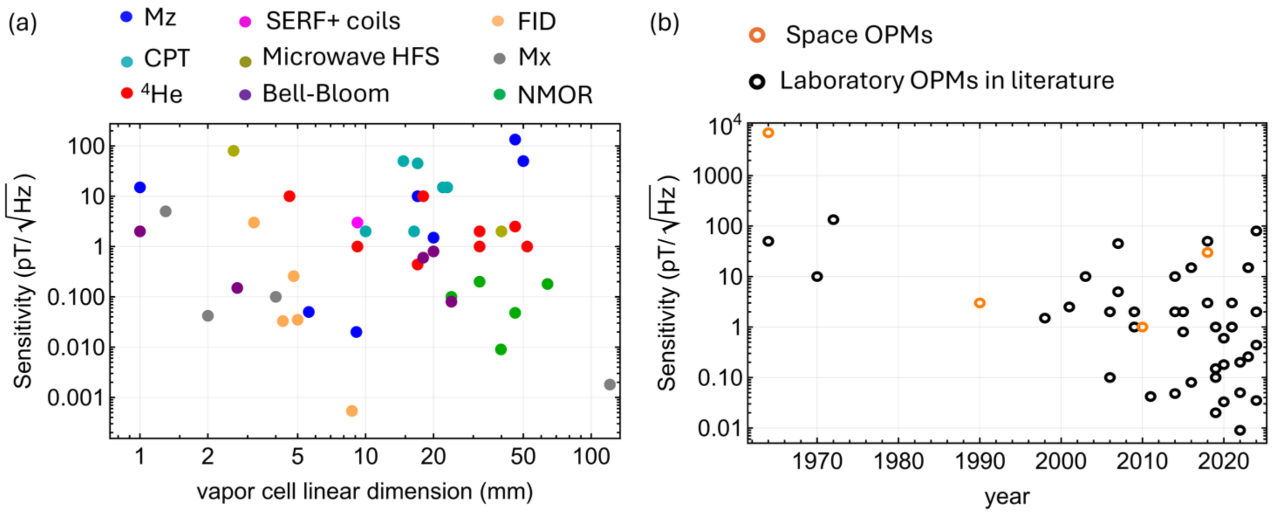

Figure 1-3. Scalar sensitivity vs vapor cell linear dimensions.

1.1.2.2 Bandwidth

As it will be discuss in Section 2, the bandwidth of magnetometers in space missions is crucial because it determines which parts of the spectrum can be measured. Space missions typically focus on measuring low-frequency fields, ranging from DC to just a few Hz, which helps filter out specific magnetic noise. For instance, in the GRACE-FO mission, a cutoff frequency filter of 20s was applied to remove potential Alfvén waves (Stolle, Michaelis, et al., 2021a).

However, some missions require bandwidths extending up to the kHz or even few MHz range (Auster et al., 2009; Balogh et al., 2001; Connerney et al., 2017). Increasing the bandwidth often comes at the expense of sensitivity, requiring missions to carefully balance bandwidth requirements against the need for accurate and precise magnetic measurements. Compared to other devices, such as inductive pick-up coils, OPMs show less sensitivity advantage at higher frequencies (~50 MHz). As illustrated in Figure 1-4 (Savukov et al., 2007), the dot-dashed line represents the sensitivity of a potassium atomic magnetometer occupying the same volume as an inductive coil magnetometer, whose sensitivity is plotted as a solid line.

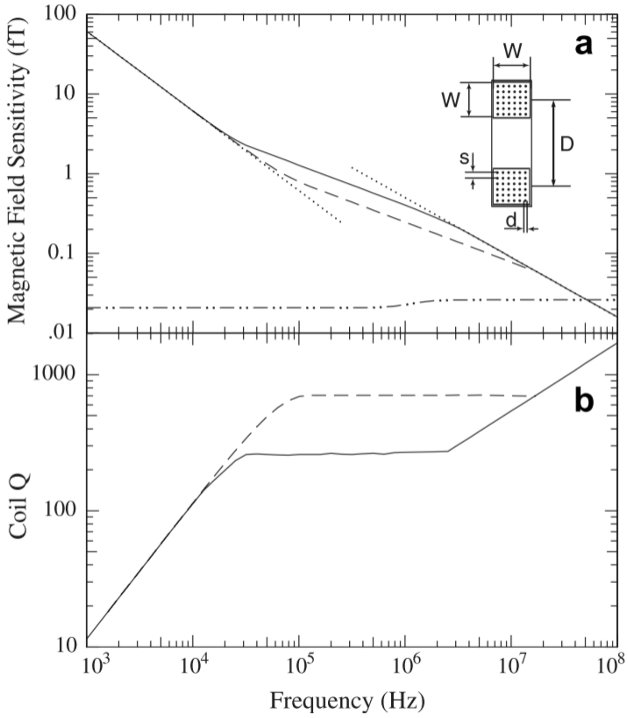

Figure 1-4 Figure taken from (Savukov et al., 2007). The dot-dashed line represents the sensitivity of a potassium atomic magnetometer occupying the same volume as an inductive coil magnetometer, whose sensitivity is plotted as a solid line. This analysis shows that OPMs have fundamental sensitivity advantages over inductive pick up coils for all frequencies up to the 50 MHz range. For more details refer to the article.

As shown in Figure 1-5, advancements in OPM techniques over the years have enabled increased bandwidth without necessarily sacrificing sensitivity. For example, (Wilson et al., 2020) demonstrated a magnetometer with a bandwidth of up to 400 kHz. Other notable examples include (S. Ingleby et al., 2022), who developed a 10 kHz magnetometer with a sensitivity of 70 fT/√Hz, and (Li et al., 2020), whose magnetometer achieved a bandwidth of over 100 kHz with a sensitivity of 80 fT/√Hz at 8 Hz bandwidth and 0.7 nT/√Hz for bandwidth at 1000 kHz. Both devices have proven to operate effectively at geophysically relevant magnetic field magnitudes. Although these remain laboratory-based techniques, they show significant potential for future space applications.

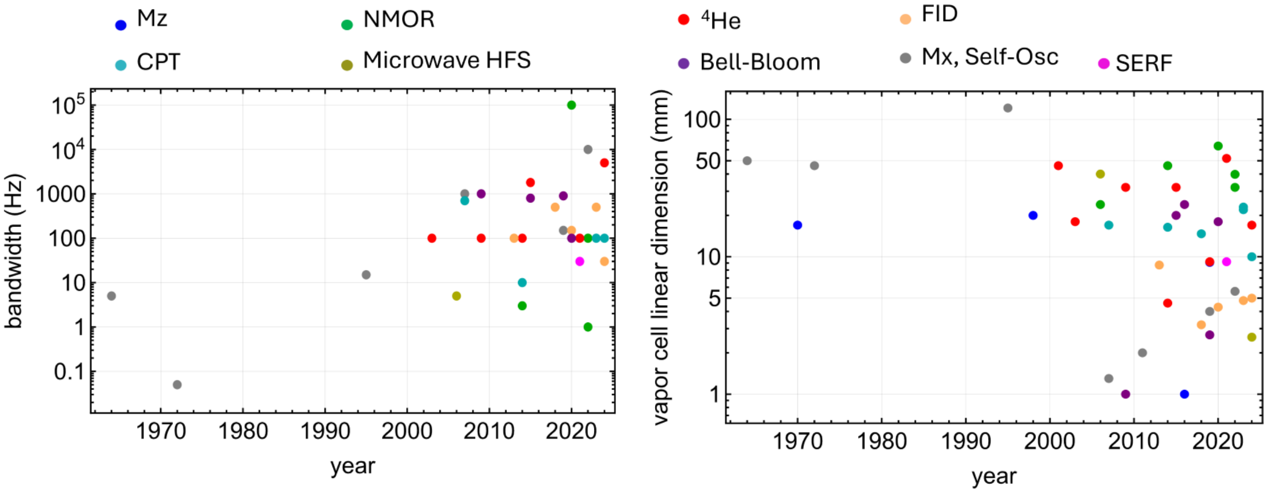

Figure 1-5. Scalar OPM bandwidth and vapor cell size over the last six decades

1.1.2.3 SWaP

In this section we examine commercial and Space OPM examples to demonstrate what is achievable in terms of SWaP. A significant advancement in this regard was the development of microfabricated vapor cells using silicon micromachining in the early 2000s (Liew et al., 2004), and is likely to be essential for reducing OPM production costs and facilitating mass production. Microfabricated vapor cells (H. Wang et al., 2021), with volumes as small as 1 mm^3, have enabled the spatial mapping of magnetic fields with millimeter resolution. These developments have applications in medical fields like magnetoencephalography (Alem et al., 2014) and magnetocardiography (Bison et al., 2003), as well as in remote NMR detection (Ledbetter et al., 2008). Additionally, the compact size of these cells is beneficial for space satellite integration, offering reduced size and weight (Knappe et al., 2023; Rutkowski et al., 2014). In these MEMS cells, buffer gases like N_2 are crucial for increasing diffusion length and mitigating wall collisions, thereby enhancing the coherence time T_2. The ongoing quest to miniaturize vapor cells further to micrometer scales and beyond is an active area of research (Baluktsian et al., 2010; Cutler et al., 2020; Lucivero, Zanoni, et al., 2022; Peyrot et al., 2019). Notable examples in the development of low SWaP OPMs are highlighted in Figure 1-6 including functionalized mm-sized vapor cell (Raghavan et al., 2024a), microfabricated cells with 3D optical access (Yu et al., 2024), and miniaturization of 3D coil systems (Tayler et al., 2022a). A notably low-SWaP example is presented in (Schwindt et al., 2007), where the device featured a compact 25 mm^3 volume, operated at a total power of 0.194 W, achieved a sensitivity of 5 pT/√Hz, and had a bandwidth of 1 kHz.

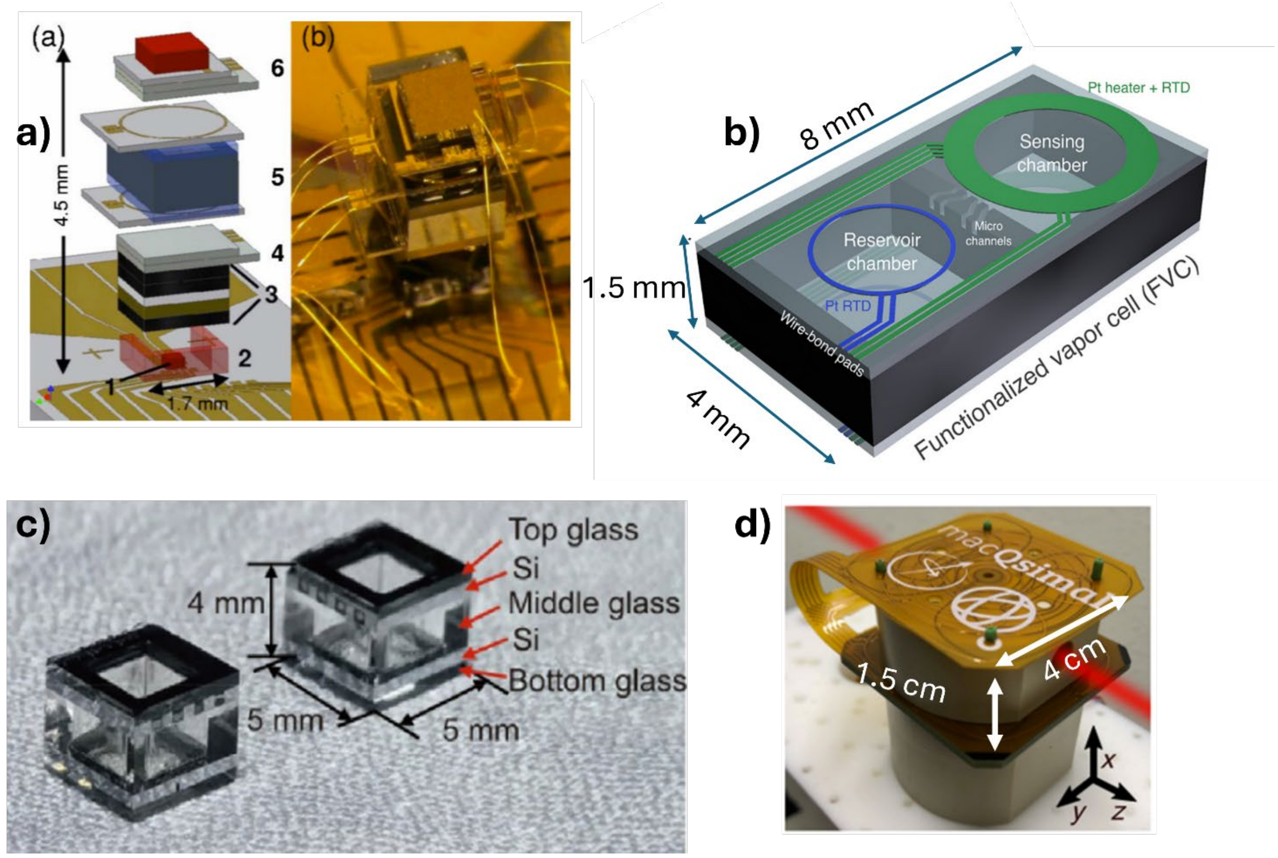

Figure 1-6. Notable examples in the development of low SWaP OPMs. (a) an extremely low-SWaP OPM (Schwindt et al., 2007). (b) Functionalized microfabricated vapor cells (Raghavan et al., 2024a). (c) Microfabricated vapor cells with 3D optical access (Yu et al., 2024). (d) Miniature bi-planar coil systems (Tayler et al., 2022a).

Most laboratory research OPMs found in literature are generally proof-of-principle and not optimized for lowest SWaP and often SWaP is not reported. Table 1-3 compares the characteristics of various OPMs, including commercially available models, those used in spacecraft, and laboratory-developed prototypes. One key observation is related to size, weight, and power (SWaP). While commercial models have characteristics comparable to those already deployed in space, laboratory-developed prototypes often fail to meet space mission requirements. This shortfall is mainly because many laboratory designs are not fully oriented toward space applications, focusing instead on proof-of-principle developments.

Another significant aspect is the scalar sensitivity of the magnetometers. Commercially available OPMs now offer higher sensitivity than those used in space missions. However, space mission magnetometers are not primarily optimized for sensitivity, as other parameters—such as dynamic range, accuracy, dead zones, and resolution. Furthermore, current designs are predominantly optimized for Earth-based applications and have yet to be tailored to meet the specific requirements of planetary exploration, solar wind studies, or outer space measurements.

In terms of dead zones, the space magnetometer listed in Table 1-3 has none, as expected for its specific mission requirements. Optical devices inherently avoid dead zones or can easily mitigate them with additional techniques, which is a notable advantage. Finally, although heading errors are crucial for ensuring directional accuracy, commercial and space-grade OPMs exhibit comparable performance in this area.

Table 1-3. Comparison between commercial vs space vs laboratory OPMs

	Sensor	**Sensitivity (pT/√Hz)**	**Accuracy (nT)**	**Deadzones**	**Size**	**Weight (g)**	**Power (W)**
Commercial OPMs	Fieldline Industries / SM300	0.5	3	±7° in equatorial plane	15 x 15 x 35 mm	17	1.5
	QUSPIN / QTFM Gen-2	3	3	±7°	17.7 x 19.8 x 35.8 mm	12	2.5
	GEM Systems / GSMP 35/25(Potassium)	0.2	0.5	±10° at ⊥B and IIB	161 x 64 mm diameter	1000	11-16
	Twinleaf / PPM (Rubidium)	0.2	5	±7°	16 x 36 x 136 mm	100	5
	Geometrics / MFAM(Cesium)	2	50	Polar 60°	33 x 25 x 32mm	230	5
Space OPMs	CSES / CPT	50	0.19	None	1.5 cm^3	340	3.3
	SWARM / ^{4}He	1	NR	None	40 × 60mm	3000	5.3
	NanoMagSat / ^{4}He	1	0.05	None	70 cm^3	NR	NR
Laboratory OPMs	NIST / Mx (Rubidium)	5	NR	Probing IIB	25 mm^3	NR	0.194

1.1.2.4 Deadzones

Another significant challenge in operating OPMs in geomagnetic fields is the occurrence of signal degradation in specific magnetic field orientations, referred to as dead-zones. This issue is particularly evident in the free-induction decay (FID) sensing configuration, where spin precession ceases when the magnetic field is aligned parallel to the pumping axis.

To address dead-zones, various strategies have been implemented, though they often increase the complexity of the sensor system. These approaches include the use of multiple probe beams or vapor cells (Chéron et al., 1997; Farthing & Folz, 1967; Geometrics, n.d.; Meilleroux, 1970), mechanical rotation of components (Guttin et al., 1994), placing the OPM within a coil system (Bertrand et al., 2021a), switching between Mx and Mz magnetometer configurations (Korth et al., 2016; H. Wang et al., 2021), or alternating between orientation and alignment detection (Ben-Kish & Romalis, 2010).

Additionally, hyperfine structure (HFS) magnetometers, which utilize either unpolarized light to probe microwave resonances (Aleksandrov et al., 2006) or coherent population trapping (CPT) resonances (Pollinger et al., 2018a), have demonstrated dead-zone-free operation. Moreover, ^{4}He based magnetometers can achieve dead-zone-free operation by using alignment detection (Lieb et al., 2019; Rutkowski et al., 2014), where the linear polarization of the probing light is rotated to prevent signal degradation.

Table 1-4. List of deadzone-free techniques

Dead-zone-free OPM techniques
Mx-Mz tandem (Korth et al., 2016; H. Wang et al., 2021)
Alignment-orientation tandem (Ben-Kish & Romalis, 2010)
Coil system magnetic environment (Bertrand et al., 2021a)
HFS magnetometry (Aleksandrov et al., 2006; Pollinger et al., 2018a)
He 4 alignment detection (Lieb et al., 2019; Rutkowski et al., 2014)
Multiple OPMs oriented orthogonally (Chéron et al., 1997; Farthing & Folz, 1967; Geometrics, n.d.; Meilleroux, 1970)

1.1.2.5 Accuracy

The scalar accuracy of optically pumped magnetometers (OPMs) is a key factor for various geomagnetic applications, not only in observing Earth's magnetic environment but also in areas such as navigation (Canciani & Raquet, 2016), geophysics (Friis-Christensen et al., 2006a; Stolle, Olsen, et al., 2021), space exploration (Bennett et al., 2021; Dougherty et al., 2004; Korth et al., 2016), and unexploded ordnance detection (Billings, 2004; Mark Prouty, 2016). For instance, magnetic anomaly detection requires accuracy better than 1 nT (Canciani & Raquet, 2016, 2017), while space missions often demand accuracy below 0.2nT (Ellmeier et al., 2023). Despite these needs, some OPM techniques achieve only around 10nT accuracy (Lee et al., 2021), and most commercial OPMs currently reach approximately 3nT (see Table). While this level of accuracy is adequate for certain applications, it falls short for others, driving ongoing research to push OPM precision to sub-nT levels.

The first type of systematic error in scalar OPMs is related to inaccuracies in extracting the Larmor frequency during signal analysis. A common example arises in closed-loop techniques such as Bell-Bloom, Mz, and Mx, where phase errors in the feedback signal can lead to frequency shifts. These phase errors can be mitigated with proper design of the sensor (Bulatowicz et al., 2023; Groeger et al., 2006; Zhu et al., 2025). To address this, free-induction decay (FID), also known as free spin precession (FSP), measurements are preferred for high-accuracy applications, as they directly monitor the atomic ensemble's precession frequency without relying on feedback (Grujić et al., 2015).

The second type of systematic error is associated with external perturbations in the sensor. A common example of this error are AC Stark shifts, also known as light shifts, which increases with the light intensity during detection and arise from the vector and tensorial components optical beam associated with circular and linear polarization respectively (Oelsner, Schultze, Ijsselsteijn, et al., 2019). By using sufficiently detuned light such as in Faraday rotation these light shifts can be mitigated to the few pT levels. Other methods include using unpolarized light during detection (Aleksandrov et al., 2006), or to use Ramsey style interrogation (Hunter et al., 2023). Another example of this type of systematic error is magnetization of the components that make up the sensor.

The third type of systematic error is associated with changes in the relationship between the Larmor frequency and the magnetic field strength associated with alkali-based OPMs. This systematic error is due to unresolved frequency components in the Larmor signal, caused by nonlinear Zeeman (NLZ) shifts within the ground-state hyperfine manifolds (Alexandrov, 2003; Lee et al., 2021). These errors arise from variations in the strengths of the frequency components that contribute to a broadened magnetic resonance, primarily due to collisional broadening from spin-exchange and wall collisions. These frequency components are shown for example in Figure 1-7 for the case of ^{87}Rb. This broadening is particularly significant in vapor cells utilizing microelectromechanical systems (MEMS) technology, which offer a compact and scalable approach for mass production.

Such errors, commonly known as "heading errors" occur because the magnetic resonance frequency components are influenced by changes in atomic sublevel populations when the sensor's orientation relative to the magnetic field shifts. While increasing the vapor cell size and lowering the temperature can resolve these frequency components (V. Acosta et al., 2006), this approach is incompatible with sensor miniaturization goals.

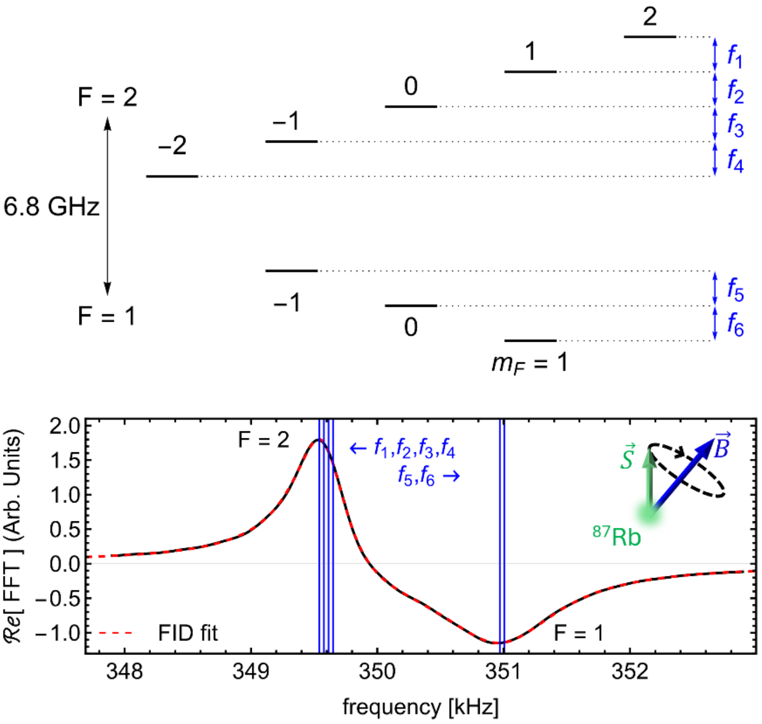

Figure 1-7. Heading error nonlinear Zeeman effect (NLZ)

OPMs based on metastable ^{4}He are immune to NLZ errors due to the involvement of pure electronic spin, which eliminates these frequency uncertainties (J. M. Léger et al., 2015). Potassium-based magnetometers can also be designed to minimize NLZ effects because they have well-separated frequency components that remain distinct across a wide range of vapor cell parameters (Beverini et al., 1998).

Several other methods have been developed to mitigate NLZ errors in alkali-based OPMs. For instance, it has been demonstrated that in high spin polarization regimes, NLZ errors can be accurately modelled to 0.1nT (Lee et al., 2021). Other approaches to reduce heading errors include techniques such as spin-locking (Bao et al., 2018, 2022), light polarization modulation (Oelsner, Schultze, IJsselsteijn, et al., 2019), double-pass configurations (Rosenzweig et al., 2023), double-modulated synchronous pumping (Seltzer et al., 2007), and leveraging tensor light shifts (Jensen et al., 2009). However, these methods often overlook frequency shifts arising from the distinct Zeeman resonances between the F=I±1/2 hyperfine manifolds (Hewatt et al., 2024). Additionally, many methods mitigate NLZ effects by utilizing higher-order polarization moments (V. M. Acosta et al., 2007; Yashchuk et al., 2003; Zhang et al., 2023); however, these approaches are impractical for MEMS vapor cells due to the high buffer gas pressures commonly used in such systems (Rushton et al., 2023).

An alternative approach involves using coil systems around the OPM to mitigate NLZ-related errors by maintaining a weak magnetic field environment (Bertrand et al., 2021; Seltzer & Romalis, 2004), effectively eliminating NLZ effects. However, this method has the drawback of requiring precise calibration of the coil system to achieve the desired accuracy.

Hyperfine structure (HFS) techniques, such as coherent population trapping (CPT) (Ellmeier et al., 2023; Liang et al., 2014; Pollinger et al., 2018a) and direct microwave interrogation (Aleksandrov et al., 2006; C. H. Kiehl, 2024), have emerged as promising solutions for achieving high scalar accuracy, even in the challenging environment of MEMS vapor cells. These methods eliminate heading errors caused by NLZ effects by resolving Zeeman shifts between multiple hyperfine transitions. Among these, CPT offers significant advantages, including all-optical operation, which enables miniaturization and reduced power consumption. However, CPT measurements typically exhibit lower sensitivity and are more susceptible to light shift effects compared to direct microwave interrogation (Batori et al., 2022).

The various techniques and their reported accuracy are summarized in Table 1-5.

Table 1-5. Techniques for high scalar accuracy.

Technique	Scalar accuracy (nT)
High spin polarization (Lee et al., 2021)	0.1
K OPMs (Beverini et al., 1998)	< 0.1
Coil system with near zero-field environment (Bertrand et al., 2021; Seltzer & Romalis, 2004)	< 0.1
Alignment resonances (Zhang et al., 2023)	NR
He 4 alignment detection (J. M. Léger et al., 2015)	0.05
HFS magnetometry (e.g. CPT (Ellmeier et al., 2023; Liang et al., 2014; Pollinger et al., 2018a) and µw detection (Aleksandrov et al., 2006; C. H. Kiehl, 2024))	< 0.2

1.1.3 Vector OPMs

Measuring the magnetic field vector requires an external reference, making component accuracy inherently susceptible to machining tolerances and sensor drift. In vector OPMs, this reference is typically a coil system (Gravrand et al., 2001), though alternative methods leveraging atomic interactions with electromagnetic fields for vector operation are discussed further in Section (). Other vector magnetometers, such as fluxgates (Auster et al., 2009; Koch & Rozen, 2001), magneto-resistive (Liu et al., 2012), Hall sensors (Karsenty, 2020; Nhalil et al., 2019), and superconducting quantum interference devices (SQUIDs) (Clarke, 1989; Dantsker et al., 1994), are mounted orthogonally to directly measure individual magnetic field components and reconstruct the full magnetic field vector. For high-accuracy applications, vector magnetometers rely on an OPM as a scalar reference for ground and in-flight calibration to maintain precision and compensate for drift (J. M. G. Merayo et al., 2000). Vectorizing an OPM offers the potential to eliminate the need for multiple sensors, improving overall SWaP while leveraging state-of-the-art OPM techniques to enhance vector sensitivity and accuracy.

This section is structured as follows: an overview of different types of vector OPMs, an identification of the most promising examples, and a comparison between space-based fluxgate technology and state-of-the-art vector OPMs.

1.1.3.1 Types of vector OPMs

Vector OPMs can be categorized into two types. The first, and most common and reliably accurate, are OPMs that rely on scalar detection with respect to the magnetic fields produced by a coil system. The vector accuracy of these techniques is generally limited by the calibration accuracy of coil system parameters such as coil factors and coil pair orthogonality diagrammed in Figure 1-8. These approaches include a directional varying reference field (variometer) (Aleksandrov et al., 2006; Alexandrov et al., 2004; Alldredge, 1960), fast rotating fields (T. Wang et al., 2023), low-frequency coil modulations (Andryushkov et al., 2022; Gravrand et al., 2001; J. M. Léger et al., 2015), and zero-field nulling (Bertrand et al., 2021; Seltzer & Romalis, 2004). Coil modulation is a well-established approach that has been implemented with a ^{4}He OPM in the European Space Agency SWARM mission (J. M. Léger et al., 2015) or in the NanoMagSat mission (J.-M. Léger et al., 2022a). That type of sensor reached 10 µrad directional accuracy after a calibration involving multiple sensor rotations (Gravrand et al., 2001).

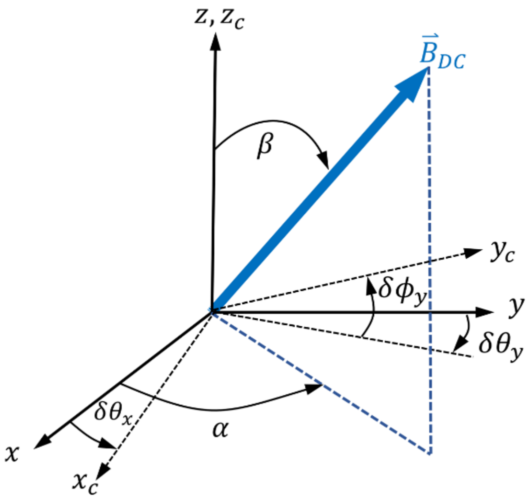

Figure 1-8. Schematic of the non-orthogonal coil coordinate frame $C=(x_c, y_c, z_c)$ with respect to an orthogonal laboratory frame $L=(x, y, z)$ relevant for vector OPMs employing scalar detection with respect to magnetic fields produced by a coil system. Necessary calibration parameters are three non-orthogonality angles$(\delta\theta_x, \delta\theta_y, \delta\phi_y)$, three coil factors, and three background field components.

Vector magnetometry via scalar detection combined with a coil system presents certain technical challenges. The first challenge is that the vector sensitivity degrades with increased background magnetic field strength for the same modulation depth of the coil field. Moreover, in some cases weak modulation fields are necessary due to power requirements, to prevent coupling to external objects, and slew-rate limitations of coil feedback electronics (Zhang Rahul Mhaskar Geometrics, 2019). For instance, by employing modulation depths of around 18 μT, vector component sensitivities down to 0.4 pT/√Hz have been achieved, as reported in (T. Wang et al., 2023). Conversely, in the SWARM mission, vector component sensitivities are restricted to 1 nT/√Hz a limitation attributed to the smaller modulation depths of 50 nT, as detailed in (J. M. Léger et al., 2015).

The second type of vector OPM is one that uses an electromagnetic field as its vector reference, by coupling the atomic ensemble to its polarization structure or propagation direction and offers some advantages over coil modulation approaches. This type can be further divided into whether the technique is all-optical vector or uses external RF or microwave fields. All-optical methods, such as electromagnetically induced transparency (EIT) (Gonzalez Maldonado et al., 2024; Yudin et al., 2010), nonlinear magneto-optical rotation (NMOR) (Meng et al., 2023; Pustelny et al., 2006), and methods that detect spin projections on multiple laser beams (Afach et al., 2015a; Fairweather & Usher, 1972; Patton et al., 2014; Petrenko et al., 2023; Zhang et al., 2021; Zhivun et al., 2014), are attractive because they enable remote detection, are magnetically quiet, and are compatible with sensor miniaturization. Methods that utilize radio-frequency fields include are double resonance atomic alignment (Ingleby et al., 2018; Weis et al., 2006), and the Voigt effect (Pyragius et al., 2018). Alternately, a microwave-based technique that probes hyperfine transitions with Rabi oscillations has been demonstrated (C. Kiehl et al., 2025). Unlike coil system modulation techniques, these approaches do not gain vector information from a modulation in the magnetic field strength, except for (Patton et al., 2014) but resonantly probe atomic transitions. Thus, by tuning the electromagnetic frequency their vector sensitivity does not degrade at large DC magnetic fields.

Notably, as demonstrated in (C. Kiehl et al., 2025), type 2 vector OPMs employing Rabi oscillations extract more detailed information about the vector system compared to the scalar measurements obtained from type 1 coil modulation techniques. This additional information has been proposed to enable drift detection and potentially facilitate real-time calibration without requiring sensor or bias field rotations, which often lead to unnecessary downtime. Consequently, type 2 vector OPMs hold the promise of correcting systematic errors caused by drift without introducing calibration-related interruptions. However, this concept remains to be fully validated in a sensor beyond the scope of drift detection.

Despite these advantages of type 2 vector OPMs, achieving vector accuracy better than 1-degree (17 mrad) with an electromagnetic reference is a nontrivial task due to challenges in modelling the nonlinear directional dependence of the atomic measurements (S. J. Ingleby et al., 2018; McKelvy et al., 2023; Meng et al., 2023; Petrenko et al., 2023; Zhang et al., 2021). Furthermore, most reports on vector OPMs using an electromagnetic reference focus solely on sensitivity characterization, leaving vector accuracy underexplored. Major contributing factors to modelling inaccuracy are sensitivity to complex decoherence effects from atomic collisions, imperfect optical pumping, and characterization errors of the electromagnetic reference in terms of spatial inhomogeneity, polarization structure, and time-dependent drifts.

Table 1-6. Vector OPM techniques

Categorization	**Technique**	**Vector component**	**Vector component accuracy (nT)**	**Bandwidth (Hz)**

		sensitivity (pT/√Hz)		
Coil system + scalar detection	Fast bias field rotations (T. Wang et al., 2023)	0.3	0.14	30
	Variometer (Vershovskii et al., 2006)	4.5	0.15	5
	Low-frequency coil modulations (Leger, 2009)	1000	1	0.4
	Zero-field nulling (Bertrand et al., 2021a)	0.13	NR	1000
Electromagnetic vector reference: all-optical	Vector light shifts	25000	NR	3
	Spin-projections on multiple laser beams (Petrenko et al., 2023)	20	NR	180
	NMOR (Meng et al., 2023)	10000	5	16
	EIT (Gonzalez Maldonado et al., 2024)	4363	870	10
Electromagnetic vector reference: μw/RF	Voigt Effect	1.2	NR	62.5
	Double-resonance atomic alignment	NR	NR	NR
	Rabi frequencies (Kiehl, 2025)	2500	23	3.3

1.1.3.2 Identification of notable vector OPM techniques

We classify notable vector OPM techniques into two categories. The first category includes coil-based techniques, which are the most readily implementable for geomagnetic and space applications. These methods have already demonstrated state-of-the-art vector sensitivity and accuracy in experimental settings. The second category consists of all-optical vector OPMs, which offer advantages over coil-based techniques such as low SWaP and zero cross-talk in addition to demonstrating state-of-the-art vector and scalar sensitivity. However, their vector accuracy has yet to be thoroughly demonstrated and studied, and many have only been tested in large glass-blown vapor cells a few centimeters in size rather than in microfabricated cells. As a result, while these emerging techniques present a promising research direction, they are not yet suitable for immediate deployment in geomagnetic and space applications.

1. In the first category, a ^{4}He zero-field vector OPM (Bertrand et al., 2021a) achieved state-of-the-art vector component sensitivity of 130 fT/√Hz, a ±70 μT dynamic range, and 1 kHz bandwidth in a ~1.5 cm vapor cell. While no accuracy evaluation was reported, this technique is expected to achieve directional accuracy within 10 μrad (< 0.5 nT).

2. Another notable example is a coil-based vector OPM employing high-frequency (~1 kHz) rotating magnetic fields (T. Wang et al., 2023). This sensor demonstrated a scalar sensitivity of 35 fT/√Hz, a vector component sensitivity of 300 fT/√Hz, and a vector component accuracy of 140 pT, along with a 30 Hz bandwidth in a 5 mm vapor cell. However, since this technique is FID-based, it still suffers from deadzones. Recent advancements in miniaturizing coil systems (Tayler et al., 2022) are particularly relevant for designing low-SWaP sensors in this category.

In the second category, several all-optical techniques show promise for vector measurements compatible with miniaturization, zero cross-talk, low SWaP state-of-the-art sensitivity, but require further validation for vector accuracy:

1. Bell-Bloom Vector OPM with Orthogonal Beams (Petrenko et al., 2023): This method utilizes two orthogonal laser beams, where the amplitude and phase information is used to reconstruct the full magnetic field vector. It achieves a scalar sensitivity of 16 fT/√Hz and a vector component sensitivity of 0.4 μrad/√Hz (20 pT/√Hz at 50 μT) at 180 Hz bandwidth in an 8 mm vapor cell. While not explicitly reported, this technique should be compatible with deadzone-free operation.

2. Modulated Vector Light Shift OPM (Patton et al., 2014): This approach uses modulated vector light shifts from two orthogonal beams to drive atomic spins, achieving a scalar sensitivity of 50 fT/√Hz and a vector sensitivity of 0.5 mrad/√Hz (25 nT/√Hz at 50 μT) in a 5 cm vapor cell. The authors suggest that their sensitivity was limited by technical noise, and in principle, vector sensitivity could be improved to the μrad/√Hz level. Related work has demonstrated a similar setup operating as a scalar magnetometer without deadzones, using fictitious radiofrequency (RF) fields to drive atomic spin.

3. Multi-Beam Absorption-Based Vector OPM (Afach et al., 2015b): Based on the principle reported by Fairweather and Usher (1972), this method reconstructs the full magnetic field vector by analyzing the absorption signals from four circularly polarized laser beams oriented in different directions. Stability tests demonstrated a scalar resolution of 300 fT for integration times ranging from 80 ms to 1000s, with the best scalar measurement reaching 80 fT for integration times between 1.6 and 6 seconds. The magnetic field direction was measured with a resolution better than 10 μrad for integration times between 10s and 2000s. These measurements were performed in a 4.5 cm paraffin-coated spherical vapor cell. The technique employed an RF field for π/2 spin rotations before measurement, though Bell-Bloom optical pumping could potentially be incorporated into this approach.

1.1.3.3 Space Fluxgate overview and vector OPM comparison

Fluxgate magnetometers have been widely used in space missions due to their reliability and stable performance under varying environmental conditions and over time. Their extensive use in non-space applications has further established confidence in their effectiveness. These instruments are intrinsically sensitive to the direction of external magnetic fields, making them the preferred choice for vector measurements (Bennett et al., 2021). Additionally, fluxgates are capable of measuring across a large dynamic range, which is advantageous for many mission requirements.

However, fluxgate magnetometers are not absolute by design and thus require external calibration to derive accurate estimates of weak field components within strong magnetic fields. Although pre-launch calibrations (e.g. temperature drifts, zero-offset, among others) are typically conducted on Earth, in a fluxgate magnetometer, an additional source of zero error arises after the launch if the high-permeability core retains any residual or permanent magnetization. Further calibration can be achieved through various methods, such as using an external Absolute Scalar Magnetometer (ASM) (Dougherty et al., 2004; Fratter et al., 2016) or applying software-based corrections with reference data from other onboard devices (Balogh et al., 2001).

Over the years, the accuracy of fluxgate magnetometer data has significantly improved with the introduction of Absolute Scalar Magnetometer (ASM) measurements (see Figure 1-9). Early space missions did not employ ASM for fluxgate calibration. It was not until the Explorer X mission in 1961 that a rubidium magnetometer was incorporated, enabling accurate determination of zero-level shifts (Heppner et al., 1963). However, as mentioned earlier, the rubidium magnetometer experienced operational issues during the mission.

In recent years, the development of ^{4}He magnetometers and coherent population trapping (CPT) magnetometers has further enhanced accuracy. For instance, during the Cassini mission, the combination of a ^{4}He magnetometer and a fluxgate magnetometer proved particularly effective. The vector mode of the ^{4}He magnetometer optimized low-frequency measurements in low magnetic fields, while the fluxgate performed better at high frequencies and across a wider dynamic range. Additionally, the scalar mode of the ^{4}He magnetometer enabled precise absolute calibration of the fluxgate, reducing its measurement error to 1 part in 10^5 (Dougherty et al., 2004). Another example is with the China Seismo-Electromagnetic Satellite (CSES), where they used a CPT magnetometer in conjunction with two fluxgate sensors. The entire setup reached an accuracy of 0.19nT (Pollinger et al., 2018a).

Another in-flight calibration technique involves evaluating external sources of error that arise during the mission. Notably, the Cluster mission does not use an Absolute Scalar Magnetometer (ASM) as a reference to calibrate the three onboard fluxgate magnetometers. Instead, it relies on the Geocentric Solar-Ecliptic (GSE) coordinate system. By combining this coordinate framework with the digitized vector measurements from the fluxgates, the system can recalibrate the devices, claiming to achieve an accuracy of approximately 0.1 nT (Balogh et al., 2001).

However, this process is complex and depends on various external factors. These include the scale factors and offsets of the sensors and fluxgate electronics, previous on-ground calibrations, spacecraft-induced offsets, delays, bandwidth limitations, the performance of Analog-to-Digital Converters (ADCs), and the digital filtering process, among other considerations (Balogh et al., 2001). As mentioned earlier, size, weight, and power (SWaP) are important factors for sensors used in space missions. Table 1-7 shows examples of SWaP for both OPMs and fluxgate magnetometers, including those used in space and commercially available models. Improving SWaP would allow satellites to carry more scientific instruments. This is especially important for small spacecraft like CubeSats, which have limited space and power.

Advances in OPM miniaturization show great promise towards the stringent SWaP requirements. As explained in Section 1.1.2.3, microfabrication techniques, such as microfabricated components and miniature coils (Raghavan et al., 2024a), could be used to make space magnetometers smaller and more efficient.

In terms of commercialization, Table 1-7 highlights the limited availability of commercial vector OPMs, as they require further research and development. Nevertheless, this is an emerging field with significant potential. For instance, Quspin's SWaP characteristics are more favorable in comparison with other devices used already in some missions (e.g. SWARM mission). Although Quspin's magnetometers have not yet achieved the sensitivity levels of other devices, they claim their instruments exhibit no noticeable drift, unlike fluxgate magnetometers. In addition to this example, there are other techniques that are still in laboratory stage which have shown long stability on scalar OPM (Bison et al., 2018; Wilson et al., 2019), which could be potentially expanded to a vector magnetometer.

Table 1-7. Comparison between commercial and space magnetometers

	Sensor	**Sensitivity (pT/√Hz)**	**Size**	**Weight (g)**	**Power (W)**
Commercial	QUSPIN / QTFM Gen-2	100	17.7 x 19.8 x 35.8 mm	12	2.5
	Bartington / Fluxgate Spacemag-Lite	50	20 x 20 x 20 mm	67	0.175
Space	Swarm / ^{4}He	1	NR	1000	1
	Swarm / Fluxgate	6.6	NR	3000	5.3

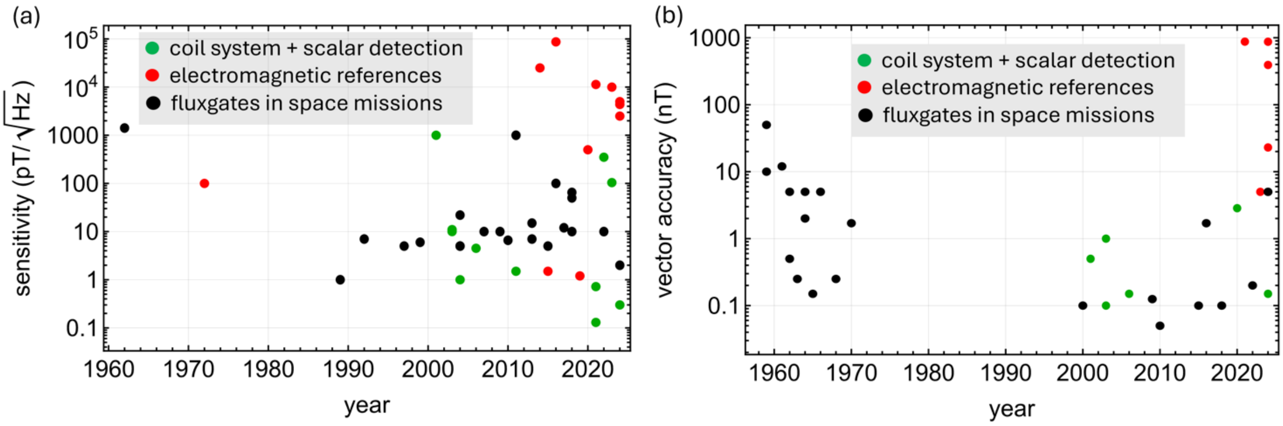

Figure 1-9. vector OPM sensitivity and accuracy over the last six decades

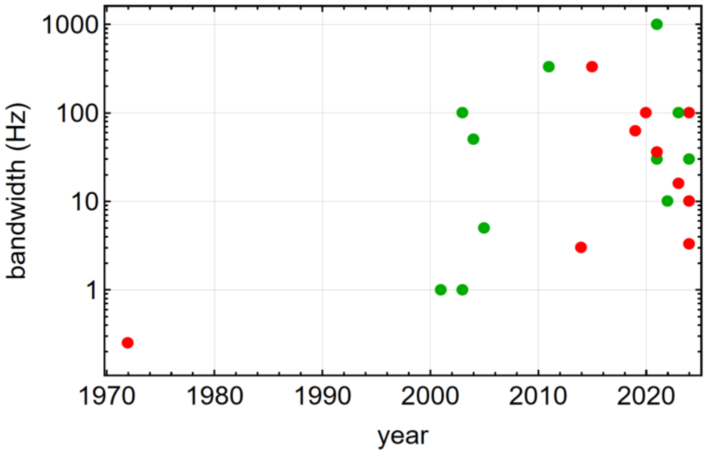

Figure 1-10. vector OPM bandwidth over the last six decades

As shown in Figure 1-9, OPM technology has surpassed the sensitivity of space fluxgate magnetometers over the past 20 years, achieving even sub-pT sensitivities in Earth's magnetic field (Bertrand 2021; Li 2021). OPMs have also improved in bandwidth (see Figure 1-10), allowing for a wider range of measurements (Li 2021, Bertrand 2021, Gravrand 2001). However, the current level for vector accuracy of fluxgates has not yet been reached by optical magnetometers. This aspect is still not fully understood, and further research is needed (Kiehl, 2025).

1.1.4 Conclusion

This article has presented state-of-the-art techniques for both scalar and vector OPMs, focusing on key performance metrics such as sensitivity, accuracy, bandwidth, SWaP, and deadzone-free operation. By analyzing the evolution of these performance metrics in the literature, we find that OPM technology has steadily advanced across all key parameters. Notably, vector OPMs can now achieve better sensitivity than state-of-the-art fluxgates deployed in space. However, their vector accuracy remains comparable, as this aspect has been relatively understudied in vector OPM research. These state-of-the-art techniques are summarized in Figure 1-11. In principle, the most effective sensor design would integrate a combination of these methods.

As illustrated in the Figure 1-11, some missions have already demonstrated successful combinations of these approaches. The Swarm mission, for example, combined a ^{4}He scalar magnetometer with low-frequency coil modulations to eliminate deadzones while maintaining high scalar and vector accuracy. Similarly, the CSES mission employed CPT as a hyperfine structure (HFS) technique to achieve a deadzone-free, high-accuracy scalar magnetometer. Many other promising technique combinations remain unexplored. Among laboratory research efforts, vector nulling has emerged as a strong candidate for achieving both high vector sensitivity and accuracy while being readily deployable with existing technology and experimental methods.

At present, all-optical vector OPMs lag behind coil-based vector OPMs in vector accuracy. However, they offer several potential advantages, including reduced SWaP, elimination of cross-talk, and improved calibration protocols. Further research in this area could significantly enhance not only space and geomagnetic applications but also a broader range of sensing technologies.

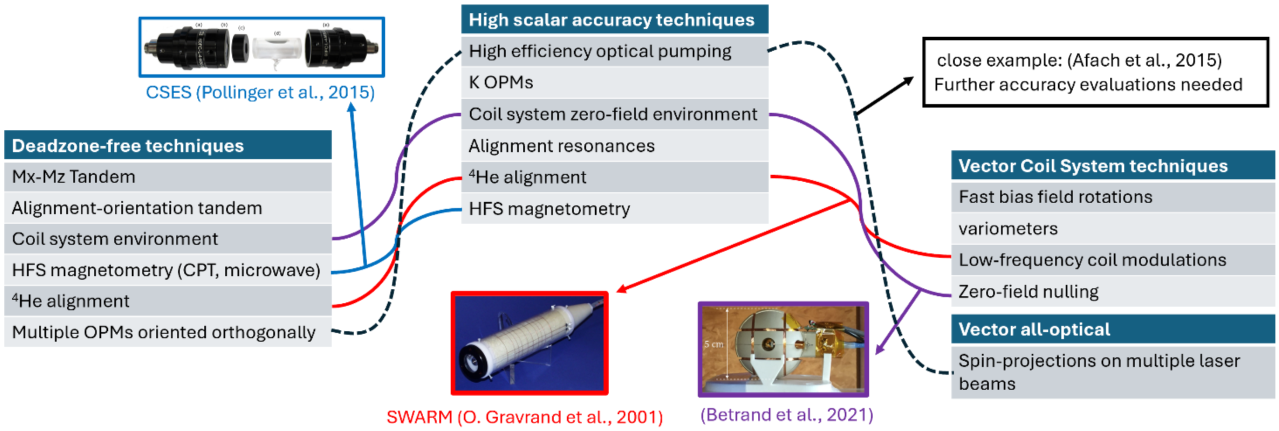

Figure 1-11. Diagram of state-of-the-art techniques for high scalar accuracy, dead-zone-free, and high vector accuracy.

1.2 Scientific spaceborn earth observatoin magnetometry

1.2.1 Introduction

Spaceborne magnetometers on satellites changed our view on Earth in understanding the magnetic field interactions around the Earth with the environment, with fluids, gas, with plasma and waves. This chapter gives an overview of the scientific targets of interest reachable by using near-Earth magnetic field readings with their various general properties and caveats, followed by the recent history of relevant and used spaceborne magnetometry. Finally, this report gives an overview of actual lessons learned about the general limitations of spaceborne magnetic field investigation, which occurs during various attempts to get real spaceborne magnetic field readings ready for further scientific exploitation.

1.2.2 Intentions

This first part is a brief tour covering the possible objectives of spaceborne magnetometry. The most important distinction is between internal and external sources and physical systems of the Earth. Internal sources of magnetic field parts are created below the surface of the Earth, inside the solid Earth, and external above. But these sources, are, not independent. The external current systems exist without the major core field contribution, part of the internal contributions (in particular induced fields) is caused by the broad set of external fields and their variations.

1.2.2.1 Objectives for spaceborne magnetometry

A review on spaceborne magnetometry was given by (Olsen & Stolle, 2012). The first two images therein will guide us: Figure 1-12 gives an overview on the various sources and current systems in or near the Earth involved in creating the combined measurable magnetic field signal – and in a second view outlines the behaviour of those contributions in spatial and frequency domain (Figure 1-13).

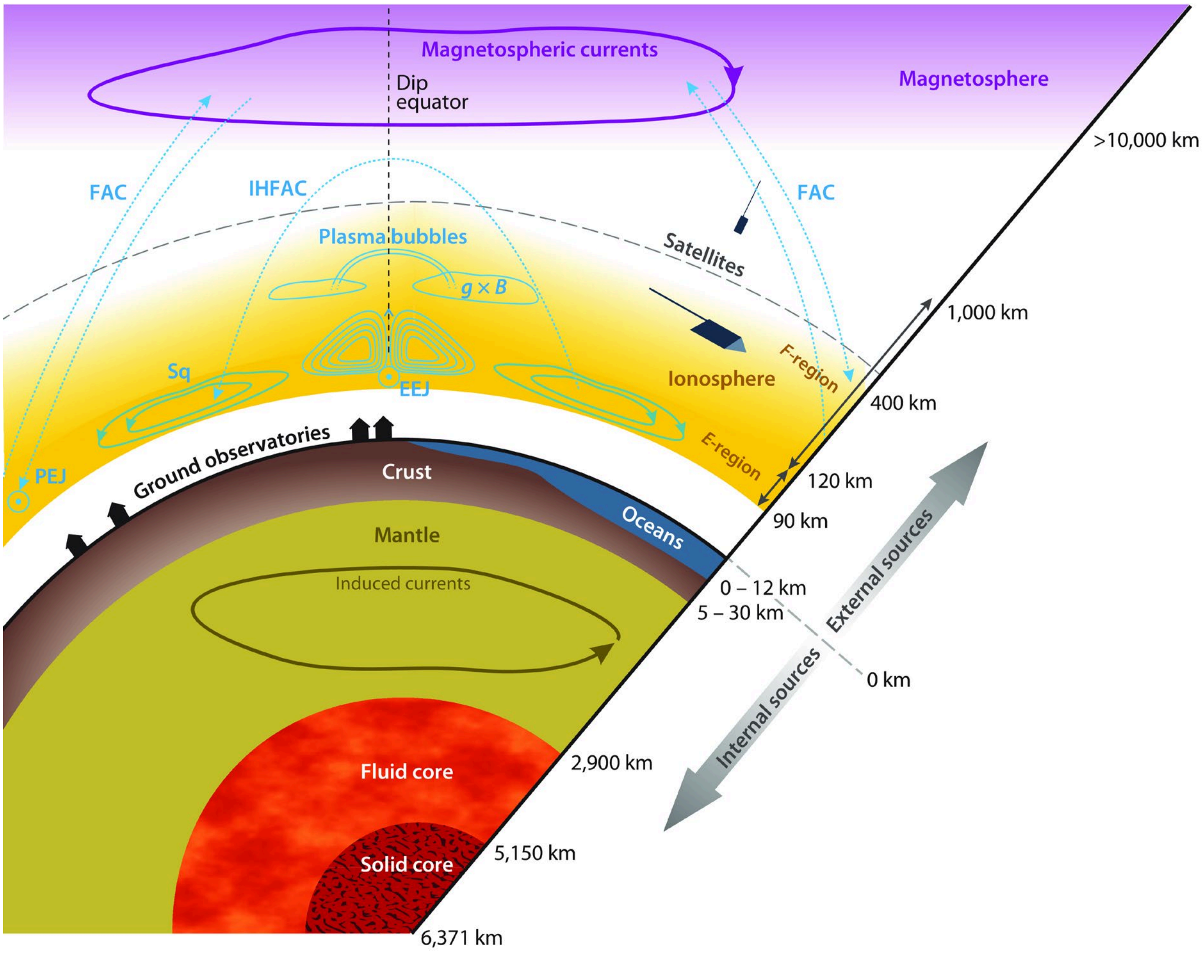

Figure 1-12: (Olsen & Stolle, 2012), p. 446; original legend removed, see text.

1.2.2.1.1 Physical objects

In general, this distinction between internal and external sources may be disputable. The often-used spherical harmonic expansion to describe an averaged magnetic field model depends for this discrimination in a mathematical, not a physical sense, on the altitude of the measurement. For ground observatory data, this altitude limit is, despite the non-spherical geoid and the topographic differences, approximately the surface of the Earth. An advantage is, that the lower neutral atmosphere is approximately a source-free (current free) region. The observatory data are well exposed to the induced fields in the mantle and oceans and still close to current systems in the ionosphere. Spaceborne readings taken above several 100 km kept a larger distance to this source, but are embedded in the ionosphere. The readings cannot be taken entirely outside any source region of magnetic field generation. The dominant main field originates in the fluid outer core, a field component expected to be mostly dipolar, as long we are not in an epoch of a reversal or excursion. Of main interest is the field topology itself but in particular the first derivative in time, the Secular Variation (SV). This signal can be used to understand the dynamical processes, in combination with other signals from deep Earth-like seismic sounding or the significant length of day variation (SOD). As signals under dispute are the detection and interpretation of regional or global so-called Jerks, sudden and short-period changes of the SV. The non-zero conductivity of the Earth's mantle and the oceans (mostly by their salinity) allows a look under the surface for otherwise hidden parameters. The large-scale variations of external field contributions on certain timescales are inducing currents in the mantle and ocean. The ocean flow is a fairly small signal. In particular, some tidal components can be filtered out in the frequency domain (Grayver et al., 2024). Another source is the field of the lithospheric field, which is, assuming crustal levels below the Curie temperature, taken as a mostly static contribution. To map this information, external field contributions need to be removed, so low external field activity and a very low orbit are desired. These prerequisites were fulfilled in the late period of the CHAMP mission by the unexpected deeply quiet and elongated long phase around the onset of Solar Cycle period number 24. Further larger scale phenomena of interest at ionospheric reign are the Equatorial electrojet (EEJ), see climatological studies by (Lühr et al., 2012; Soares et al., 2022; Yamazaki et al., 2024; Zhou et al., 2020), Polar and Solar quiet current systems and IHFAC (inter-hemispheric field-aligned current), see (Park, Stolle, et al., 2020; Park, Yamazaki, et al., 2020). Other field-aligned currents (FACs) in high latitude regions above 60 degrees have smaller scales and plasma bubbles as well. The most prominent external, magnetospheric current system is the large-scale ring current (RC), and the other effects induced by solar activity, like geomagnetic storms, coronal mass ejections (CMEs) and waves occurring by interaction of the magnetic force and the plasma.

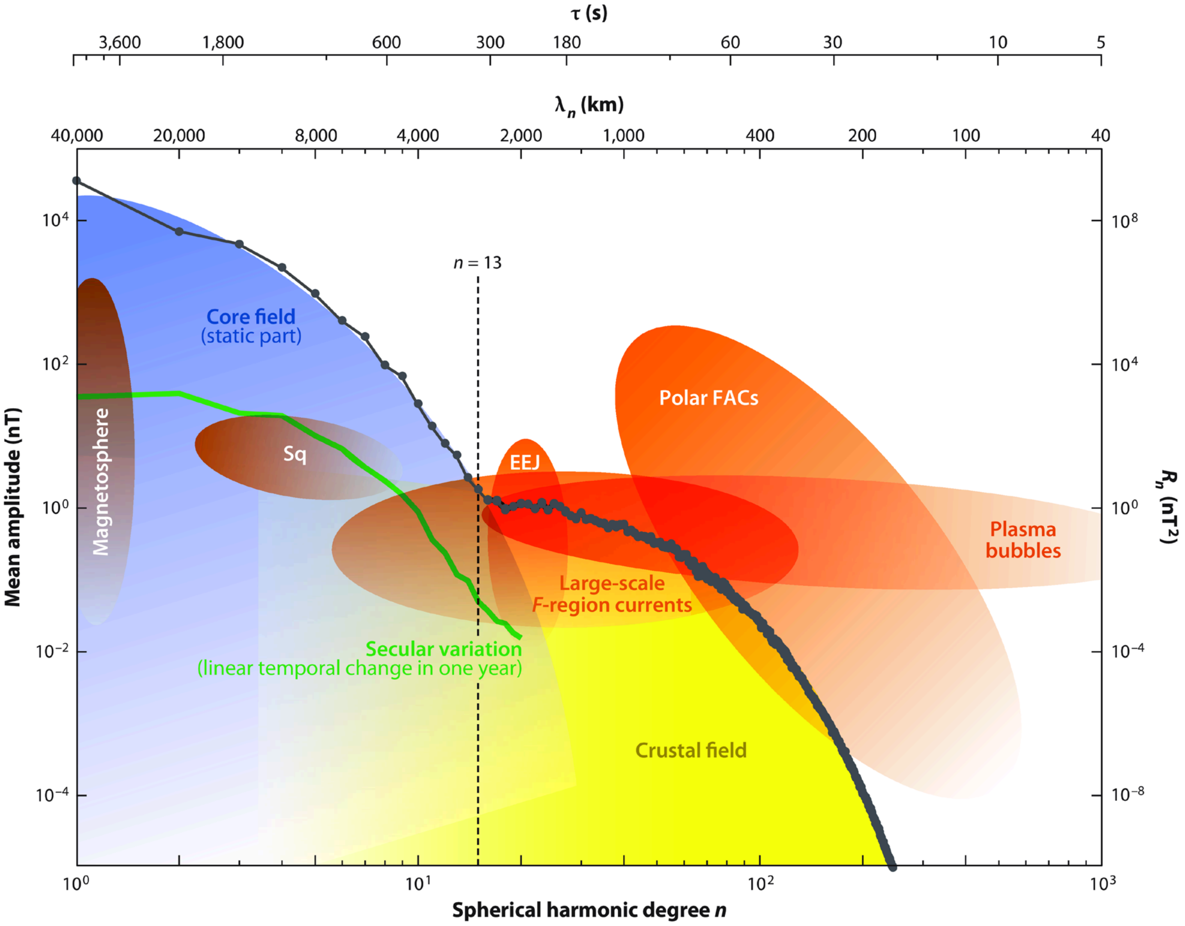

Figure 1-13: Frequency and spatial realms, Olsen and Stolle (2012), p. 447, original legend removed, see text.

Figure 1-13 from Olsen and Stolle (2012), maps the various physical signals in a graph of signal Amplitude over spherical harmonic degree, as a spatial scale factor proxy for the most common description of physical phenomena in spherical geometries. The right scale displays the translation of the amplitude axis in the corresponding power, the upper scales for the SHA-degree to the corresponding length scales and their significant times τ, the usual Low Earth Orbit (LEO) satellite velocity of about 8-9 km/s given. As the various populations are heavily overlapping, it is a challenge to distinguish between the signals originating from the various source regions. Only a very good local time (LT) coverage and the use of constellation between satellites or with ground observatories or close occasional encounters of satellites can help, for example, to distinguish between. With the advent of human technology in orbit and sensitive large-scale infrastructure on the ground and in orbit, Space Weather monitoring (in particular real-time or near real-time) gains more interest.

1.2.2.1.2 Modelling internal fields

In particular for modelling internal fields, the stability of instrument parameters influences the reachable accuracy. Non-stable parameters need an in-flight calibration. For lithospheric studies also low orbits in a quiet solar cycle period are needed. Due to the high velocity of satellites along the orbit, the position and absolute timing need to be known in excellent reliability, down to fractions of milliseconds. These vector readings are essential for accurate scientific analysis because the well-known Backus effect prevents a unique internal model field solution when relying solely on scalar readings. The Backus effect arises from the mathematical limitations of using only scalar (magnitude-only) measurements, which do not provide enough information to distinguish among possible internal magnetic field configurations. Without vector data (which include both magnitude and direction), multiple field structures can produce the same scalar measurements. As a result, no matter how dense or widely distributed a set of scalar readings is, it is generally impossible to determine a unique internal field model. There were efforts to establish workarounds (see for example (Holme et al., 2005; Schneider et al., 2018)). But vector readings need excellent attitude information, as vector information requires not only valid position information (for a velocity of the ground projection of about 8 km/s). Vector readings are most useful only in Earth’s related reference frames (ECEF, Earth Centered, Earth fixed), various coordinate transformations between local S/C coordinate systems and physical systems (celestial systems and ECEF) require high accuracy in attitude down to single arc seconds and very precise absolute time information. Gaps, in particular, if occurring in any systematic way, are not welcome for global models, neither in time or local time nor in spatial coverage. That’s true even if the time resolution required is moderate only (1 Hz or fractions of it) for global core field modelling. systematically occurring larger gaps (for example by S/C intrinsic effects of sun directions, power and solar-cell current distortions on terminators) may render a global field modelling invalid.

1.2.2.1.3 External fields

For the observation of external magnetic fields presumably higher sample frequencies are necessary. Besides the timing issue, requirements of stability and accuracy of the readings may not be explicitly crucial. Constellations are very useful (see ’Cluster’, Swarm A/C and B, NanoMagSat). For core or lithospheric fields or mantle conductivity, modelling is still affected and degraded by the tangled and mostly unpredictable effects of external field contributions.

There are two methods to handle external field contributions, noise in that respect, for global geomagnetic internal field modelling. One method is reducing the scope, i.e. limited nightside data and using selected geomagnetically very quiet periods only. The other method is to model and predict the unknown external field contributions. The latter approach needs good LT coverage.

1.2.2.2 On the physical environment

If an LEO satellite is used for geomagnetic internal field modelling, sample frequencies of and below 1 Hz may be sufficient, but on the other hand, the stability and total accuracy of the vector readings are crucial. Modelling will need good vector measurements with an excellent and reliable attitude and full global coverage. If lithospheric anomalies are in focus, at least about 1 Hz usable sampling may be required. But also, besides full global coverage and accuracy, repeat orbits and low altitude. E.g., CHAMP's final phase in the extended quiet period on the border between solar cycle number 23 and 24. For ionospheric phaenomena, additional good coverage of all activity levels can be useful for statistical (aka climatological) studies. For an example of Plasma bubble events see Stolle et al., 2024. If an LEO satellite is foreseen for ionospheric field prospection or listening to the magnetospheric footprints, sample frequencies far above 1 Hz (10, 50, 250) may be useful, for example for small-scale FAC calculations by constellations or for wave detection. For such statistical studies regular, in particular, gap-free readings are required. For a magnetospheric sounder, i.e. fitted to detect Alfven-waves, but also Whistlers (see the presentation poster by (Coïsson et al., 2024)) higher sample frequencies are required.

1.2.2.3 First objective: Models

Early attempts to model the main field were snapshot models, driven by short coverage in time (as for the short-lived Magsat mission). But with the advent of continuous readings on satellite altitude, it was possible to cover longer periods in time without gaps by a continuous description of the temporal behaviour, probably as a set of partly smooth, splined Spherical Harmonic Expansion coefficients. These continuous models use external field descriptions as a function of various indices provided by other sources and approaches to describe the geomagnetic activity. Prominent examples of models used in the community, with fairly different characteristics, are: the International Geomagnetic Reference Field (IGRF), given since 1900, but not differentiable as piece-wise linear, is today a large community effort, repeated in a five-year interval. In early winter of 2024, the IGRF-14 was published as a derivation from delivered candidate models of already about 20 groups working with various geomagnetic data sources, from miscellaneous satellites to ground observatories, and various methodological approaches. CHAOS: A multi-satellite data model, for the period 1997 – present, updated, meanwhile, a few times a year, used as a multi-tool, as a common reference model for further scientific investigations, in particular further SV and external field studies. But CHAOS is not the only recent advanced and smooth, differentiable model; we have also internal field models from POMME- or GRIMM- (i.e. Mag.num) and also Kalmag-type (Baerenzung et al., 2022), with different approaches to handle the time dependence, ways to extract valuable data information and how to take care of data properties and their uncertainties. We have to ensure, that such global reliable and usable reference models can be created. Otherwise, even a vast bulk of spaceborne readings may get useless.

1.2.2.4 Further example objective: Space Weather

Besides the climatological descriptions of properties of the geomagnetic field in numerical descriptions of the average geomagnetic field behaviour, real-time or near-real-time availability of satellite readings and indices gain the most interest. It allows the global monitoring of the various field sources in unprecedented detail and notably topicality in space and time. Besides the modern satellite measurements, an example is the geomagnetic Hp30 index (back to 1985) as an alternative description of the traditional Kp index (back to 1932), with higher time resolution and available in near real-time. Also, the Swarm mission developed recently a processed data product series, which is available in a range of hours, not days after the fact – opening new applied scopes.

1.2.3 History

1.2.3.1 Overview

Table 1-8 : Overview of dedicated magnetic scientific missions.

Satellite Name	Mission Duration	Inclination in degree	Altitude in km	High-Precision Measurements
OGO-2	1965 – 1967	87	410 – 1510	Scalar
OGO-4	1967 – 1969	86	410 – 910	Scalar
OGO-6	1969 – 1971	82	400 – 1100	Scalar
Magsat	1979 – 1980	97	325 – 550	Scalar and vector
Ørsted	1999 – 2014	97	650 – 850	Scalar and vector
CHAMP	2000 – 2010	87	260 – 450	Scalar and vector
SAC-C	2001 – 2004	97	698 – 705	Scalar
Swarm	2013 ongoing	88/87	530 – 450	Scalar and vector

Satellite Name	Mission Duration	Inclination in degree	Altitude in km	High-Precision Measurements
CSES	2018 +5 ongoing	97.4 (SSO)	507	Scalar and vector
MSS-1	2023 ongoing	41	450	Scalar and vector
NanoMagSat	2027 -	two at 60	575	Scalar and vector

Table 1-9 : Overview of missions utilizing platform magnetometers for scientific objectives.

Satellite Name	Mission Duration	Inclination in degree	Altitude in km	Low-Accuracy Measurements
GRACE	2002 – 2017	89	450 – 500	vector (limited usability)
GRACE-FO	2017 ongoing	89	480 – 506	vector
GRACE-C	scheduled 2028			vector
GOCE	2009 – 2013	96.7 (SSO)	234	vector
Cyrosat-2	2010 ongoing	92 (SSO)	717	vector
DMSP	various – 2014	(SSO)		vector
AMPERE	2010 ongoing	86.4 (6 orbital planes, 30° apart)	780	vector

1.2.3.2 Missions

The experience starts with CHAMP, shown in Figure 1-14, but other missions need to be mentioned: Oersted launched before CHAMP, SAC-C (with Oersted payload), the early Polar Orbiting Geophysical Observatories program (POGO, which used optically pumped rubidium vapour absolute magnetometers), and Magsat from the 1970th. The Magsat sketch is shown in Figure 1-15, as this design is prototypical. The two magnetometers, a (fluxgate) vector magnetometer and two dual-cell, caesium-vapor sensor heads for scalar readings were mounted on a long, flexible and foldable long boom, which grants a certain distance from the noisy satellite body. The attitude accuracy was, despite the fragile boom, already in the range of 10-20 arc seconds, but this would be insufficient for the goals and even the precision provided by modern sensors. Later satellite layouts moved the star camera sensor, shown as essential for proper attitude information, closer to the vector instrument, on a common, stable optical bench. The problems, i.e. changing instrument sources, are well known even decades later (Langel et al., 1982).

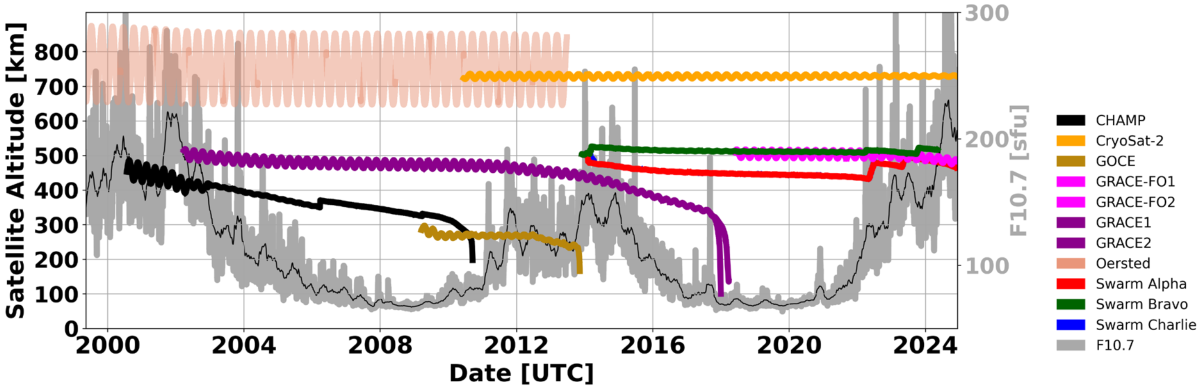

Figure 1-14: Characteristics and altitude of relevant satellites (stage: 2024-12-10).

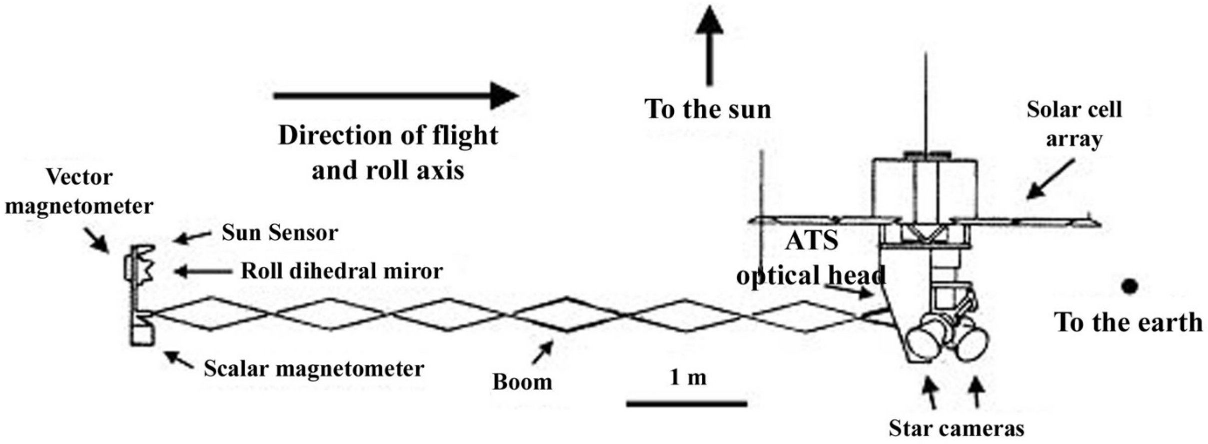

Figure 1-15: Sketch of Magsat (Explorer 61), 1979-1980, unfortunately with a short lifetime of only four months. From Wikipedia (2024).

1.2.3.2.1 Oersted

The Danish satellite Oersted (Thomsen & Hansen, 1999) was launched in 1999 and even the mission was operational at least till 2014, the last vector data available are from 2004. Oersted used a polar orbit with 96.5° inclination and a high altitude and slightly elliptical orbit of ~650-860 km. The outer layout shown in Figure 1-16 is a small box (62 kg) with a deployed, very flexible long boom. The boom was folded into the box during launch and used the gravity gradient as a stabilising influence, otherwise ACS magnetorquers. The instrumentation with a scalar (Overhauser) magnetometer on the boom tip and an optical bench with a one-star imager accompanied by a fluxgate magnetic field sensor (Compact Spherical Coil, CSC) in a gondola two meters apart from the boom tip. The problems were the blinding of the single-star camera, the attitude control, boom vibrations and its thermal stability by self-shadowing. The star camera's limit of operation was an angular rate of 10 deg/min. For details see (Bak, 1999) and (Thomsen & Hansen, 1999); on magnetometer inter-calibration see (Olsen et al., 2003).

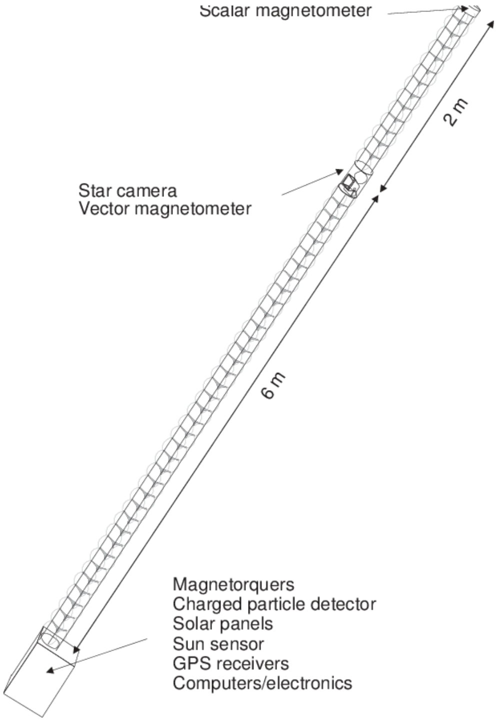

Figure 1-16: Sketch of Oersted satellite.

1.2.3.2.2 CHAMP

The LEO mission CHAMP (European Space Agency, 2012) by DLR and GFZ covered the period 2000-2010 and was manufactured by EADS/Astrium. With an iconic layout and a mass of about 522 kg, it faced multiple targets (gravity, ionospheric sounding, magnetic fields). A sketch of the design an instrument location is shown in Figure 1-17.

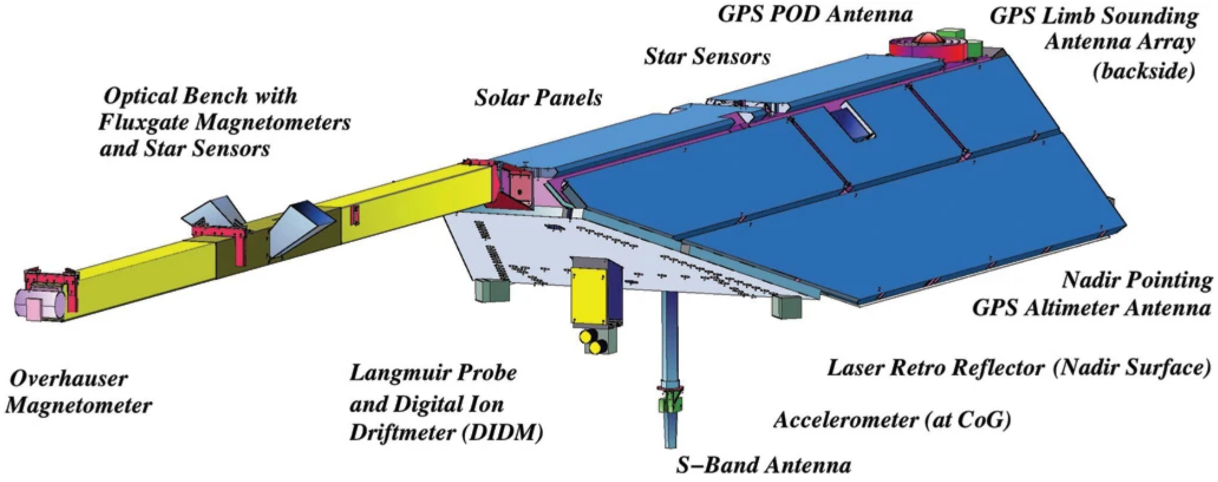

Figure 1-17: Sketch of CHAMP satellite (by GFZ).

CHAMP had, in contrast to predecessors, a fairly stiff boom of about 4 m alone with two vector magnetometers mounted there on an optical bench, accompanied by two of total four-star camera sensors (two other on S/C body), 50 Hz magnetometer readings from a CSC type magnetometer, an Overhauser scalar magnetometer OVM (1 Hz) at the tip. CHAMP was three-axis stabilized with a boom heading in flight direction. Its attitude is AOCS stabilized using magnetorquer and cold gas jets, (but no momentum wheels). Other instrumentations were GPS, Ion-Drift-Meter (DIDM) and Laser reflectors (LRR). The S/C stray field at the point of the vector magnetic sensor was below 0.5 nT, the regular in-flight calibrations used the scalar OVM readings. The scale factor as a result of the in-flight calibration drifted, significantly visible after a few days. See (Yin, 2009), with CHAMP final calibration attempt.

1.2.3.2.3 Swarm

The ESA mission Swarm (Friis-Christensen et al., 2006b)was launched in November 2013 and this mission with three initially identical satellites bit resembling the CHAMP general layout is on-going and currently the reference mission still. A sketch of the design and instrument location is shown in Figure 1-18. All three satellites have (drifting) polar orbits with high inclination of about 87 deg, B with a higher orbit of about 530 km and A and C with about the same altitude of about 430 km, close together (initially side-by-side). It is intended that the satellites with lower orbits, A and C, are going to survive the current solar cycle. The satellites have a stiff deployed long boom with an optical bench with a fluxgate (VFM) and three-star sensors – but the flight direction is inverted compared to the CHAMP mission, the boom is trailing. There are three-star cameras on the optical bench but, in contrast to CHAMP, no sensor on the body. The optical bench is an independent system mounted on top of the boom, whereas for CHAMP it was mounted inside the boom. The absolute accuracy scalar reference for the usual VFM inflight-calibration is given on the tip of the boom by an optically pumped magnetometer with Helium 4 cells (ASM), see (Bertrand et al., 2021b; Jager et al., 2024; Leger et al., 2009). This ASM delivers also (self-calibrating) vector (ASM-V) readings with 1 Hz (see for example (Hulot et al., 2015; Vigneron et al., 2021) and additionally a burst mode of 250 Hz scalar data (Hulot et al., 2024). Unfortunately, all satellites showed the initial error of an unknown source, preventing a proper inflight-calibration. It got obvious soon, that this signal depends on the position of the sun relative to the S/C. The so-called dBSun-effect was finally mostly resolved, and the processing was updated by a heuristic correction model. The true reason was revealed in a combined effort. On Swarm satellite C the operational ASM instrument got lost by radiation in November 2014, the redundant sensor on C was already found not-operational after launch. The constellation (A, C, side-by-side, later also aligned) proved to be very fruitful, but other constellation studies, also with ground observatories (for example with Swarm constellation and SuperMAG, (Dunlop et al., 2024).

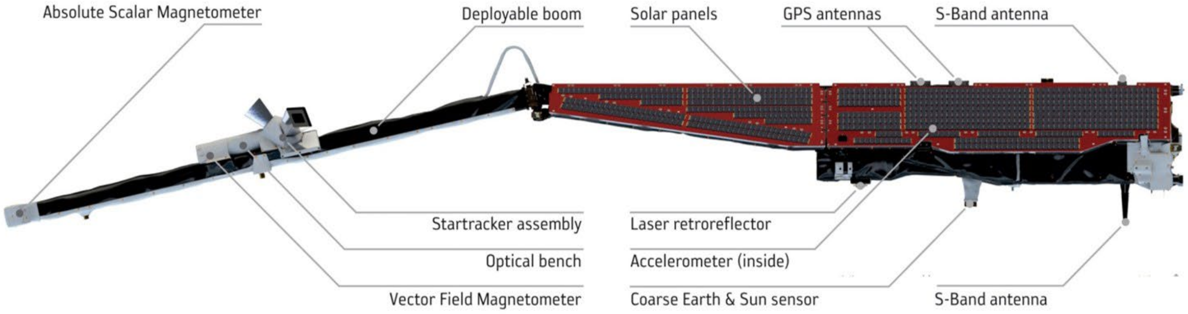

Figure 1-18: Sketch of Swarm satellite (by ESA, https://earth.esa.int/eogateway/missions/swarm#instruments-section).

1.2.3.2.4 NanoMagSat

The NanoMagSat (Figure 1-19) mission is still in preparation (Information mostly taken from websites, https://www.leti-cea.com , https://www.ipgp.fr/, https://www.esa.int/, and (Hulot et al., 2024)). The mission is mostly driven by Gauthier Hulot (IPGP) and initially intended as an Add-On for the Swarm satellite trio A, B, C. NanoMagSat is now a part of the ESA Scout (small satellite) program and will consist of three 16U cube-sats (22x22x44cm, 30 kg) each with a 3 m folded (deployable) boom. The layout is less skinny than Oersted and with an initial altitude of 575 km. NanoMagSat will be equipped with a miniaturised Swarm type (optically pumped) magnetometer (MAM) on a boom tip mounted with two-star cameras on an optical bench for attitude control. There seems an urge to solve the boom problem with a non-magnetic, spring-driven innovative development (Algarra et al., 2023). Other instrumentation will be a multi-needle Langmuir probe (m-NLP), two dual-frequency GNSS and a High-Frequency Magnetometer (HFM) on the boom, but not on the tip. With the British company Open Cosmos as a responsible contractor, the launch is tightly scheduled for 2027. The orbit will be partly non-polar with a 60-degree inclination, only one of the NanoMagSats is foreseen for a polar orbit. The AOCS will probably be challenging, as the platform is gravitationally stabilized and no onboard thrusters will exist. But the miniaturising and the subsequently reduced mass load on the boom may help. The star tracker µASC promises to provide the magnetic field in arc seconds attitude accuracy. Initially intended to add local time coverage to the existing Swarm constellation, NanoMagSat mostly envisages ionospheric current systems and plasma density dynamics to cover the external field. It is, as a concept and in Phase B at the end of 2024, very likely now a frontrunner in high-precision modern but small satellite constellations to monitor the magnetic field of the Earth.

Figure 1-19: Sketch of NanoMagSat satellite (by ESA, Open Cosmos & NanoMagSat consortium).

1.2.3.2.5 MSS-1

MSS-1 (Figure 1-20) is a Chinese satellite (https://mss.must.edu.mo/) launched in May 2023, but proposed to be two not identical satellites (the second launch is scheduled earliest 2026), as a cooperation of Macao (Macao University of Science) a Special Administrative Region of China and the China Mainland. It is dedicated to observing the SAA with an inclination of only 41 deg., and with an altitude of about 450 x 500 km. It is equipped with vector and scalar sensors for magnetic field readings, scanning local time (14 hrs/month, full LT coverage in 26 days). It has a magnetic cleanliness program and no magnetorquers on board to minimise magnetic disturbance. [Information taken from a presentation on the 14th Swarm Data Quality workshop in Bucharest, session 7, second presentation, by Yi Jiang, Macau Scientific Satellite System Design and Verification, https://swarmdisc.org/dqw-archive/]. The mission data were recently mentioned in a paper on ocean-induced fields (Finlay et al., 2024).

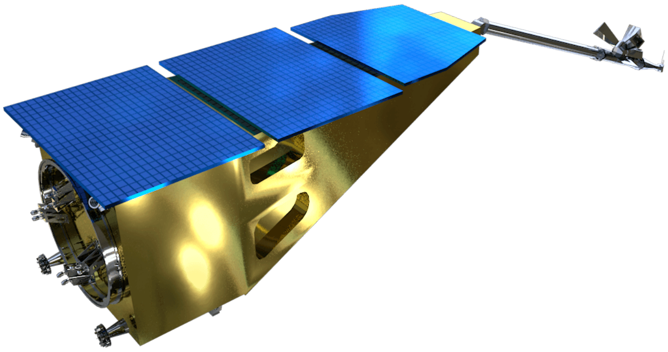

Figure 1-20: Sketch of MSS-1 satellite (https://mss.must.edu.mo/introduction.html).

1.2.3.2.6 CSES-1

CSES-1 (Figure 1-21) is a Chinese satellite (https://cses.web.roma2.infn.it), weighing 700 kg, which is considered a substantial size for a satellite. It has a box layout and was launched on February 2, 2018, into a sun-synchronous orbit at an altitude of 507 km. The satellite has a descending node time of 14:00 local time and operates in a polar orbit with an inclination of 97.4°. Its designed operational period is five years (Shen et al., 2018). The nominal scientific focus is the observation of earthquake effects in the ionosphere (seismo-ionospheric perturbations) and to measure geophysical fields in general like magnetic fields, electromagnetic waves (EM field waves in ULF, ELF, VLF and HF bands), plasma parameters, electron and ion temperatures and densities, TEC, energetic particle energy spectrum from 200 keV to 200 MeV; Pitch angle of energetic particles. For this ambitious purpose, CSES carries a full set of instruments: including a search-coil magnetometer (SCM), electric field detector (EFD), high precision magnetometer (HPM), GNSS occultation receiver (GOR), plasma analyser package (PAP), Langmuir probe (LAP), high energetic particle package (HEPP) and detector (HEPD), and tri-band beacon (TBB), among which HEPD is provided by Italian Space Agency. The magnetometers are mounted near the tip on relatively thin booms, the HPM is a combination of two (FGM) fluxgates and one coupled dark state magnetometer (CDSM, see(Pollinger et al., 2018b)). The data quality is affected (but flagged) by the magnetorquers and (consistently to own experiences as well) by terminator transitions, probably caused by boom deformation, with effects up to 100 nT (Yang et al., 2021) The magnetic data are recently were recently mentioned in a paper on ocean-induced fields (Finlay et al., 2024), too.

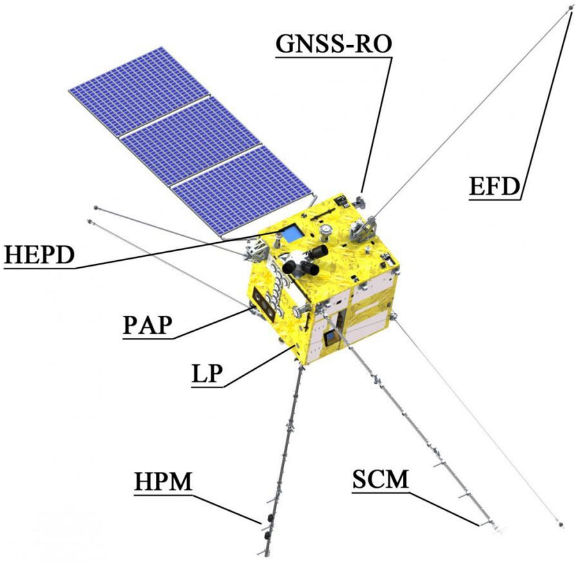

Figure 1-21: Sketch of CSES-1 satellite (https://cses.web.roma2.infn.it/?page_id=903).

1.2.3.2.7 GRACE/GRACE-FO

This mission series is focused on gravity, the initial mission GRACE (https://grace.jpl.nasa.gov/) covered 2002-2017, GRACE-FO (https://gracefo.jpl.nasa.gov) was launched in 2018 and GRACE-C (https://science.nasa.gov/mission/grace-c/) is scheduled for 2028. An overview sketch of the magnetometer location is given in Figure 1-22. GRACE was initially a NASA and DLR joint mission, an initial mission satellite manufactured by Astrium. It has a near-polar orbit with 89° inclination, 450 - 500 km (for GRACE) and 480 - 506 km (for GRACE-FO), the configuration is two satellites following each other in a controlled and precisely measured distance. This allows us to get a differential signal of environmental Earth's gravity. Subsequently this mission grants, by mission design, a stable attitude and reliable position. For calibration attempts of the platform magnetometer data see (Olsen, 2021; Styp-Rekowski et al., 2021).

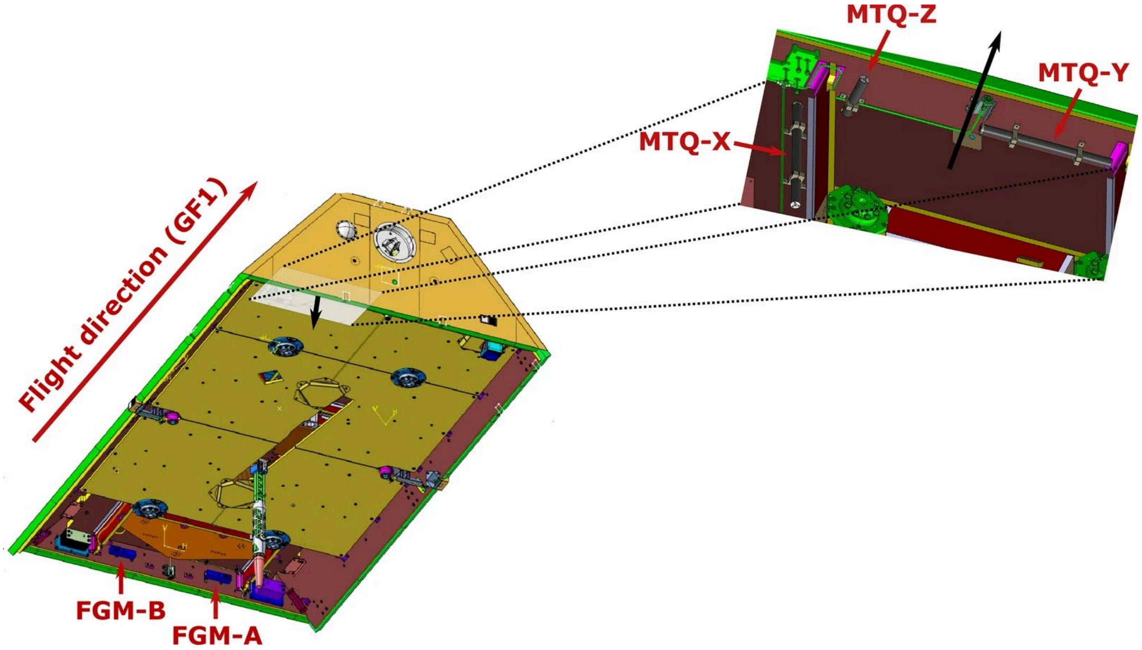

Figure 1-22: Sketch of GRACE-FO satellite (Figure 2 in (Stolle, Michaelis, et al., 2021b)).

1.2.3.2.8 GOCE

GOCE (https://earth.esa.int/eogateway/missions/goce) was part of the ESA Living Planet Program and spans 2009 - 2013, with a polar orbit of 97° inclination and an initial low altitude of 284 km. To maintain this altitude exposed to air-drag, an on-board xenon ion propulsion system was designed to compensate for the drag. This is another example of a gravity mission with platform magnetometers (MGM 1-3) used for AOCS, with attitude control by magnetorquers. An overview of satellite design and magnetometer location is given in Figure 1-23. By mission design the attitude information was reliable. More than one attempt to calibrate the magnetometers was performed, see (Michaelis et al., 2022; Olsen, 2021; Styp-Rekowski et al., 2022).

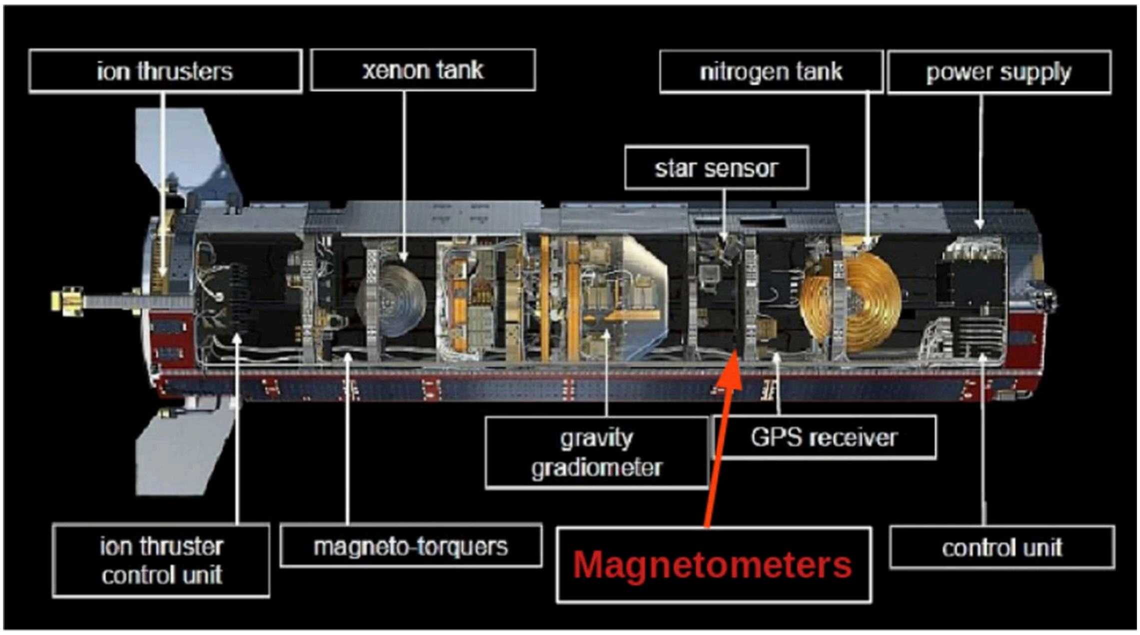

Figure 1-23: Sketch of GOCE instrument location Credits: ESA; Figure 3 in (Michaelis et al., 2022).

1.2.3.2.9 CryoSat-2

After the initial loss of CryoSat-1, the second version, CryoSat-2, was launched in April 2010 as part of the ESA Living Planet Program (https://earth.esa.int/eogateway/missions/cryosat). This mission focuses on monitoring changes in ice sheets and sea levels. The readings from its inflight-calibrated magnetometer can help address the data gap left by the CHAMP/Swarm missions. The satellite completes its scanning of LT in approximately eight months. For calibration attempts on CryoSat-2, refer to the work by (Olsen et al., 2020). For a study utilizing the calibrated CryoSat-2 platform's magnetometers to investigate ionospheric currents, refer to (Park, Stolle, et al., 2020). An overview sketch of the magnetometer's location is provided in Figure 1-24.

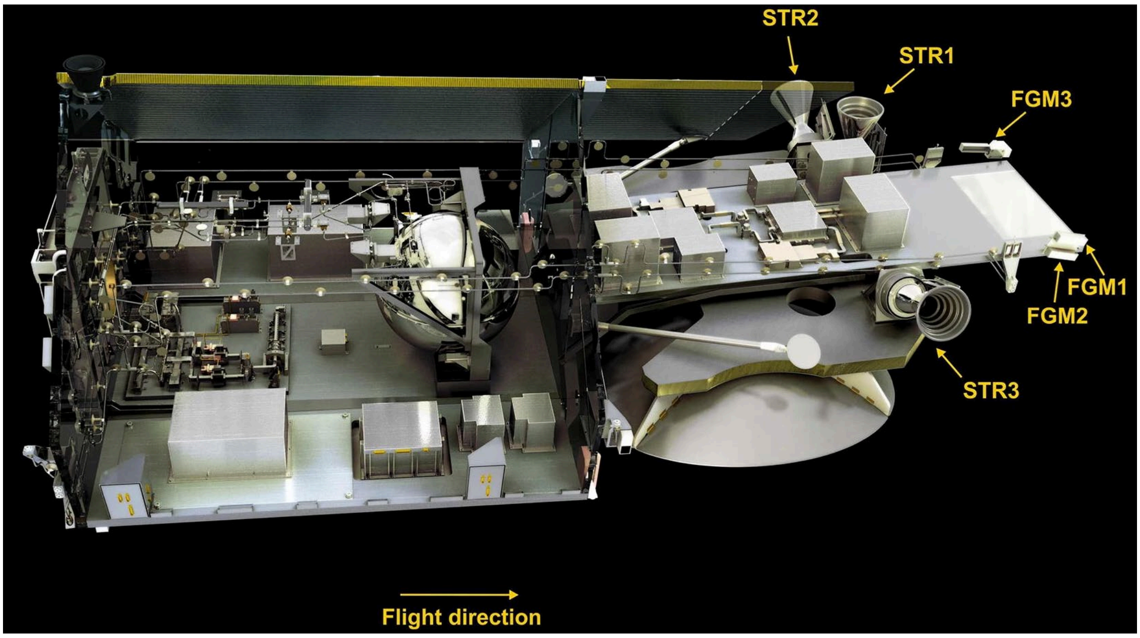

Figure 1-24: Sketch of CryoSat-2 satellite (Figure 1 in (Olsen et al., 2020)).

1.2.3.2.10 DMSP

DMSP (https://www.ncei.noaa.gov/products/satellite/defense-meteorological-satellite-program) is a series of U.S. military missions that began in the 1980s. Early satellites lacked magnetometer booms, but later versions, starting with DMSP F15 launched in 1999, were equipped with 5-meter booms to reduce magnetic interference from the spacecraft. Challenges with DMSP data include limited accessibility, competition with civilian weather applications, and issues arising from debris-related failures. Notably, DMSP F16 was utilized in efforts to bridge the data gap between the end of the CHAMP mission in 2010 and the commencement of the Swarm mission in 2013, as discussed by (Alken et al., 2020).

1.2.3.2.11 AMPERE (Iridium)

The Active Magnetosphere and Planetary Electrodynamics Response Experiment (AMPERE, https://ampere.jhuapl.edu) is a U.S. Earth observing system, operational since 2010, that utilizes a constellation of over 70 Iridium satellites (https://www.iridium.com/network/). These satellites orbit at approximately 780 km altitude in near-circular polar orbits, distributed globally across six orbital planes separated by 30°. AMPERE provides near-real-time magnetic field measurements, enabling 24-hour monitoring of Earth's response to solar wind and plasma ejections from the Sun. Its primary goals are to understand the global-scale electrodynamic interactions between the ionosphere and magnetosphere and to provide continuous, high-resolution observations of Birkeland currents (Anderson et al., 2000).

1.2.4 Lessons Learned

1.2.4.1 Attitude

Attitude information had turned always and finally out to be crucial for the scientific exploitation of core modelling and other internal fields. The crucial role of the star camera can be seen easily in the fact, that Swarm holds three-star cameras on its optical bench predecessor mission CHAMP only two, Oersted struggled with one. With attitude information available from more than one camera, the rotational sensitivity differences in the star camera coordinate system movement can be compensated. The angle in the boresight view direction (camera view) is far less sensitive than across the boresight axis. Unfortunately, subsequently, any transition between the modes of blinding modes is a sensitivity and attitude quality transition. The transition between normal operation and blindings of camera sensors may be difficult to handle, as there may be some instabilities of the calculated inter-boresight angles, the angles between the star camera view directions. These angles are needed to establish a proper and stable common reference system as a starting point for the transformation of vector information in Earth-Centered-Earth-Fixed or other physically useful magnetic coordinate systems. For mini-satellites without a full very rigid structure (see NanoMagSat and the deployable boom) attitude control needs obviously extra attention (Murilo et al., 2021).

1.2.4.2 Noise

It may be better to avoid momentum wheels (gyros) for magnetic missions: On the CASSIOPE/ePOP platform, there was an intense high-frequency signal, even changing on gyroscopes failings. Also, all mechanical movable parts are disadvantageous, see motor activation signal mentioned in (J. M. Léger et al., 2015) p. 3. All sources of satellite noise need attention, all possible locations need to be documented precisely (see Swarm dbSun error). Magnetorquers need extended effort at ground calibration and unfortunately, probably in-flight calibration manoeuvres too, as the ground values may be partly invalidated during launch. For the layout decisions keep in mind, that proper HK for in-flight categorizations of S/C disturbances (currents, temperatures) are very probably needed, the availability of HK should be an early mission design decision. In an ideal situation, with the availability of proper HK information, the machine learning attempt promised a simplified and more automated path for in-flight calibration and categorization (Styp-Rekowski et al., 2021, 2022). Heaters are another source of S/C inherent and time-dependent distortions, depending on satellite layout and the temperature prediction and management for sensor, boom or electronic boxes. Magnetic readings from modern sensors may not going to keep their high precision status after the processing without proper HK information. See for example heater systematic problems on Swarm ASM in burst mode, mentioned in (J. M. Léger et al., 2015) p. 4. Both, the usual launch delays and the obvious variability of the solar cycle will not allow to design a satellite for a dedicated quiet or busy period inside a cycle.

1.2.4.3 Considerations and hardware properties

The radiation sensitivity of sensors and electronics is a problem for the mission cycle of a box (see Swarm C final ASM failure). For CHAMP, the manufacturer of the vector magnetometer made a sufficient estimate on the sensitivity drift over time. It is important to know, if there is to be expected any decay of sensor sensitivity, other sensor-parameters or the electronic box (if any) during time, changing radiation level and launch stress. By what amount does the sensor reading need to be processed on board? Which information is exactly transmitted to the ground, and which part of the information is used and needed also by the on-board AOCS? The run-time inside the measurement cycle in the on-board processing needs to be known very well, depending on the sampling frequency and scientific target, usually even down to fractions of milliseconds. Spurious little time-shifts are usually a free parameter at least to check during an in-flight-calibration attempt. It is very beneficial if all instruments are properly synced by the GPS signal. Is there a long gap period after a cold restart or recovering from save-mode? There may be a trade-off between system life-estimation, degrading of the satellite system and instrument health and tasks scheduled. For example, on lithospheric and ionospheric studies just before atmospheric re-entry (see Swarm C ASM fail). At this probably late mission stage, the instrument and S/C health should be in proper health, and still good enough to cover the accuracy and stability requirements. The stray fields of sensors and heaters may limit the free layout of sensor locations, the stray field of the electronic box(es) may limit the number and time resolution of on-board magnetometers, the bit-widths of analogue to digital (AD) converters may limit the resolution of magnetic field recordings. For the required sensitivity level for ocean current and other internal field studies, there will be cross-talk – in particular but not exclusively on small boomless satellites. The Power sources (both, solar cells and batteries) and their transitional, temporal behaviour may limit the accuracy and usability of the magnetic field readings more than the specific properties of the dedicated sensors. Subsequently also orbit characteristics and S/C solar cell array layout have been taken into account.

1.2.5 Summary

Small and fancy satellites are usable to strengthen the impact of missions using dedicated high-precision vector and scalar magnetometer measurements with absolute accuracy. Even small field contributions by unexplained external fields are still weakening the geomagnetic field modelling gain. In-flight calibration may be simplified nowadays by Machine Learning (ML, if HK-data will be available by design), nevertheless, ground calibrations and system magnetic tests, flight manoeuvres and proper design decisions may be inevitable, still. Innovations only on the accuracy and stability of magnetic field sensors may not give the desired effect without taking care of the entire S/C system. However, efforts towards self-calibrating, high-precision vector and scalar magnetometer measurements with absolute accuracy are welcome for the next decade. Besides scientific (internal and external) geomagnetic modelling, the Space Weather near real-time monitoring to maintain and secure our critical infrastructure on the ground and in space may need additional minimizing the time delays for data availability in a valid and reliable product format. The Front-runner in the realisation of the named problems seems currently to be the incoming ASM-driven ESA Scout-program mission NanoMagSat, which is already tackling some known challenges of small satellite magnetic field measuring platforms, for example, miniaturising, an improved boom-construction and, assumably, the manoeuvrability problem (AOCS) of small and tiny mission layouts, in particular heading for constellation options and their benefits.

2 SENSOR REQUIREMENT DEFINITION

2.1 Introduction

Geophysical effects, current systems, and magnetic fields have been reviewed and documented in section 1.2. In this section, sensor requirement are defined. First, scenarios are developed based on each component of the state-of-the-art review. For each scenario, key parameters, including sensor accuracy, noise levels, and data distribution, are defined to ensure the scenario meets its specific requirements. Additionally, the scenarios account for potential variations in environmental conditions, measurement uncertainties, and operational constraints to enhance their applicability and robustness.

Based on the state-of-the-art of magnetic sensors used in space missions, instrument-level requirements are then defined in section 2.3, both for vector and scalar measurements. These requirements serve as a basis for selection of the most appropriate OPM technology in section 3. Finally, tentative instrument-level requirements are defined for the identified technology in section 2.3.2. These requirements will serve as a basis for the sensor high-level design realized in the next phase of the project. Final requirements will be updated based on the design realized in this last phase.

2.1.1 Definitions

In order to ensure a common understanding of the terminology used in this section, the following elements are defined:

Level-0 (L0): Raw measured data, directly representing the output of the instrument in its native data structure and in native units (e.g. clock cycle counts), after restoration of the chronological data sequence for the instrument operating in observation mode, at full (space/time) resolution, appended with all supplementary information to be used in subsequent processing (e.g. orbital data, time conversion, instrument status). L0 observation data are time-tagged. The precision and accuracy of the time-tag shall be such that the observations can be localized with a geometrical and temporal accuracy compatible with user requirements.

Level-1a (L1a): individual instrument physical products before corrections and calibration.

Level-1b (L1b): processed and corrected/calibrated data at instrument level.

Accuracy: the **absolute accuracy** is the root mean square (RMS) difference between the measurement and truth (or accepted reference value of the measured parameter) including both random and common systematic (bias) errors. Error distributions are to be understood as Gaussian and the values given refer to one standard deviation (1σ), unless otherwise stated. The accuracy can be expressed as follows: $accuracy=\sqrt{precision^2+bias^2}$. The unit of the accuracy is typically nT.

Resolution: the resolution is the smallest change a magnetometer can resolve for an individual measurement.

Sensitivity: the sensitivity is a sensor-specific value which characterizes the RMS noise for a given bandwidth. It is expression in units of rms magnetic field units per square root bandwidth. To achieve a given resolution, the sensitivity of a magnetometer must be at least equal over the measurement bandwidth and sampling rate.

Sensor drift: the sensor drift is the cumulated long-term error between two measurements made at over a time distance. The unit of the drift is typically nT/month.

Cadence (or sampling rate): The cadence is the frequency, normally constant, with which a given (L1b) observable is delivered in a data product. This may be linked, for instance, to the time needed to perform a measurement/acquisition cycle, or to the integration time of an instrument, and may be used synonymously with acquisition frequency. It can be distinct from a (faster) internal measurement sampling frequency where further integration within the cadence period may be necessary to obtain the final product or from a frequency range for alternating current (AC) observables, like electric or magnetic fields.

Bandwidth: The measurement bandwidth of an instrument is the difference between the upper and lower cutoff frequencies of the sensor. It is a sensor-specific value which, in principle, does not correspond to the sampling frequency of the sensor or the cadence of the measurement.

Dynamic range: the range of values is measurable by the system at L1b, or defining the expected range of values of a geophysical quantity that shall be observed. Often, the dynamic range of a measurement is limited at one end by saturation or physical limits of the measurement system, and at the other end by sources of random noise or uncertainty.

Signal range: the range of values of an isolated geophysical quantity without surrounding magnetic field.

Deadzone: the occurrence of signal degradation in specific magnetic field orientations with respect to the sensor is referred to as dead-zones

2.2 Observation scenarios

The internal geomagnetic field has the strongest requirements for accurately resolving magnetic field components (see Section 2.2.1.1). Field-aligned currents (FAC) at 50 Hz impose even stronger requirements in the context of current system observations (see Section 2.2.2.3). The strongest overall requirements are related to the secondary objective of detecting derived whistler waves (see Section 2.2.3.2).

2.2.1 Magnetic field

The geomagnetic field near Earth is shaped by internal and external sources, which include the internal field, external field, and lithospheric field. Together, these components shape the complex magnetic environment surrounding Earth, affecting navigation, communication, and space weather dynamics.

2.2.1.1 Internal field

The primary internal field originates from the Earth's core, resembles approximately a tilted dipole and gradually weakens with altitude. But the crucial field signal to isolate for the scientific exploitation is the time dependence, called Secular Variation, both on various length scales till about spherical harmonic degree 13 and also with response time scales down to weeks and months (see Figure 1-13). This is a fully-fledged challenge to the end-to-end stability, as of the sensor, the satellite system and any in-flight calibration schemes.

Table 2-1 : Overview of magnetic field requirements (internal field).

Type of Requirement	Value	Comments and Justification	Source
Magnetometer	Vector	See Backus effect (see section 1.2.2.1.2)	
Dynamic range	±65000 nT		(ESA Mission Experts Division, 2006)
Signal range	±65000 nT		(ESA Mission Experts Division, 2006)
Accuracy	< 0.8 nT		(ESA Mission Experts Division, 2006)
Cadence (Hz)	1/20		Rother et al., 2021
Sensor drift	< 0.025 nT/3 months		(ESA Mission Experts Division, 2006)

Table 2-2 : Overview of observational requirements (internal field).

Type of Requirement	Value	Comments and Justification	Source
Altitude coverage	~300-850 km (LEO)	This altitude range allows: • proximity to Earth's surface for better detection of the core magnetic field • reduced atmospheric drag to extend satellite operational lifespans	
Magnetic latitude coverage	Low-mid: <|55°| (SM) High: >|55°| (NEC)		(Rother et al., 2021)

Type of Requirement	Value	Comments and Justification	Source
Magnetic local time coverage	Low-mid: 23:00 to 05:00 High: all	It may depend on the details of the inversion method	(Rother et al., 2021)
Temporal coverage	3 months to decades		(ESA Mission Experts Division, 2006)
Temporal accuracy	< 10 ms	Temporal errors will be misinterpreted as vector attitude errors, minimum requirement for all payloads	Estimated at satellite altitude of 500km with a velocity of 8 km/s for the given attitude precision
Multi-point: number, location	TBD	Depends on satellite design (see WP230), sensor dead zones (see WP220), noise level reduction	
Boom configuration	TBD	Depends on satellite design (e.g., noise level, gradient)	
Attitude precision	< 2.5 arc sec		Estimated from accuracy @65000 nT (GFZ Technical Note in preparation)
Magnetic field vector product accuracy	0.8 nT	The overall accuracy requirement for the magnetic vector field product should be up to 0.8 nT, accounting for the cumulative impact of all instrument accuracies throughout the processing chain.	(ESA Mission Experts Division, 2006)
Magnetic field vector product drift	0.025 nT over 3 months	The overall drift requirement for the magnetic vector field product should be up to 0.025 nT over 3 months, considering the cumulative impact of all instrument drifts throughout the processing chain.	(ESA Mission Experts Division, 2006)

2.2.1.2 Lithospheric field

The lithospheric field, generated by magnetized crustal rocks, introduces smaller-scale anomalies. Assuming that crustal layers remain below the Curie temperature, this field is considered a largely static contribution. However, unless significantly enhanced, it remains a weak signal at satellite altitude, especially compared to low-degree main field contributions, already a weak signal at satellite altitude and on short and particularly disturbed periods in time easily masked by more than one external field contribution (see Figure 1-13).

Table 2-3 : Overview of magnetic field requirements (lithospheric field).

Type of Requirement	Value	Comments and Justification	Source
Magnetometer	Vector	See Backus effect (see section 1.2.2.1.2)	
Dynamic range	±65000 nT		(ESA Mission Experts Division, 2006)

Type of Requirement	Value	Comments and Justification	Source
Signal range	±25 nT		(ESA Mission Experts Division, 2006)
Accuracy	< 0.8 nT		(ESA Mission Experts Division, 2006)
Cadence (Hz)	1/5		Thébault et al., 2021
Sensor drift	< 0.025 nT/3 months		(ESA Mission Experts Division, 2006)

Table 2-4 : Overview of observational requirements (lithospheric field).

Type of Requirement	Value	Comments and Justification	Source
Altitude coverage	~250-500 km (LEO)	This altitude range allows: • proximity to Earth's surface for better detection of the core and crustal magnetic field reduced atmospheric drag to extend satellite operational lifespans	(Thébault et al., 2021)
Magnetic latitude coverage	Low-mid: <|60°| High: >|50°|		(Thébault et al., 2021)
Magnetic local time coverage	Low-mid: <|60°| (21:00 to 05:00) High: >|50°| (Sun at least 10° below horizon)		(Thébault et al., 2021)
Temporal coverage	Decades to static		(ESA Mission Experts Division, 2006)
Temporal accuracy	< 10 ms	Temporal errors will be misinterpreted as vector attitude errors, minimum requirement for all payloads	Estimated at satellite altitude of 500km with a velocity of 8 km/s for the given attitude precision
Multi-point: number, location	TBD	Depends on satellite design (see WP230), sensor dead zones (see WP220), noise level reduction	
Boom configuration	TBD	Depends on satellite design (e.g., noise level, gradient)	
Attitude precision	< 2.5 arc sec		Estimated from accuracy @65000 nT (GFZ Technical Note in preparation)
Magnetic field vector product accuracy	0.8 nT	The overall accuracy requirement for the magnetic vector field product should be up to 0.8 nT, accounting for the cumulative impact of all instrument accuracies throughout the processing chain.	(ESA Mission Experts Division, 2006)

Type of Requirement	Value	Comments and Justification	Source
Magnetic field vector product drift	0.025 nT over 3 months	The overall drift requirement for the magnetic vector field product should be up to 0.025 nT over 3 months, considering the cumulative impact of all instrument drifts throughout the processing chain.	(ESA Mission Experts Division, 2006)

2.2.1.3 External field

The external field components, generated by various current systems above the Earth's surface (beyond the crust and oceans), exhibit variations on shorter timescales. These fluctuations are primarily driven by interactions with the solar wind and encompass periodic and aperiodic contributions, as well as spatial variations ranging from large to small scales within the magnetosphere and ionosphere. Notably, this includes dynamic phenomena such as geomagnetic storms and substorms, which can persist for hours to several days, significantly influencing the Earth's magnetic environment.

Table 2-5 : Overview of magnetic field requirements (external field).

Type of Requirement	Value	Comments and Justification	Source
Magnetometer	Vector	See Backus effect (see section 1.2.2.1.2)	
Dynamic range	±65000 nT		(ESA Mission Experts Division, 2006)
Signal range	±1000 nT		(ESA Mission Experts Division, 2006)
Accuracy	< 0.8 nT		(ESA Mission Experts Division, 2006)
Cadence (Hz)	10 to 250	TBD	
Sensor drift	< 0.025 nT/3 months		(ESA Mission Experts Division, 2006)

Table 2-6 : Overview of observational requirements (external field).

Type of Requirement	Value	Comments and Justification	Source
Altitude coverage	TBD	Depends on the scenarios, see section 2.2.2)	
Magnetic latitude coverage	TBD	Depends on the scenarios, see section 2.2.2)	
Magnetic local time coverage	TBD	Depends on the scenarios, see section 2.2.2)	
Temporal coverage	0.1 sec to 11 years		(ESA Mission Experts Division, 2006)

Type of Requirement	Value	Comments and Justification	Source
Temporal accuracy	< 10 ms	Temporal errors will be misinterpreted as vector attitude errors, minimum requirement for all payloads	Estimated at satellite altitude of 500km with a velocity of 8 km/s for the given attitude precision
Multi-point: number, location	TBD	Depends on satellite design (see WP230), sensor dead zones (see WP220), noise level reduction	
Boom configuration	TBD	Depends on satellite design (e.g., noise level, gradient)	
Attitude precision		< 2.5 arc sec	Estimated from accuracy @65000 nT (GFZ Technical Note in preparation)
Magnetic field vector product accuracy	0.8 nT	The overall accuracy requirement for the magnetic vector field product should be up to 0.8 nT, accounting for the cumulative impact of all instrument accuracies throughout the processing chain.	(ESA Mission Experts Division, 2006)
Magnetic field vector product drift	0.025 nT over 3 months	The overall drift requirement for the magnetic vector field product should be up to 0.025 nT over 3 months, considering the cumulative impact of all instrument drifts throughout the processing chain.	(ESA Mission Experts Division, 2006)

2.2.2 Current systems

The near-Earth environment hosts various current systems, both internal and external, that influence the geomagnetic field: mantle-induced currents, magnetospheric currents, field-aligned currents (FACs), inter-hemispheric FACs, solar quiet currents, equatorial electrojet, polar electrojet, ocean tides.

2.2.2.1 Mantle-induced currents (internal, core)

These currents are produced by fluctuations in the Earth's core magnetic field, which induce electrical currents within the mantle through electromagnetic induction.

Table 2-7 : Overview of magnetic field requirements (external field).

Type of Requirement	Value	Comments and Justification	Source
General remark		Core, lithospheric and external magnetic field model components must be extracted. The quality of the analysis depends on the quality of the available model. Specifications for internal, lithospheric and external field have to be fulfilled as well.	(Finlay et al., 2024)
Magnetometer Dynamic range			

Type of Requirement	Value	Comments and Justification	Source
Signal range	±10 nT	The internal field requirements are more restrictive (see section 2.2.1.1)	(Finlay et al., 2024)
Accuracy			
Cadence (Hz)			
Sensor drift			

Table 2-8 : Overview of observational requirements (external field).

Type of Requirement	Value	Comments and Justification	Source
General remark			
Altitude coverage			
Magnetic latitude coverage			
Magnetic local time coverage			
Temporal coverage			
Temporal accuracy			
Multi-point: number, location			
Boom configuration			
Attitude precision			
Magnetic field vector product accuracy			
Magnetic field vector product drift			

2.2.2.2 Magnetospheric currents (external, equator)

These are large-scale currents within the magnetosphere, including the ring current (RC), which encircles the Earth near the equator and plays a significant role in geomagnetic storms.

Table 2-9 : Overview of magnetic field requirements (external field).

Type of Requirement	Value	Comments and Justification	Source
General remark			
Magnetometer			
Dynamic range			
Signal range	±20 nT	The internal field requirements are more restrictive (see section 2.2.1.1)	(Finlay et al., 2024)
Accuracy			
Cadence (Hz)			
Sensor drift			

Table 2-10 : Overview of observational requirements (external field).

Type of Requirement	Value	Comments and Justification	Source
General remark			
Altitude coverage			
Magnetic latitude coverage			
Magnetic local time coverage			
Temporal coverage			
Temporal accuracy			
Multi-point: number, location			
Boom configuration			
Attitude precision			
Magnetic field vector product accuracy			
Magnetic field vector product drift			

2.2.2.3 High-latitude field-aligned currents (external, polar)

Auroral field-aligned currents, known as Birkeland currents, connect the Earth's magnetosphere to the polar ionosphere along magnetic field lines. These currents transfer energy from the magnetosphere into the ionosphere, where they enhance auroral activity. During geomagnetic storms, the intensity of these currents increases, leading to more vivid auroras and influencing space weather conditions.

Table 2-11 : Overview of magnetic field requirements (external field).

Type of Requirement	Value	Comments and Justification	Source
General remark		Core, lithospheric and external magnetic field model components must be extracted. The quality of the analysis depends on the quality of the available model. Specifications for internal, lithospheric and external field have to be fulfilled as well.	
Magnetometer	Vector	FAC are derived from eastward pointing component in mean field aligned coordinate frame.	(Rother et al., 2007)
Dynamic range			
Signal range	±1000 nT		(Rother et al., 2007)
Accuracy	0.1 nT	A field change of 0.1 nT in 20ms converts to a very small FAC density of 0.8 µA/m^2	(Rother et al., 2007)
Cadence (Hz)	50	Small-scale FAC, wave length range 5km to below 1km	(Rother et al., 2007)
Sensor drift			

Table 2-12 : Overview of observational requirements (external field).

Type of Requirement	Value	Comments and Justification	Source
General remark			
Altitude coverage			
Magnetic latitude coverage			
Magnetic local time coverage			
Temporal coverage			
Temporal accuracy			
Multi-point: number, location			
Boom configuration			
Attitude precision		Arc second precision.	(Rother et al., 2007)
Magnetic field vector product accuracy			
Magnetic field vector product drift			

2.2.2.4 Inter-hemispheric FACs (external, equator)

Inter-hemispheric field-aligned currents (IHFACs) are equatorial currents that connect the northern and southern hemispheres through the Earth's magnetosphere. These currents are primarily driven by ionospheric and magnetospheric processes, such as variations in solar wind and the Earth's magnetic field.

Table 2-13 : Overview of magnetic field requirements (external field).

Type of Requirement	Value	Comments and Justification	Source
General remark		Core, lithospheric and external magnetic field model components must be extracted. The quality of the analysis depends on the quality of the available model. Specifications for internal, lithospheric and external field have to be fulfilled as well.	
Magnetometer			
Dynamic range			
Signal range	±100 nT	The internal field requirements are more restrictive (see section 2.2.1.1)	(Finlay et al., 2024)
Accuracy			
Cadence (Hz)			
Sensor drift			

Table 2-14 : Overview of observational requirements (external field).

Type of Requirement	Value	Comments and Justification	Source
General remark			
Altitude coverage			
Magnetic latitude coverage			
Magnetic local time coverage			
Temporal coverage			
Temporal accuracy			
Multi-point: number, location			
Boom configuration			
Attitude precision			
Magnetic field vector product accuracy			
Magnetic field vector product drift			

2.2.2.5 Solar quiet currents (external, low latitudes)

Solar quiet (Sq) currents, driven by solar heating, flow in the ionosphere's E-region, mainly near the equator. Sun-induced heating increases conductivity, generating these currents that modulate the geomagnetic field. They peak during the day, following a regular diurnal pattern, and play a significant role in global ionospheric and magnetospheric dynamics.

Table 2-15 : Overview of magnetic field requirements (external field).

Type of Requirement	Value	Comments and Justification	Source
General remark		Should be co-estimated with core, lithospheric and external magnetic field model components. Specifications for internal, lithospheric and external field have to be fulfilled as well.	(Finlay et al., 2024)
Magnetometer			
Dynamic range			
Signal range	±20 nT	The internal field requirements are more restrictive (see section 2.2.1.1)	(Finlay et al., 2024)
Accuracy			
Cadence (Hz)			
Sensor drift			

Table 2-16 : Overview of observational requirements (external field).

Type of Requirement	Value	Comments and Justification	Source
General remark			

Type of Requirement	Value	Comments and Justification	Source
Altitude coverage			
Magnetic latitude coverage			
Magnetic local time coverage			
Temporal coverage			
Temporal accuracy			
Multi-point: number, location			
Boom configuration			
Attitude precision			
Magnetic field vector product accuracy			
Magnetic field vector product drift			

2.2.2.6 Equatorial electrojet (external, equator)

The Equatorial Electrojet (EEJ) is a powerful eastward electric current that flows close to the magnetic equator in the ionosphere, mainly within the E-region. This current is generated by increased ionospheric conductivity and electric fields.

Table 2-17 : Overview of magnetic field requirements (external field).

Type of Requirement	Value	Comments and Justification	Source
General remark		Core, lithospheric and external magnetic field model components must be extracted. The quality of the analysis depends on the quality of the available model. Specifications for internal, lithospheric and external field have to be fulfilled as well.	
Magnetometer	Vector + Scalar		(Lühr et al., 2011)
Dynamic range			
Signal range			(Lühr et al., 2004)
Accuracy	0.1 nT		
Cadence (Hz)	1		(Lühr et al., 2004)
Sensor drift			

Table 2-18 : Overview of observational requirements (external field).

Type of Requirement	Value	Comments and Justification	Source
General remark			
Altitude coverage			
Magnetic latitude coverage			

Type of Requirement	Value	Comments and Justification	Source
Magnetic local time coverage			
Temporal coverage			
Temporal accuracy			
Multi-point: number, location			
Boom configuration			
Attitude precision			
Magnetic field vector product accuracy			
Magnetic field vector product drift			

2.2.2.7 Polar electrojet (external, polar)

The Polar Electrojet (PEJ) is a strong electric current that flows in the polar regions of the ionosphere, generally aligned with the Earth's magnetic field. It is associated with geomagnetic activity and auroras and often becomes stronger during solar storms.

Table 2-19 : Overview of magnetic field requirements (external field).

Type of Requirement	Value	Comments and Justification	Source
General remark		Core, lithospheric and external magnetic field model components must be extracted. The quality of the analysis depends on the quality of the available model. Specifications for internal, lithospheric and external field have to be fulfilled as well.	
Magnetometer			
Dynamic range			
Signal range	±50 nT	The internal field requirements are more restrictive (see section 2.2.1.1)	(Finlay et al., 2024)
Accuracy			
Cadence (Hz)			
Sensor drift			

Table 2-20 : Overview of observational requirements (external field).

Type of Requirement	Value	Comments and Justification	Source
General remark			
Altitude coverage			
Magnetic latitude coverage			
Magnetic local time coverage			

Type of Requirement	Value	Comments and Justification	Source
Temporal coverage			
Temporal accuracy			
Multi-point: number, location			
Boom configuration			
Attitude precision			
Magnetic field vector product accuracy			
Magnetic field vector product drift			

2.2.2.8 Ocean tides and currents (internal)

Conductive seawater movement, generated by gravitational forces from the Moon and the Sun, produces electrical currents that interact with the geomagnetic field, resulting in small but detectable magnetic variations.

Table 2-21 : Overview of magnetic field requirements (external field).

Type of Requirement	Value	Comments and Justification	Source
General remark		Should be co-estimated with core, lithospheric and external magnetic field model components. Specifications for internal, lithospheric and external field have to be fulfilled as well.	
Magnetometer	Scalar + Vector		(Grayver et al., 2024)
Dynamic range			
Signal range	±1 nT		(Finlay et al., 2024)
Accuracy			
Cadence (Hz)	1/15		(Grayver et al., 2024)
Sensor drift			

Table 2-22 : Overview of observational requirements (external field).

Type of Requirement	Value	Comments and Justification	Source
General remark			
Altitude coverage			
Magnetic latitude coverage	Vector: lat < |55|, Scalar: all		(Grayver et al., 2024)
Magnetic local time coverage			
Temporal coverage			

Type of Requirement	Value	Comments and Justification	Source
Temporal accuracy			
Multi-point: number, location			
Boom configuration			
Attitude precision			
Magnetic field vector product accuracy			
Magnetic field vector product drift			

2.2.3 Waves

A section for wave detection, which may connect with distant, magnetospheric, currents, but show specific features. This section is based on contributions seen in different conferences and personal communications and seems that there are a quite a few publications or none(!).

2.2.3.1 PC waves

in particular PC-1 (about 1 Hz, < 10 Hz, ULF) can easily measure by LEOs

Table 2-23 : Overview of magnetic field requirements (external field).

Type of Requirement	Value	Comments and Justification	Source
General remark			
Magnetometer			
Dynamic range			
Signal range	< 1 nT		
Accuracy			
Cadence (Hz)			
Sensor drift			

Table 2-24 : Overview of observational requirements (external field).

Type of Requirement	Value	Comments and Justification	Source
General remark			
Altitude coverage			
Magnetic latitude coverage			
Magnetic local time coverage			
Temporal coverage			
Temporal accuracy			
Multi-point: number, location			

Type of Requirement	Value	Comments and Justification	Source
Boom configuration			
Attitude precision			
Magnetic field vector product accuracy			
Magnetic field vector product drift			

2.2.3.2 Whistler

Whistler (probably only the low frequent versions) are detected by Swarm ASM in burst modes (<250 Hz) but it is hard to find any published paper (some conference presentations only, e.g., see Swarm DQWs).

It is assumed that whistler are created below the LEO satellite orbits, related to magnetospheric activity and, also, the VLF and ELF versions to Lightening events in the atmosphere. They have been observed since the beginning of 20th century from the ground magnetic observatories. Since the high-precision satellite magnetometry, the statistical studies even over the unpopulated oceans is possible.

Table 2-25 : Overview of magnetic field requirements (external field).

Type of Requirement	Value	Comments and Justification	Source
General remark			
Magnetometer			
Dynamic range			
Signal range	50 -- > 500 pT in radiation belt		(Tyler et al., 2003 and Bernhardt et al., 2022)
Accuracy			
Cadence (Hz)	250 (Swarm)	800 Hz for NanoMagSat That is still only the lower edge of the frequency band of Whistlers (ELF range from DC to 1000 Hz).	(Coisson et al., 2022)
Sensor drift			

Table 2-26 : Overview of observational requirements (external field).

Type of Requirement	Value	Comments and Justification	Source
General remark			
Altitude coverage	LEO and above		
Magnetic latitude coverage			
Magnetic local time coverage	unspecified		
Temporal coverage			

Type of Requirement	Value	Comments and Justification	Source
Temporal accuracy	Not critical		
Multi-point: number, location			
Boom configuration			
Attitude precision			
Magnetic field vector product accuracy			
Magnetic field vector product drift			

2.2.3.3 Alfven waves

Alfven waves, a frequent phenomenon in applied physics and astrophysics, are here associated with (assumed) high-frequency FACs and the concept of an IAR (ionospheric Alfvén resonator. This was discussed already at the beginning of this millennium for a complete picture it is challenging but necessary to discriminate between spatial static and simultaneous temporal wave structures.

Table 2-27 : Overview of magnetic field requirements (external field).

Type of Requirement	Value	Comments and Justification	Source
General remark			
Magnetometer			
Dynamic range			
Signal range	Till Approx 100 nT		
Accuracy	low		
Cadence (Hz)	> 50 Hz		
Sensor drift	Neglib.		

Table 2-28 : Overview of observational requirements (external field).

Type of Requirement	Value	Comments and Justification	Source
General remark			
Altitude coverage			
Magnetic latitude coverage			
Magnetic local time coverage			
Temporal coverage	All LT		Rother 2007
Temporal accuracy	<1 ms		
Multi-point: number, location			
Boom configuration			
Attitude precision	Few ‘’		

Type of Requirement	Value	Comments and Justification	Source
Magnetic field vector product accuracy	< 1 nT		
Magnetic field vector product drift	Not critical		

2.2.4 Magnetometer configuration and data coverage

2.2.4.1 Magnetometer configuration

This section covers the setup and specifications of the satellite's magnetometers, including the number of instruments, their arrangement (either on the satellite's boom or integrated within the satellite body), and their measurement capabilities. It also describes the technical features that enhance the sensitivity and accuracy of the magnetometers in detecting geomagnetic variations.

2.2.4.2 Data coverage

This section discusses the spatial distribution, temporal cadence, and magnetic local time (MLT) coverage of the satellite's data collection. It includes details on how the satellite's inclination, sun-synchronization, and overall orbit characteristics influence data coverage, ensuring comprehensive observations of the geomagnetic field across different regions and time periods.

2.3 Instrument-level requirements

In this section, the instrument-level requirements for a space OPM are derived. The following aspects were considered:

- Functional requirements
- Performance requirements
- SWaP (Size, weight and power consumption), both at sensor and at instrument level
- Environmental aspects: Lifetime, operating interface temperature range, radiation (micro-) vibration hardness

First a preliminary identification of the most relevant OPM technologies is presented. This will serve as a basis for the next task of the project. Then instrument-level requirements are derived which will be refined based on the output of the high-level design done in the next task of the project.

2.3.1 Identification of relevant OPM technologies

Due to stringent vector accuracy requirements in Earth observation missions, the literature review identifies coil-based scalar measurement systems as the most promising platform for vector optically pumped magnetometers (OPMs). While other emerging techniques have been demonstrated (see Section 1.1.3), they remain in early stages of development and require significant additional development to achieve accuracy standards suitable for near-Earth orbit applications. In contrast, coil calibration algorithms utilizing scalar measurements are well-established, achieving vector accuracies better than 1 nT (Gravrand et al., 2001), and have successfully supported multiple space missions (Olsen et al., 2003). In addition, recent innovations in miniaturizing 3D planar coil systems present significant opportunities for reducing size, weight, and power (SWaP) (Tayler et al., 2022), further enhancing the suitability of coil-based vector OPM technologies for space missions.

Below, three promising coil-based vector OPM techniques identified in the literature review are detailed along with their strengths and limitations:

2.3.1.1 Fast Rotating Field Vector Magnetometer

Description:

This technique, described in (T. Wang et al., 2023), involves applying a fast-rotating (~1 kHz) magnetic field to a pulsed scalar OPM, enabling simultaneous measurements of total magnetic field magnitude and two polar angles relative to the rotation plane. Readout is based on free induction decay (FID).

Pros:

- High angular resolution: 6 nrad/√Hz at 50 μT ambient field
- Vector sensitivity down to 280 fT/√Hz; scalar sensitivity (without modulation) as low as 28 fT/√Hz
- Rapid measurement capability (bandwidth ~30 Hz)
- Potential for enhanced sensitivity using multipass cells (down to a few fT/√Hz)
- Increased stability through vector axes defined by magnetic field rotation plane, avoiding mechanical coil orthogonality requirements

Cons:

- Presence of dead zones
- Vector accuracy depends significantly on atomic response modeling
- Limited validation (currently supported by a single research publication)

2.3.1.2 Low-Frequency Coil Modulation (Swarm Mission Approach)

Description: The technology described in (Andryushkov et al., 2022; Gravrand et al., 2001; J. M. Léger et al., 2015), utilizes low-frequency (~10 Hz) coil modulation fields independently applied along three orthogonal axes. The scalar magnetometer detects amplitude changes induced by these modulations, enabling the reconstruction of ambient field orientation. Optimal performance typically requires ^{4}He scalar magnetometers due to lower systematic errors compared to alkali-based magnetometers.

Pros:

- Proven vector accuracy: ~7 μrad (~0.35 nT at 50 μT ambient field), as demonstrated by Swarm mission
- High scalar accuracy (better than 100 pT)
- Established and robust technique with successful space heritage
- Potentially deadzone-free with rotating linear polarization in ^{4}He magnetometers

Cons:

- Limited vector sensitivity (~1 nT/√Hz at 25 μT), significantly lower than scalar sensitivity (~1 pT/√Hz)
- Constrained vector measurement bandwidth (few Hz) due to low modulation frequencies
- Necessity of 4He scalar magnetometers, as alkali magnetometers introduce systematic errors >3 nT

2.3.1.3 Zero-Field Nulling

Description: This technique (Bertrand et al., 2021; Seltzer & Romalis, 2004) involves using coil systems to precisely control and minimize the magnetic field environment around the OPM cell. The technique is flexible in magnetic field strength (low-field conditions at the cell: ~1–5 µT) and orientation, maximizing sensitivity independently of atomic species.

Pros:

- High operational dynamic range (±70 µT demonstrated under challenging coil compensation scenarios)
- Compatible with multiple atomic species, avoiding alkali limitations at high fields (e.g., nonlinear Zeeman splitting)
- Demonstrated high vector sensitivity: 130 fT/√Hz (4He) (Bertrand et al., 2021); 1 pT/√Hz (K) (Seltzer & Romalis, 2004)
- High vector accuracy (~0.7 nT), primarily limited by characterization methodology
- Compact size and low SWaP (5 cm diameter system plus electronics)
- Deadzone-free operation
- Reasonable bandwidth (~1 kHz)

Cons:

- Performance constrained by electronics and feedback mechanisms
- Vector calibration based on methodologies from the Oersted mission, limited by assumptions of homogeneous local magnetic and thermal fields (though improvement is possible)
- High demands on DAC performance (dynamic range and noise)

2.3.1.4 Discussion

The zero-field nulling approach is particularly promising for near-Earth orbit applications due to its demonstrated combination of high accuracy, sensitivity, dynamic range, and deadzone-free operation. Additionally, its compatibility with both ^{4}He and alkali vapor cells provides flexibility in design and implementation. Alkali atoms offer potential advantages through established MEMS vapor cell technology cell (Raghavan et al., 2024a), although typically requiring separate pump and probe beams for high-accuracy implementations. MEMS-based ^{4}He cells remain challenging Rutkowski et al., 2014) and underdeveloped.

Commercial alkali OPM sensors, such as those from Qspin and Fieldline, demonstrate promising scalar and vector sensitivities with low SWaP. However, their accuracy currently falls short of near-orbit mission requirements. Further investigation into calibration methods and combining commercial alkali OPMs with zero-field nulling may yield significant accuracy improvements, warranting additional research.

2.3.2 Derivation of instrument-level requirements

In this section, requirements are derived for one instrument, following our proposal (see section 3) for a self-calibrating vector OPM. We suppose that, as for most magnetic field observation missions including Swarm (see 2.3.1.2), the scalar magnetometer serves for continuous calibration of the vector magnetometer making it obsolete in our design.

The requirement table is derived from different sources:

- The performance requirements for the observation scenarios considered in section 2.2
- The state-of-the-art specifications of magnetic sensors used in previous missions
- Commercial products based on OPM technology
- The typical requirements of a space product used in the relevant orbit for a normal-size and for a small satellite
- European Cooperation for Space Standardization standards (ECSS)

In the high-level presentation of our sensor concept, compliance to these requirements will be derived and discussed.

2.3.3 Magnetometer requirements

Table 2-29: Magnetometer requirements.

Ref.	Parameter	Value	Unit	Remark
Functional				
RQS10	1 highly accurate vector magnetic field strength signal			
RQS20	Functional modes ON and OFF			
RQS30	No maintenance in OFF mode			
RQS40	"health status" and telemetries to debug and assess lifetime behaviour			
RQS50	Data rate / Cadence	250	Hz	Needed for external fields detection
RQS60	Warm-up time	< 3600	s	
Performance				
RQS110	Dynamic range	65	μT	
RQS120	Bandwidth	400	Hz	Bandwidth is half burst mode data rate (RQS60)
RQS130	Resolution	10	pT/sqrt(Hz)	Value calculated from RQS120
RQS140	Accuracy	< 0.8	nT	Over the full instrument lifetime (RQS370)
RQS150	Drift	3	pT/month	TBC: value calculated from RQS140 and RQS370
RQS160	Deadzone	Deadzone free		
Size, Weight and Power consumption				
RQS210	Mass	< 200	gr	Design goal: < 100 g
RQS220	Volume	< 200	cm^3	Design goal: < 100 cm^3
RQS230	Voltage supply	TBD	V	TBD in function of satellite /mission
RQS240	Sensor power consumption during warm-up	< 3	W	Under vacuum, over the full range of temperature (RQ310), design goal: <2W
RQS250	Power consumption	< 2	W	Under vacuum, over the full range of temperature (RQ310)
Environment				
RQS310	Operating temperature	-15 to 55	°C	
RQS320	Storage & OFF mode temperature	-55 to 85	°C	
RQS330	Random vibration	TBD	grms	Mission / satellite dependent, TBD according to [AD 1]

RQS340	Micro-vibration	TBD	mg	Mission / satellite dependent, TBD according to [AD 1]
RQS350	Shock	TBD	g	Mission / satellite dependent, TBD according to [AD 1]
RQS360	Radiation	TBD	Krad	Orbit and inclination dependent, TBD according to [AD 2]
RQS370	Lifetime	20	years	
RQS380	Operates both in vacuum and ambient conditions			

2.3.3.1 Functional requirements

The functional requirements describe what the instrument shall perform.

Data rate:
The date rate is based on the observation scenarios reported above with the highest needed rate of 250 Hz needed for the measurement for external fields. In our case, data rate is limited by the recalibration sequence leading to deadtime.

Burst mode data rate:
The burst mode data rate is not based on the observation scenarios reported above but on the requirement for the HFM of NanoMagSat (J.-M. Léger et al., 2022b).

Note that it was estimated LEO orbit maximal rate for magnetic fields of the order to 50 nT/s. The minimal burst mode data rate is hence derived by this value and the chosen accuracy. For 0.8 nT accuracy the burst mode data rate should be at least of the order to 62.5 Hz.

Warm-up time:
The warm-up time is the time required by the instrument to provide its data. It corresponds to the time required by the atomic vapor cell to reach its operational temperature.

2.3.3.2 Performance requirements

Dynamic range:
The dynamic range requirement is fixed by the absolute magnitude of the magnetic field to be measured. Typical requirements of space products are of 65µT (see section 2.2 and (J.-M. Léger et al., 2022a; J. é M. G. Merayo et al., 2008)).

Bandwidth:
OPMs are capable of high bandwidth measurement (see 1.1.2.2). The bandwidth requirement is hence estimated as half the burst mode cadence.

Resolution:
The required resolution (or sensitivity) depends on the bandwidth and the required accuracy for a single measurement. This requirement will be determined from the chosen bandwidth and accuracy.

Vector accuracy:
An accuracy requirement of 0.8 nT is given for the different observation scenarios (see section 2.2) for the L1b vector product. The vector accuracy is guaranteed by a continuous scalar calibration with the help of the scalar magnetometer. This requirement accounts for the cumulative impact of all instrument accuracies throughout the processing chain, *i.e.* the contributions from the vector

instrument, the scalar instrument used for calibration, the attitude determination, as well as any remaining calibration errors, position and attitude uncertainties, and integrated noise.
An equivalent zero stability is needed to reach the a given vector stability with the help of a absolute scalar reference.

Vector drift:
An overall L1b vector stability requirement of 0.025 nT over 3 months is given for the different observation scenarios (see section 2.2). However, in order to guarantee a total vector accuracy of 0.8 nT (RQS140) over the entire lifetime of the sensor (RQS310), a maximum drift 0.01nT/month is given as requirement. The total vector accuracy is guaranteed by a continuous scalar calibration with the help of the scalar magnetometer. However, an equivalent zero stability is still needed to reach the same vector stability. This drift value thus also serves as a basis for this requirement.

2.3.3.3 SWaP requirements

A need for low-SWaP instruments to embark on small-size plateforms was identified in section 1.2. The SWaP requirements are thus based on the current state-of-the-art of commercial OPMs based on miniature atomic vapor cells (MEMS cells). In particular, the QZFM Gen-4 zero-field OPM from QuSpin is used as reference.

Figure 2-1: QuSpin QZFM Gen-3 OPM

The following specifications are reported by QuSpin[1]:

- Sensor size (without coils): 5 cm^3
- Instrument size (including electronic): 562 cm^3 (0.6 l)
- Resolution: <23fT/sqrt(Hz) (3-axis)
- Bandwidth: 3-100 Hz
- Power consumption: 5W total (0.7W sensor head)
- Selling price (07/03/2025) <10’000$/pce

Mass:
Considering a spatial product to be embarked in a small satellite, a value of < 100 g is given, which corresponds to the requirements of NanoMagSat (J.-M. Léger et al., 2022). Based on the commercial state-of-the-art above, a design goal of < 50 g is fixed, which includes the coil system. Given that our proposal does not contain a separate scalar OPM, we double these values in our requirements.

Volume:
Considering a spatial product to be embarked in a small satellite, a value of < 100 cm^3 is given, which corresponds to the requirements of NanoMagSat (J.-M. Léger et al., 2022). Based on the

---

[1] https://quspin.com/products-qzfm/

commercial state-of-the-art above, a design goal of < 50 cm^3 g is fixed. In order to reach such a low volume, miniature coils can be used to minimize the footprint of the 3-axis coil system(Tayler et al., 2022b). Given that our proposal does not contain a separate scalar OPM, we double these values in our requirements.

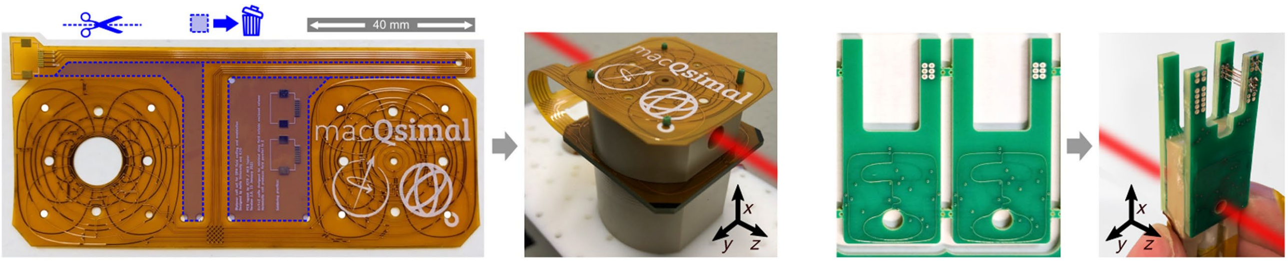

Figure 2-2: Miniature biplanar coils for OPMs (Tayler et al., 2022b)

Power consumption:
Based on the SWARM vector field magnetometer specification, a power consumption of < 1 W in steady-state and <1.5 W during warm-up under vacuum is fixed. This is compatible with the commercial sensor head power consumption reported above of 0.7W under atmosphere. The physics package power consumption is typically dominated by the heating of the atomic vapor cell which is lower in vacuum. Values of < 250mW at 25°C ambient temperature have been demonstrated (Haesler et al., 2017). Refinement of the electronic design is nevertheless needed to confirm this value. Given that our proposal does not contain a separate scalar OPM, we double these values in our requirements.

2.3.3.4 Environmental and lifetime requirements

Operating / storage temperature:
Based on the commercial state-of-the-art of scalar magnetometer above, a temperature range of -15 to 55°C for operation with reasonable margin in -55 to 85°C for storage & OFF-mode is proposed.

Vibration and shock:
Vibration and shock levels are to be determined in function of the mission. It can nevertheless be noted that no specific limiting element and no moving part were identified to that regard.

Radiation:
Compared to other orbits, radiation is typically limited for LEO operation. Exact levels are to be defined in function of the mission orbit and inclination. No specifically radiation sensitive elements were identified at this stage in the OPM components.

Lifetime:
Lifetime requirements can be deduced from the history of magnetometry missions reported in section 1.2. A value of 20 years is given. It can be noted that this value directly influences the accepted sensor drift as the drift ultimately influences the sensor accuracy.

3 HIGH-LEVEL SENSOR DESIGN

3.1 Working principle

3.1.1 Introduction

The proposed magnetometer is based on the zero-field resonance (ZFR) vector magnetometer described previously in (Bertrand et al., 2021). The magnetometer will use Rb-87 alkali atoms enclosed in a microfabricated cell with three sensor chambers, each with an independent optical beam passing through. This design enables vector and free-induction decay (FID) measurements across all three chambers to reduce sources of inaccuracy such as vector light shifts. In a calibration mode, the sensor operates using FID measurements within a single coil system, allowing self-calibration.

The ZFR vector magnetometer in (Bertrand et al., 2021) achieved high-accuracy vector measurements with a sensitivity of up to 130 fT/√Hz. The ZFR technique is particularly advantageous due to its inherently high sensitivity, broad bandwidth, and compatibility with low SWaP requirements. Although the demonstrated technique in (Bertrand et al., 2021) was performed with He-4, we chose Rb-87 for its advantages as an alkali atom, which has been shown to reach fundamental sensitivity in the fT/√Hz range (Lucivero, Lee, et al., 2022), and for its potential to be implemented in atom-based MEMS technology as in (Raghavan et al., 2024), which offers lower SWaP characteristics compared to other systems of its kind, with sensitivity of 18 fT/√Hz.

An additional advantage of the ZFR approach is the elimination of several limitations usually associated with alkali optically pumped magnetometers (OPMs), such as dead zones and heading errors, due to the controlled magnetic environment provided by the coil system. The overall accuracy of the proposed ZFR vector magnetometer is primarily governed by three key factors: precise calibration of coil system parameters, accurate orientation of the optical beams, and effective suppression of vector light shift systematic errors.

The proposed sensor is first-order insensitive to vector light shifts (one important source of drift) and includes self-calibration capabilities to correct for possible drifts in other system components. We minimize vector light shift errors by performing measurements that are sensitive only to magnetic field components perpendicular to the optical beam propagation direction and thus insensitive to vector light shifts, which appear as fictitious fields along the propagation direction. Scalar FID measurements, conducted using the same optical beams and cell cavities, will be used for absolute calibration of the coil system parameters. This calibration method, combined with simultaneous ZFR vector readings, also enables accurate determination of the optical beam orientations relative to the coil frame.

In the subsequent sections we give detailed explanations of the ZFR measurement principle (3.1.2), the implementation of the self-calibration with free-induction decay measurements for scalar calibration (3.1.3), the strategy for self-calibration and proposed measurement sequences (Figure 3-3), and the estimation for sensor's sensitivity and accuracy (3.1.4).

3.1.2 Zero-field resonance (ZFR) vector magnetometer

To illustrate the operating principle of the zero-field resonance (ZFR) vector magnetometer, we consider a simplified scenario as shown in Figure 3-1.a. In this example, the optical beam direction defines the z-axis of the magnetometer, while the x- and y-axes are established by two orthogonal coil pairs. A circularly polarized optical beam, driving sigma-plus (σ+) transitions, propagates along the z-axis. The ZFR occurs in the beam transmission when the transverse magnetic field component (perpendicular to the optical beam) is precisely nulled. At this condition, the atoms achieve efficient optical pumping, maximizing transmission. Conversely, a nonzero transverse magnetic field causes atomic spins to precess away from the optical axis, reducing the optical pumping efficiency and consequently decreasing transmission.

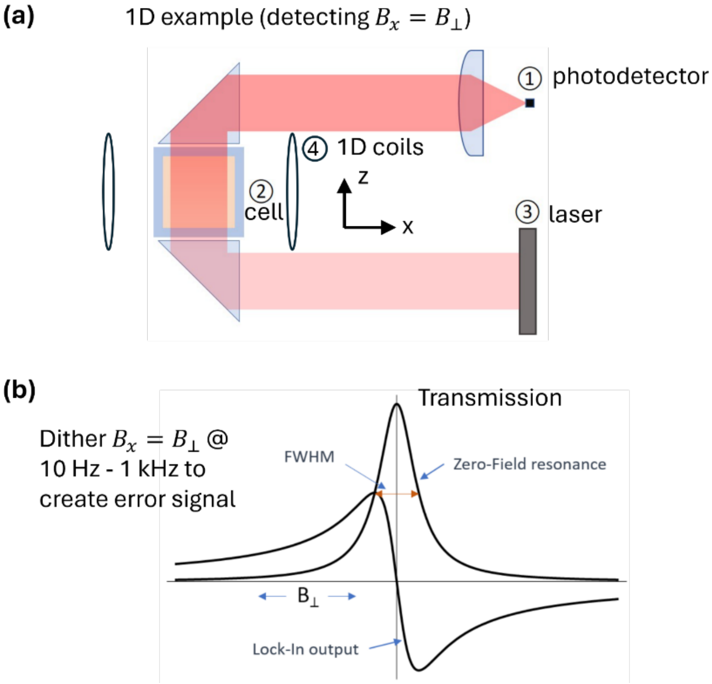

Figure 3-1. Scheme of working principle of the zero-field resonance magnetometer. a) Demonstration of the simplified scenario with one laser beam, one cell and one orthogonal magnetic field. b) Locking technique with transmission signal from the magnetometer. Figure adapted from QuSpin[2].

By applying a small modulation (dithering) to the transverse magnetic fields at distinct frequencies, typically around 1 kHz, an error signal associated with the zero-field resonance condition is generated. Using two orthogonal coil pairs modulated at different frequencies along the x- and y-axes, separate error signals for each axis are obtained simultaneously, enabling precise determination of the zero-field resonance in the transverse plane.

Although methods exist to also detect the ZFR of the magnetic field component along the optical axis using a single optical beam, our implementation specifically avoids measuring this axial component to eliminate systematic errors due to vector light shifts. Instead, we employ three orthogonal optical beams, each passing through a dedicated vapor cell cavity, to fully determine all vector components of the magnetic field without introducing vector light shift systematics. This configuration allows simultaneous, redundant vector measurements as each cell can measure two perpendicular components of the magnetic field, which are also perpendicular to the beam direction. This redundancy provides consistency checks and robustness against systematic errors.

In a 2.25 amg buffer gas environment, similar to the conditions reported in (Raghavan et al., 2024), we estimate the vector light shift errors caused by a 1 mW laser beam, as shown in Figure 3-2. If the laser frequency is loosely locked near the optical resonance (with the precision of tens of MHz), these light shifts can be conservatively kept below 2 nT. To meet our target vector accuracy of about 0.8 nT, as defined in section 2.3.3.2, we calculate that the alignment of both the coil system axes,

---

[2] http://quspin.com/products-qzfm-gen2-arxiv/zero-field-magnetometer-description/

and the optical beam directions must be accurate within about 5 degrees. This level of alignment keeps the vector light shift error below approximately 0.18 nT, which is well within our acceptable range.

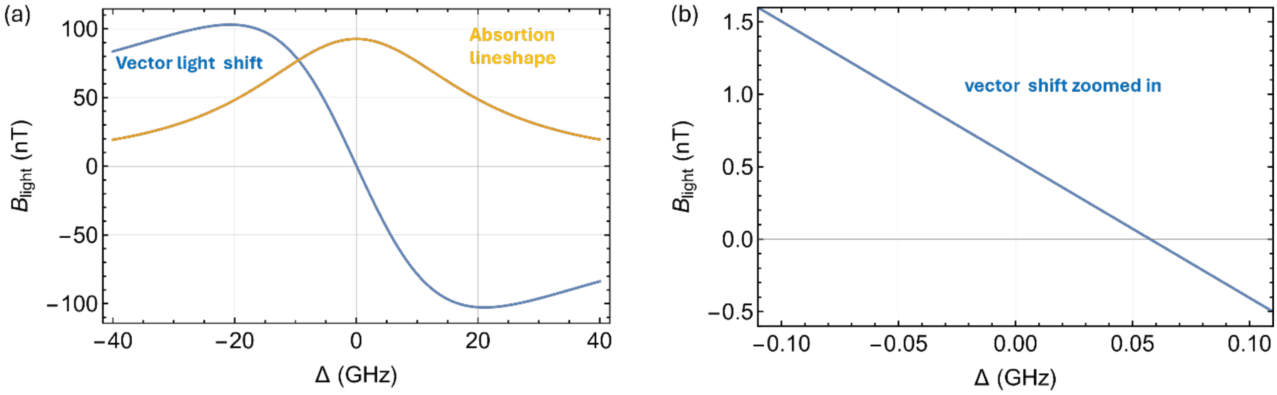

Figure 3-2. Vector light shift simulations for a cell of 2.25 amg (approx. 1700 Torr) buffer gas and optical beam power of 1 mW. The zero crossing in the detuning axes is referenced to the peak of the absorption lineshape. a) Scan of 80GHz in the detuning. b) Zoomed in region where the zero crossing of the vector light shift is shown to be at 0.5 nT.

3.1.3 Self-calibration with free-induction decay measurements

Accurate extraction of the magnetic field vector from ZFR measurements relies on precise modelling of the coil system and accurate knowledge of the optical beam orientations within the coil-defined coordinate system. At a given spatial point within the coil system, the magnetic field generated depends on parameters including coil geometry, currents, and spatial homogeneity.

We consider a cartesian coordinate system with unit vector $(\vec{x}, \vec{y}, \vec{z})$. The coil system consists of three nearly-orthogonal coil pairs that generate magnetic fields along the directions $(\vec{x}_c, \vec{y}_c, \vec{z}_c)$ which constitute a second, non-orthogonal coordinate system. Without loss of generality, we can choose 1) that $\vec{z}$ is aligned with $\vec{z}_c$, and 2) that is $\vec{x}$ is in the plane spanned by $\vec{x}$ and $\vec{z}$. It is then possible to describe the possible misalignments of these systems via non-orthogonality angles $(\delta\theta_x, \delta\theta_y, \delta\phi_y)$ and the relations

$$\vec{x}_c = \vec{x}\,\cos\delta\theta_x - \vec{z}\,\sin\delta\theta_x$$

$$\vec{y}_c = -\vec{x}\,\cos\delta\theta_y \sin\delta\phi_y + \vec{y}\,\cos\delta\theta_y \cos\delta\phi_y - \vec{z}\,\sin\delta\theta_y$$

$$\vec{z}_c = \vec{z}$$

The field generated by the coils is given by $\vec{B}_c = \sum_{k=x,y,z} \vec{B}_{k,c}$, where the contributions of the individual coils are

$$\vec{B}_{x,c} = I_x a_x\,\vec{x}_c \qquad \vec{B}_{y,c} = I_y a_y\,\vec{y}_c \qquad \vec{B}_{z,c} = I_z a_z\,\vec{z}_c,$$

(I_x, I_y, I_z) are the currents in each coil pair and (a_x, a_y, a_z) are coil factors to be determined.

The net field at the cell is $\vec{B} = \vec{B}_0 + \vec{B}_c$ where $\vec{B}_0 \equiv (B_{x,0}, B_{y,0}, B_{z,0})$ is the ambient field to be measured. The total field strength $|\vec{B}|$ is given by

$$\left|\vec{B}\right|^2 = \left(B_{x,0} + \sum_{k=x,y,z} \vec{B}_{k,c} \cdot \vec{x}\right)^2 + \left(B_{y,0} + \sum_{k=x,y,z} \vec{B}_{k,c} \cdot \vec{y}\right)^2 + \left(B_{z,0} + \sum_{k=x,y,z} \vec{B}_{k,c} \cdot \vec{z}\right)^2$$

To determine the 9 coil system parameters (3 coil factors, 3 non-orthogonality angles, and the background magnetic field components) for one cavity, at least nine independent scalar magnetic field measurements are required. These could, for example, use coil currents to apply $\vec{B}_c$ of similar magnitude and along nine directions chosen to fairly represent the full sphere and measure the resulting $|\vec{B}|$. Such a set of scalar measurements provides enough information to uniquely determine all nine parameters of the coil system.

These FID measurements can be made simultaneously for the three cavities because they use independent optical beams. A single measurement sequence can thus find the 27 coil system parameters (nine for each cavity). The ambient magnetic field should be the same in all cavities, which allows comparisons between measurements to help identify systematic errors. Taking more than nine scalar measurements would create an overdetermined dataset. This improves statistical confidence and makes it easier to detect and reject faulty data points during the calibration process.

Figure 3.2 shows two possible calibration sequences. In both cases, there is a dead time that allows the coils' current drivers to change the magnetic field direction between FID measurements or to switch to ZFR operation. The first proposed calibration sequence interleaves FID and ZFR vector measurements. This approach reduces the dead time between ZFR vector measurements and helps to compensate for external magnetic field drifts highlighted in section 3.1.4.2.2. In the second sequence, all FID measurements are performed continuously, without any ZFR vector measurements in between. This method allows us to account for any fast drifts during calibration, resulting in fully calibrated ZFR vector measurements.

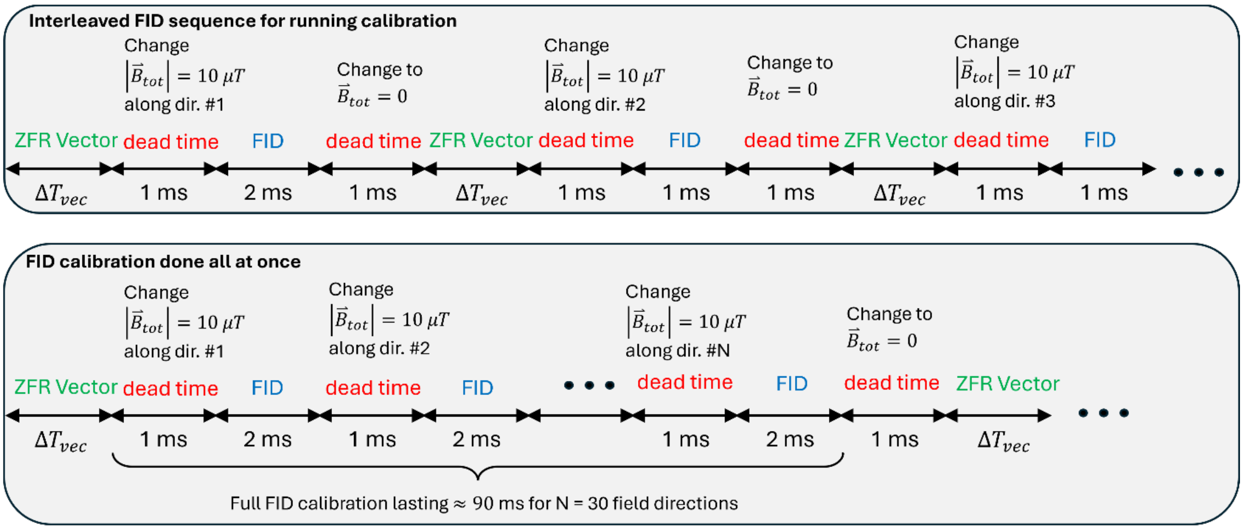

Figure 3-3: Proposed calibration sequences. In the top sequence, individual FID measurements—each taken at a precisely controlled magnetic field orientation using the coil system—are interleaved with ZFR vector measurement periods. The vector measurement periods can be made for long durations (e.g. ΔT_{vec} =10 min.) depending on the anticipated drift in coil or beam parameters that require calibration. In contrast, the bottom sequence consolidates the entire FID calibration into a single, continuous block.

Free-induction decay (FID) measurements, the basis of the scalar measurements, begin with a pumping phase utilizing approximately 1 mW per optical beam, followed by a probing phase conducted at significantly lower continuous-wave (CW) optical power of approximately 10 µW per beam. Optical pumping is performed either continuously or synchronously with intensity modulation at the Larmor frequency. Simulations of the optical pumping and subsequent FID measurements are depicted in Figure 3-4. The choice of 10 µW for the probing phase ensures decoherence from optical scattering remains negligible relative to relaxation due to wall and inter-atomic collisions. Consequently, the vector light shifts at this probing power level are anticipated to be about 100 times smaller than those at the higher power (1 mW) used during ZFR measurements. The vector light shifts during FID measurements are estimated to be around 100 pT, which is negligible for most magnetic field orientations.

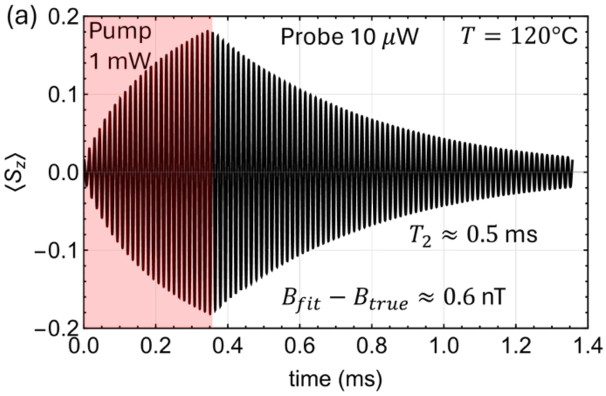

Figure 3-4 FID simulations at 10 µT field strength for a magnetic field perpendicular to the optical beam. The red-shaded region shows polarization build-up due to stroboscopic pumping with 1 mW of peak pump power and 10% duty cycle. The unshaded region shows FID with 10 µW of probe power. a) FID simulation for 120ºC. b) FID simulation for 150ºC. Comparing the fitted FID frequencies to the known Zeeman shift of the F =2 hyperfine manifold, we estimate the FID accuracy for each case. Inaccuracy here is caused by contributions of the nonlinear Zeeman effect and the different gyromagnetic ratios of the F=1 and F =2 manifolds.

Simulations indicate that systematic errors in FID measurements at a magnetic field strength of 10 µT are generally below 1 nT for typical field orientations. This level of accuracy is highly sensitive to the vapor temperature, which influences both the atomic state prepared by optical pumping and the FID coherence time. For instance, at a vapor temperature of 120 °C, the maximum estimated error is approximately 0.6 nT, whereas at 150 °C, it increases significantly to around 12 nT. These small systematic effects, mainly heading errors due to nonlinear Zeeman shifts, must be corrected to reach the required calibration accuracy of approximately 0.1 nT for scalar measurements. Given the stability of the coil system, magnetic fields with well-defined magnitude and direction can be used to pre-calibrate the systematic errors in FID measurements. This pre-calibration requires angular stability better than 10 mrad and field magnitude stability within 100 nT—both of which are readily achievable in our sensor environment.

Accurate optical beam orientations calibration with the coil system frame

The precise orientation of the optical beams relative to the coil system coordinate frame can be determined by comparing magnetic field vectors measured through scalar FID calibrations with vectors obtained from ZFR measurements. Any discrepancy between these indicates misalignment between the optical beam axis (ZFR axis) and the coil-defined z-axis. An alternative approach involves analyzing the coupling between ZFR signals corresponding to each vector component and the modulation signals applied to each coil axis, a method successfully demonstrated in (Dawson et al., 2024).

3.1.4 Estimated sensitivity and accuracy performance

3.1.4.1 Sensitivity

A state of the art zero-field resonance vector magnetometer was reported to achieve 130 fT/√Hz, using helium-4 (Bertrand et al., 2021). In our approach, we propose using rubidium-87 (Rb-87), which is optically accessible in its vapor phase (versus plasma for helium-4), and able to achieve high sensitivity in optically pumped magnetometers, reaching a few fT/√Hz (Lucivero, Lee, et al., 2022).

Given our goal of miniaturization using MEMS vapor cells, it is relevant to highlight the reported performance of a ZFR OPM incorporating MEMS cells with integrated window heating, which achieved a sensitivity of 18 fT/√Hz (Raghavan et al., 2024). Furthermore, commercially available ZFR sensors, such as those developed by QuSpin, report sensitivities of 7–15 fT/√Hz for zero-field OPMs. Their total-field magnetometers demonstrate 3 pT/√Hz scalar sensitivity and 0.1 nT/√Hz vector sensitivity.

Based on current technological benchmarks, miniaturized OPMs can be expected to achieve femtotesla-level sensitivity. However, due to specific aspects of our design, i.e., low probing power compared to the abovementioned OPMs (to minimize vector light shifts) and the presence of the technical noise originating from the current source, we anticipate a sensitivity in the range of 1–10 pT/√Hz. The pT performance remains competitive and well-suited for Earth observation.

3.1.4.2 Accuracy

Based on the previously defined requirements, we target an accuracy of 0.8 nT.

To maintain this level of accuracy, the orientation of all three beams within the calibrated coil system must be known with a precision of 10 µrad. As mentioned earlier, this will be achieved by comparing the FID calibrations (referenced to the coil-defined z-axis) with the ZRF measurements (referenced to the optical beam z-axis). Any discrepancy between these measurements reflects misalignment between the optical beam axis and the coil-defined z-axis. Alternatively, to ensure the required accuracy, the direct measurements of the non-orthogonality of the ZFR optical axes, following the technique described in in (Dawson et al., 2024) could be implemented.

We will implement a calibration of the FID accuracy for the known magnetic field strength and orientations used for the coil system. This procedure compensates for heading errors in the FID measurements. A similar calibration strategy was successfully implemented in the CPT magnetometer onboard the China Seismo-Electromagnetic Satellite, as detailed in (Pollinger et al., 2018a). The entire setup reached an accuracy of 0.19 nT.

3.1.4.2.1 Influence of Startracker stray fields to accuracy

The constraints on the distance of other devices, such as the Startracker, is given by the following equation:

$$\frac{m}{d^4} < \frac{2\pi}{3\mu_0}\frac{\Delta B}{\Delta x},$$

with d [m] the distance from the device (e.g. Startracker), $m_{NanoMagSat} = 35$ µA m^2 and $\frac{\Delta B}{\Delta x}$ [T/m] the gradient in the vapor-cell. Taking a safe value of $\Delta B = 0.1$ nT and knowing that the diameter of the vapor-cell volume of interest is $\Delta x = 12$ mm, this puts the following constraint on the distance with the tracker of:

$$d > 22.4\ cm.$$

Note that $d_{NanoMagSat} = 10$ cm.

3.1.4.2.2 Influence of deadtimes to accuracy

It is important to guarantee that the magnetic field gradient during the recalibration phase is reasonably small compared to the target accuracy. Simulations on the influence of deadtimes to accuracy is estimated from the Swarm A dataset. The results are presented on Figure 3-5 and Table 3-1.

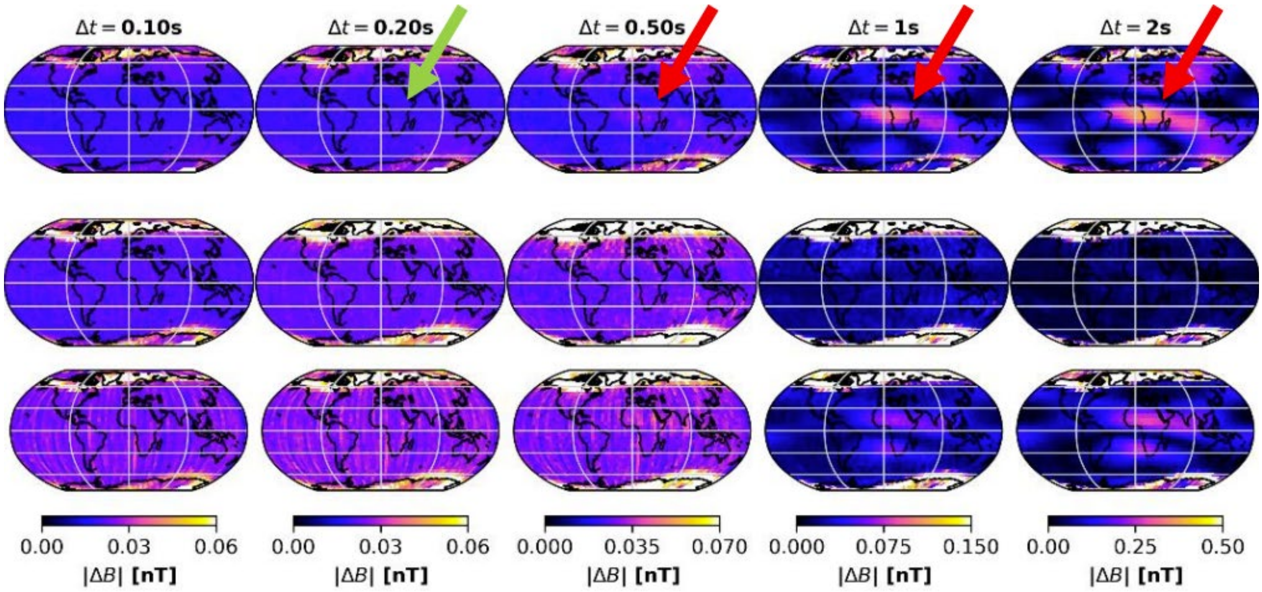

Figure 3-5: Field gradient with respect to time estimated with Swarm A data. Each row is for a different vector magnetometer. The arrows highlight a region of interest of central Africa over which the accuracy loss rate is important.

Conclusions from the simulation show that deadtimes up to 2 s leads to an error of less than 0.8 ns. However, the duration of the full FID calibration presented on Figure 3-3 is expected to be of the order of 100ms, leading to an accuracy error of the order to 136 pT.

Table 3-1: Field gradient statistics with respect to deadtime for Swarm A. Rates indicates percentiles higher than our target accuracy of 0.8 nT.

Deadtime [s]	99th percentile [nT]	95th percentile [nT]
0.02	0.052	0.036
0.04	0.114	0.077
0.10	0.136	0.091
0.20	0.141	0.094
0.50	0.155	0.103
1.00	0.205	0.099
2.00	0.363	0.282
3.00	0.798	0.619
5.00	2.210	1.708
10.00	8.799	6.809

3.2 System-level approach

3.2.1 High-level description

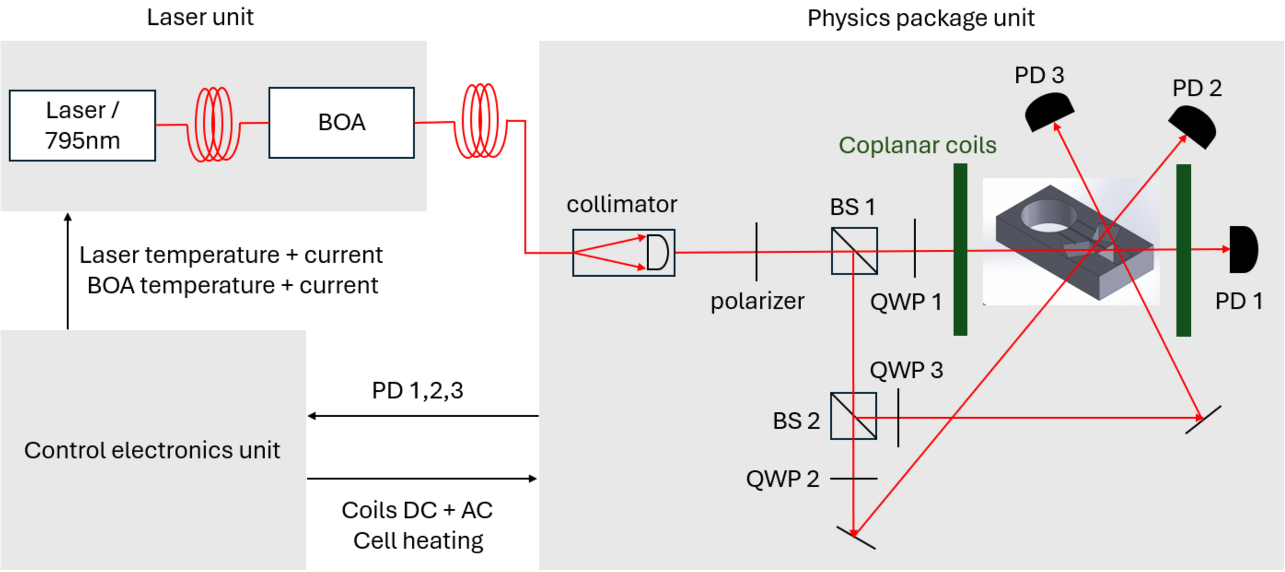

Figure 3-6: High-level schematics. BS: beam splitter, QWP: quarter-wave plate, PD: photodiode, BOA: booster optical amplifier.

Figure 3-6 shows the high-level structure of our scalar/vector OPM. Its architecture is divided into three subsystems: the laser, physics package and control electronics units. The physics package unit is, as in past satellite missions described in subsections 3.1.2 and 3.1.3, located far from the two other units to avoid stray fields.

3.2.1.1 Laser unit

The laser unit consists of a 795-nm fiber-coupled DFB/DBR laser followed by a booster optical amplifier (BOA) whose output is fiber coupled to the physics package unit. The laser frequency is locked onto the physics package vapor-cell Doppler-broadened signal using the signal of one of the three physics package photodiodes through a modulation/demodulation lock-in amplifier scheme. The BOA serves as optical amplifier to tune the laser intensity to the three different power levels required for the vector, scalar pumping and scalar probing OPMs phases as described in subsection 3.1.4. The laser power is locked using one of the three photodiodes of the physics package. Note that a fourth photodiode might be necessary to lock the laser frequency and intensity without increasing the overall sensor SWaP too much.

3.2.1.2 Physics package unit

The physics package unit contains the three-cavity microfabricated vapor cell similar to the C-MAC atomic clock (Haesler et al., 2017) with ^{87}Rb and N_2 buffer gas. Note that to avoid clipping this vapor-cell should be slightly wider than the vapor-cell referenced in (Haesler et al., 2017). Preliminary estimations from the computer assisted design model suggest a vapor-cell with dimensions 18 x 12 x 1.9 mm^3.

The light coming through a fiber from the laser unit is collimated in free space, polarized and divided into three optical paths with equal light intensity thanks to two beams splitters BS 1 (1/3, 2/3) and BS 2 (1/2, 1/2). Both vector and scalar operation require circularly polarized light which is achieved by placing a quarter wave plate on each optical path. The three optical axes are directed to the three individual cavities forming an orthogonal basis each entering the cell with a 45° angle with respect to the cell's surface.

The vapor-cell is placed between two three-layers PCBs (Tayler et al., 2022b). Each pair can be designed to act on one of the three optical axes allowing for zero-field nulling during the vector operation or physics package calibration during the scalar phase. Note that these three orthogonal optical axes are not parallel to the vapor cell natural axes but obtained from two subsequent 45° rotations along two of the cell's principal exes. Figure 3-7 shows a possible architecture for the three-cavity vapor-cell enclosed in the two PBCs along with the three orthogonal optical axes.

As pointed out in subsection 3.1.3, the field homogeneity inside of the three cavities is a key parameter. Fortunately, tools like *bfieldtools* (Zetter et al., 2020) allow for simulations of such coplanar coils with constraints such as holes for laser access to the physics package.

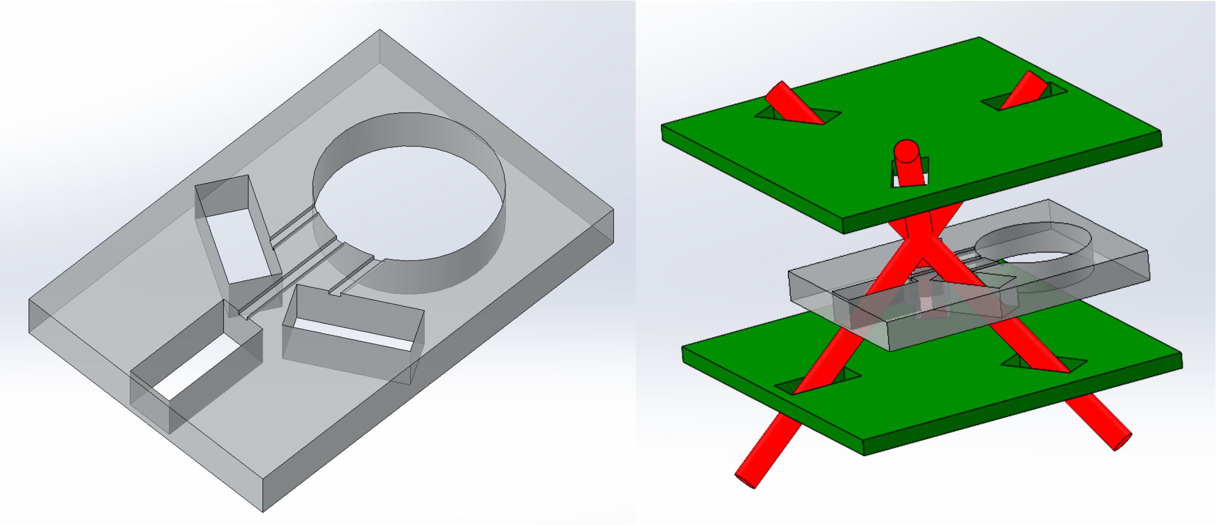

Figure 3-7: Left: example three-cavity vapor cell with reservoir with dimensions 12 x 18 x 1.9 mm^3. Right: Cell enclosed between two three-layer coplanar coils with the 3 perpendicular laser beams.

Finally, the three photodiodes are placed at the end of each optical path. Their signals will be used for zero-field nulling, laser frequency stabilization, laser intensity stabilization and OPM calibration during the scalar phase.

The size of the coils remains to be determined with proper simulations using, for instance, bfieldtools (Zetter et al., 2020). It is however possible to provide a coarse estimate by finding the width of a square Helmholtz pair such that the field inhomogeneity in the vapor-cell is comparable to the one in (Tayler et al., 2022b). Results of this coarse simulation are presented on Figure 3-8, with an estimated worst-case scenario of 47 mm. Note that the inhomogeneity figure of merit is calculated as the maximum relative deviation with respect to the field in the center of the volume.

It is important to note that biplanar coils generated by bfieldtools are not separated by the same distance as their width, which is the case for circular and square pairs of Helmholtz coils.

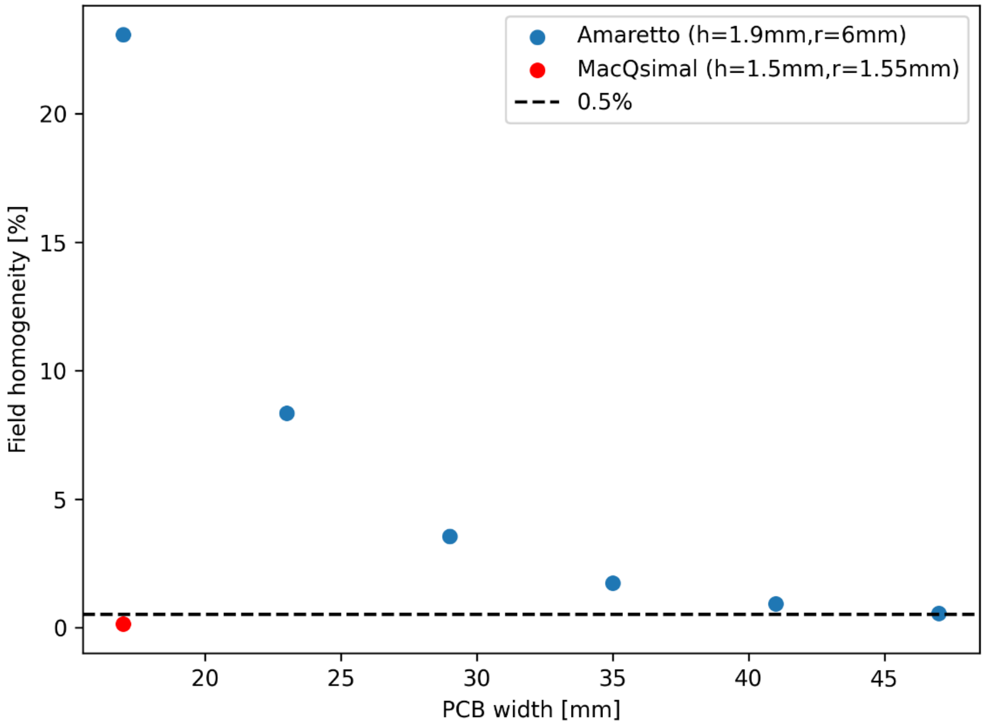

Figure 3-8: Field homogeneity for different interrogation volumes with respect to the width of a pair of square Helmholtz coils.

3.2.1.3 Control electronics unit

To meet the requirements for speed, particularly the high acquisition rate needed by FID OPMs, a FPGA controller should be used as the main electronics controller. Note that to reduce SWaP, an ASIC could be eventually developed.

The control electronics unit also contains the driver for the coils, BOA, laser, DACs and ADCs.

3.2.2 Product tree

Table 3-2 lists the components needed for assembling the OMP.

Table 3-2: Product tree for the proposed OPM sensor.

Tree item	Designation	Description	TRL
1	**LSS**	**Laser subsystem**	4-5
1.1	- CW source assembly		7
1.1.1	- - fiber-coupled DFB laser	795nm pump diode	7
1.1.2	- - fiberized BOA	Optical amplifier	7
1.1.3	- - fibre	Link to physicks package	7
2	**PPSS**	**Physics package subsystem**	2-3
2.1	- Optical path		
2.1.1	- - root beam		
2.1.1.1	- - - collimator	Free-space transition	7
2.1.1.2	- - - beam splitter	1/3, 2/3 beam splitter	7
2.1.2	- - optical axis 1	1/3 output of item 2.1.1.2	
2.1.2.1	- - - quarter wave plate 1		7
2.1.2.2	- - - mirror 1		7
2.1.2.3	- - - photodiode 1		
2.1.3	- - optical subbranch	2/3 output of item 2.1.12	
2.1.3.1	- - - beam splitter	50/50 beam splitter	7
2.1.4	- - optical axis 2	output 1 of item 2.1.3.1	
2.1.4.1	- - - quarter wave plate 2		7
2.1.4.2	- - - mirror 2		7
2.1.4.3	- - - photodiode 2		7
2.1.5	- - optical axis 3	output 2 of item 2.1.3.1	
2.1.5.1	- - - quarter wave plate 3		7
2.1.5.2	- - - mirror 3		7
2.1.5.3	- - - photodiode 3		7
2.2	- vapor cell	Microfabricated cell with three optical cavities	5
2.3	- biplanar coils	Control magnetic fields on optical axis 1,2 and 3	4
2.3.1	- - lower PCB coil		7
2.3.2	- - upper PCB coil		7
2.4	- Breadboard	Glass breadboard	
2.5	- Local electronics		
2.5.1	- - Transimpedance amplifier 1		7
2.5.2	- - Transimpedance amplifier 2		7
2.5.3	- - Transimpedance amplifier 3		7
3	**CESS**	**Control electronics subsystem**	3-4
3.1	- FPGA controler		>= 7
3.2	- Multiplexed ADC		>= 7
3.2.1	- Multipleplexed DAC	For reading laser, SOA and cell temperature	>= 7
3.2.2	- TIAs	One for each photodiode	>= 7

Buyable components have been set to TRL 7 except for electronics components that have TRL >= 7. The vapor-cell is expected to be of the order of TRL 5. Although they have been already demonstrated in literature, PCBs have the lowest TRL (4) as specific models have to be simulated and built without a priori knowledge how to ensure our requirements for field homogeneity.

Finally, the individual subsystems TRLs are defined slightly lower than their lowest TRL component to account for the subsystem development risk. An overall TRL of 2-3 is estimated, considering that the interrogation schemes need to be validated to reach TRL 3.

3.2.3 Thermo-mechanical concept

Figure 3-9 shows a possible thermo-mechanical design implementation with physics package and laser subsystems. The control electronics subsystem was not rendered as it is too early to speculate on its final form. The SWaP of the control electronics subsystem will however be discussed in the following paragraphs.

The physics package and the laser subsystems are separated by optical fiber to avoid stray fields coming from the electronics and high currents needed to operate the laser head and optical amplifier. The light is collimated to free space and enters the bottom of the physics package. Discrete free-space optics divide the light intensity into three optical beams that are orthogonally shining to the vapor-cell passing through the two coplanar coil PCBs. Three photodiodes are placed on the upper PCB.

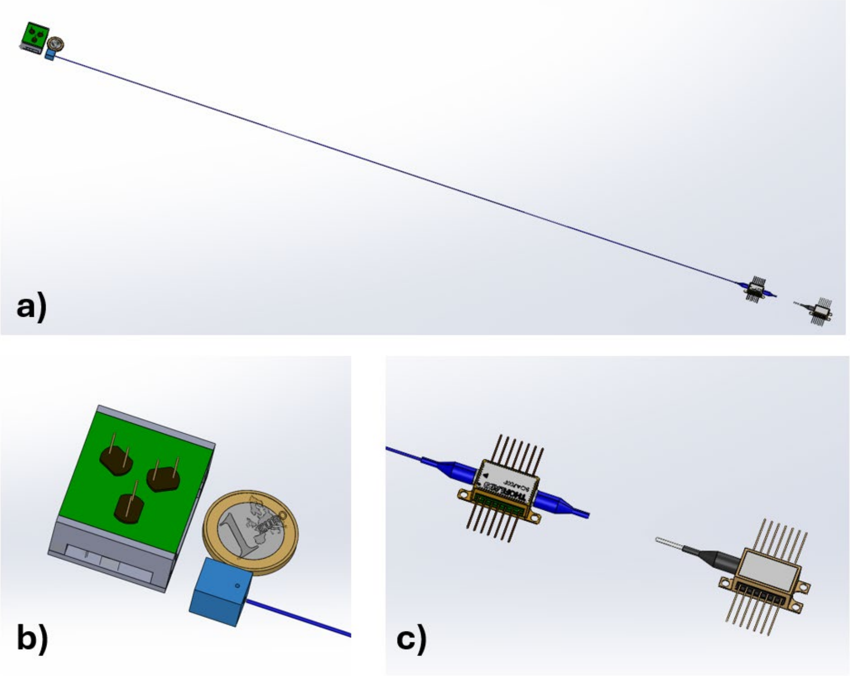

Figure 3-9: a) Top view of the thermo-mechanical concept. b) physics package alongside the collimator. c) Laser head and SOA.

3.2.3.1 Laser subsystem

The laser subsystem contains a 795-nm laser whose signal's intensity is controlled by an optical amplifier such as a BOA or SOA. Although the proposed three-axis OPM architecture relaxes the need for frequency stability, the source laser FWHM still needs to be reasonably small which favors the choice of a fiber DFB laser.

3.2.3.2 Physics package

3.2.3.2.1 Baseplate

The physics package baseplate could be built out of fused silica with the remaining elements (optics, PCBs, vapor-cell) glued in layers. The fused silica choice is motivated by the need for excellent vector pointing stability as mentioned in section 3.1.3. Zerodur could be also considered if high vector pointing stability is needed or if it suits best the satellite bench.

3.2.3.2.2 Vapor cell

The microfabricated vapor-cell is held by an isostatic holder that allows for securing and heating the vapor-cell while optimizing thermal dissipation. Figure 3-10 shows an illustrative isostatic holder and the C-MAC holder as reference.

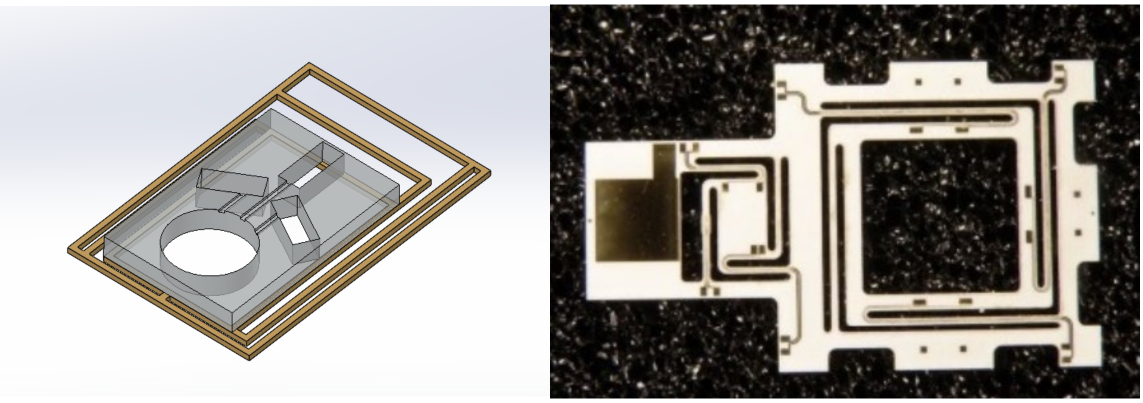

Figure 3-10: LEFT: CAD 3-cavity vapor-cell on isostatic holder. RIGHT: isostatic holder for the C-MAC atomic clock (Haesler et al., 2017).

Power consumption for heating the vapor-cell is lower in vacuum is considerably lower compared to ground operation. Figure 3-11 shows that the power consumption drops to a level of 35 mW in low-pressure conditions.

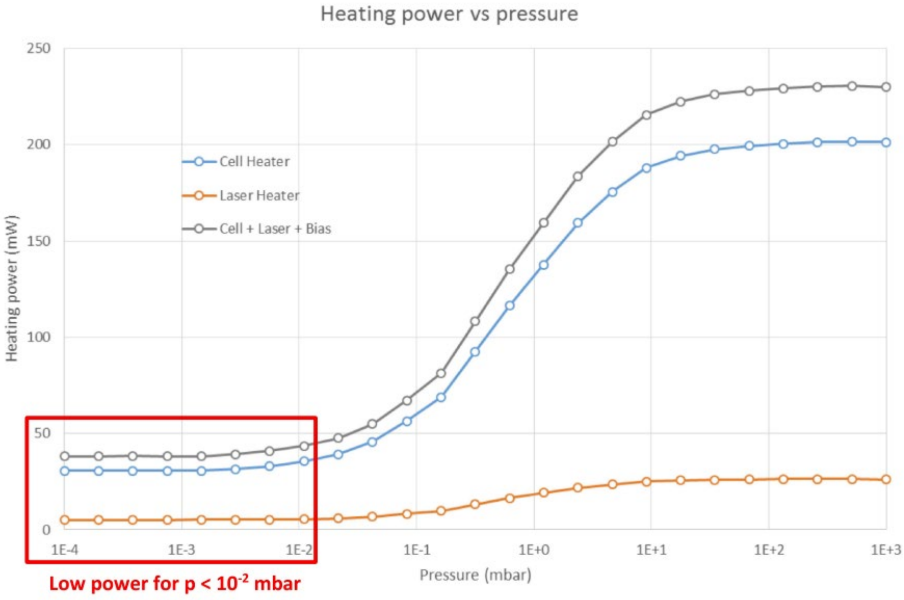

Figure 3-11: Power consumption of C-MAC vapor-cell heating with respect to pressure.

Note that, depending on the vapor cell filling method and the use case, the lifetime of atomic vapor cell can be limited (Karlen et al., 2017). This is typically the case for cells filled with if filled with CSEM patented RbN_3 method in the case of miniature atomic clocks. For the present case, given the relatively high N_2 pressure required for OPM application, the typical amount of Rb generated in a dedicated cell is in the ~160µg range (Raghavan et al., 2024b). The typical required RbN_3 amount for 10 years operation at ~100°C is in the order of 0.6 µg. This indicate that 20 years operation should likely not be a problem. The Rb consumption is nevertheless strongly influenced by the operating temperature and detailed calculation would be required to consolidate this statement. Note in addition that CSEM has been carrying out activities to refine the values published in (Karlen et al., 2017).

3.2.3.2.3 Coils

As already mentioned, the coils will take the form of three coplanar coils placed on two PCBs following the approach of (Tayler et al., 2022b). Due to the nature of the geometry, the coils are expected to be wider than the 17 mm reference. Current CAD dimensions show a 24-mm wide lower coil with a 30-mm wide upper coil. These dimensions are governed by the need for light feedthrough and stacking of the physics package elements.

Since field homogeneity is a key parameter of the approach, special care must be taken when designing the coils. It is possible that wider coils will be needed to meet the homogeneity requirement.

Unfortunately, the literature does not provide resistance and inductance values needed for estimating the power consumption when the coils are driven. However, from (Tayler et al., 2022b), it can be estimated that a maximal current of 300 mA would be needed to generate a field of 65 uT, the maximal range of our sensor.

3.2.3.3 Electronics

As already highlighted, electronics should at least include the following elements: a FPGA as controller, one multiplexed ADC, one multiplexed DAC and three TIAs. Note that 300 mW power consumption for the remaining unlisted components is estimated. Table 3-3 provides a list of potential candidates along with their power consumption.

Table 3-3: Preliminary list of need components for the electronics with potential candidates.

Func.	Des.	Current [mA]	Voltage [V]	Power [mW]	N° of devices	Power [mW]	Package	Size [mm]
TIA	ADA4350	10	5	50	3	150	TSSOP-28	10x7
ADC	ADS8688	16	5	80	1	80	TSSOP-38	10x7
FPGA	Igloo nano AGLN250	100	1.5	150	1	150	VQG100	14x14
DAC	AD5676R	4	5	20	1	20	LFCSP	4x4
Others						300		
Total						**700**		

3.2.4 SWaP

3.2.4.1 Estimate

Table 3-4: SWaP estimate and comparison with requirements.

*Under vacuum
**Power consumption of the coils to be determined based on final inductance value.

Subsystem	Size [L]	Weight [g]	Power [W]
Laser	0.10	40	1
Physics package	0.08	30	50mW* + coils**
Control electronics	0.06	50	0.7
Total	**0.22**	**120**	**1.75**
Requirements	0.20	200	2.00

The laser and physics package subsystems volumes are estimated from the CAD presented in Table 3-3.

The physics package volume is based on the estimated worst case scenario (47 mm wide PCB coils) devised in which leads to a total size above the targeted requirements. This value is nevertheless to be confirmed with a more detailed design and simulations with non-square coils. It is estimated that the electronics components presented in Table 3-3 would fit on a 60x60 mm^2 with height 15 mm.

The weight of the laser subsystem is estimated by weighing a butterfly package whose weight is rounded up to 20g per piece. The weight of the control electronics is estimated from the component list of Table 3-3 and estimated PCB area. The result is rounded up to account for missing elements such as coil drivers. The weight of the physics package is estimated by using the CAD volume of the holder and assuming fused silica. All the free-space optics weights are estimated to be ~1g. The weight of the vapor-cell is estimated to be to the same order of the C-MAC's which was measured to be 0.1g.

The power consumption of the laser physics package is estimated from the datasheets of a typical butterfly 795-nm DFB laser and Thorlabs 780P BOA. Both estimates include heating which makes most of the power budget at roughly 0.5 W for each butterfly package.

Power consumption of the physics package is estimated to 35 mW for heating the vapor-cell. Unfortunately, since no value for the coils' inductance is provided in the literature, the power consumption of the coils is still to be to be estimated.

Power consumption of electronics is estimated using Table 3-3.

3.2.4.2 Reduction strategies

3.2.4.2.1 Use of a VCSEL

Since the requirements for the maximum optical power are of the order to 3 mW at peak consumption, the DFB/DBR laser could be replaced by a lower consuming laser such as a VCSEL. With a typical power of 0.1 mW, its output could be amplified by the BOA to the required power level. However, even in our proposed architecture which reduces systematics such as the light shift, the linewidth of the laser should not be allowed to be arbitrarily wide. It is hence not certain that fibered-coupled VCSELs with sufficiently narrow linewidth exist.

3.2.4.2.2 ASIC development

Our initial proposal features a FPGA as controller for the OPM. It is foreseen that the development of an ASIC will help reducing the power consumption of the control electronics subsystem.

3.2.5 Final level 1b product error

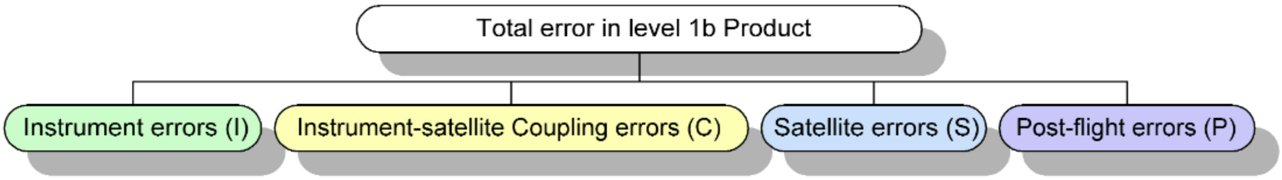

***Figure 6.1**: Error sources contributing to the final Level 1b product error.*

Figure 3-12

According to Figure 6.1 in ‘ESA Mission Experts Division. (2006)’ the total error in Level 1b products consists of four parts: instrument error (I), instrument-satellite coupling errors (C), satellite errors (S) and post-flight error (P).

The estimation for instrument error (I) is sensor-intrinsic and given in section 3.1.4.2 with a value of 0.19 nT.

The instrument-satellite coupling errors (C) can be minimized by larger distances between instruments to reduce the cross-talk, using magnetic field measurement at the end of a long boom, and using temporal synchronization of all instruments (e.g. GPS pulse). All satellite parts close to the magnetic field sensors shall be of non-hard and non-soft-magnetic materials. Magnetic field impact shall be reduced through design, for example by field canceling (e.g. on Swarm satellite solar panels).

The satellite errors (S) mainly result from position and attitude determination errors of the satellite. The table below provides an overview of impact for different sources on Swarm satellite magnetometer. The required accuracy values in this document are given in RMS for the magnetic field magnitude. We have harmonized the values in the reference document (SW-RP-EAD-SY-0004, Issue 7) to ensure comparability with the requirements. If no 1σ values are provided, 2σ values have been divided by 2 to receive 1σ, and if no magnitude values are available, the magnitude has been calculated from given component’s 1σ.

These relatively small values can only be estimated during on-ground tests. During the VFM-STR inter-calibration test, the attitude and optical bench stability has been estimated. Impacts of instruments, current loops and satellite material have been estimated during system magnetic tests by sequentially switching them on and off. Timing of instruments has been checked with respect to GPS pulse. On-ground calibration also helps validating models, e.g. for solar arrays or magnetorquers. The given values for magnetorquers are valid after the impact model has been subtracted since magnetorquers are designed to produce large magnetic fields for attitude control.

Table 3-5: List of error sources for the level 1b product.

	Error Source	**Error (Magnitude, 1σ)**	**Reduced by model or calibration**	**Reference**
C	Remanent magnetic field	0.0315 nT		Swarm Performance Prediction (SW-RP-EAD-SY-0004, Issue 7, 15.11.2013, Table 4-14)
C	Induced magnetic field	0.044 nT		Swarm Performance Prediction (SW-RP-EAD-SY-0004, Issue 7, 15.11.2013, Table 4-15)
C	Solar array currents	0.025 nT	yes	Swarm Performance Prediction (SW-RP-EAD-SY-0004, Issue 7, 15.11.2013, Table 4-16)
C	Magnetorquer currents	0.125 nT	yes	Swarm Performance Prediction (SW-RP-EAD-SY-0004, Issue 7, 15.11.2013, Table 4-17)
C	Timing error (GPS pulse accuracy of 10 ns)	<1E-16 nT		
S	VFM-STR intercalibration (Attitude)	0.247 nT		Swarm Performance Prediction (SW-RP-EAD-SY-0004, Issue 7, 15.11.2013, Table 4-13)
S	Position	0.027 nT		Swarm Performance Prediction (SW-RP-EAD-SY-0004, Issue 7, 15.11.2013, Table 4-18)
P	L1b Data Processing	0.043 nT		Swarm Performance Prediction (SW-RP-EAD-SY-0004, Issue 7, 15.11.2013, Table 4-18)
I	Vector OPM	0.190 nT		Estimated accuracy of proposed sensor architecture.
	Sum Bias (correlated) **Sum Bias (uncorrelated)**	**0.732 nT** **0.344 nT**		

Attitude impacts on the magnetic field error already comprise the largest portion of the budget. Combined with instrument-satellite coupling, satellite error and processing error the 0.8 nT budget is nearly reached, even for a magnetic clean satellite design like that of Swarm which puts strong constraints on the instrument accuracy.

Note that both pessimistic and optimistic cases, namely when noise contributions are correlated and uncorrelated, respectively, are calculated. In both scenarios, the estimated total error bias is below our target of 0.8 nT.

3.2.5.1 Future potential

The three most notable contributors to the error budget are the magnetorquer currents, the VFM-STR intercalibration and the proposed sensor itself. Efforts towards reducing the first two would lead to a sensor-limited error budget of 0.2 nT. While Magnetorquer currents influence can be mitigated through calibration while the VFM-STR intercalibration could be mitigated using OPMs arrays.

Indeed, arrays of 3-axis OPMs are already used in the field of magnetoencephalography (MEG) to discriminate the field of interest from local noise (Tierney et al., 2022). While the underlying satellite dipole model and number of required OMPs still remains to be determined, these techniques have the potential to reduce the VFM-STR intercalibration contribution while allowing to bring the sensor array closer than that of the satellite, reducing its footprint.

3.2.6 Compliance with requirements

Given the estimation provided in this section, we can provide a first estimate of the compliance to the requirements defined inTable 2-29.

Ref.	Parameter	Unit	Req.	Expected value	Compliance	Remark
Functional						
RQS10	1 highly accurate vector magnetic field strength signal				C	
RQS20	Functional modes ON and OFF				C	
RQS30	No maintenance in OFF mode				C	
RQS40	“health status” and telemetries to debug and assess lifetime behaviour				C	
RQS50	Data rate / Cadence	Hz	250	500	C	Except during recalibration (~1s every day)
RQS60	Warm-up time	s	< 3600	< 150	C	Time for heating a vapor-cell
Performance						
RQS110	Dynamic range	µT	65		C	
RQS120	Bandwidth	Hz	250	500	C	
RQS130	Resolution	pT/sqrt(Hz)	10	10	C	
RQS140	Accuracy	nT	< 0.8	0.34-0.73 nT	C	L1b error – range discussed in section 3.2.5
RQS150	Drift	pT/month	3	<1	C	Value calculated from RQS140 and RQS370, with daily recalibration
RQS160	Deadzone	Deadzone free			C	
Size, Weight and Power consumption						
RQS210	Mass	gr	< 200	120	C	C with design goal (< 100 g) TBD at PDR stage
RQS220	Volume	cm^3	< 200	220	TBC	TBC at PDR stage. Design goal remains (< 100 cm^3)
RQS230	Voltage supply	V	TBD		C	Not a limiting element at this stage, design can be adapted to the SV supply voltage

RQS240	Sensor power consumption during warm-up	W	< 3	2	C	
RQS250	Power consumption	W	< 2	1.75	C	
Environment						
RQS310	Operating temperature	°C	-15 to 55		C, TBC	No limiting element identified at this stage
RQS320	Storage & OFF mode temperature	°C	-55 to 85		C, TBC	No limiting element identified at this stage
RQS330	Random vibration	grms	TBD		TBD	
RQS340	Micro-vibration	mg	TBD		TBD	
RQS350	Shock	g	TBD		TBD	
RQS360	Radiation	Krad	TBD		TBD	
RQS370	Lifetime	years	20		C, TBC	No lifetime limiting element identified at this stage
RQS380	Operates both in vacuum and ambient conditions				C	

Table 3-6: Comparison between the sensor requirements and the estimated performances of our approach. Note that only sensor-relevant parameters are compared.

Note that the 250 Hz cadence might not be guaranteed during recalibration phases. It is important to stress that the duration of this phase not final yet and will strongly depend on the time need for one FID measurement as well as the ability to measure on the three axes simultaneously which might divide the calibration duration by 3.

For these reasons, the duration of the calibration state is estimated to last between 9 and 27 ms, which would respectively put the cadence in and out of spec during recalibration phases only.

4 TECHNOLOGY DEVELOPMENT PLAN

4.1 Model philosophy

The high-level description of all development phases and model philosophy is expressed in Table 4-1 with corresponding models. They are detailed in section 4.2.
It is proposed to start the development activities with a derisk phase including the validation of the proposed approach and of the achievable requirements in a laboratory experiment. The rest of the development plan follows a standard space instrument flow.

Phase	Model	Start TRL	Target TRL	Start date	End date	Prototype, demonstrator. Normally more than just labo experiment.
DR	De-Risk	2-3	3	Q1 2026	Q4 2026	Objective 1: Demonstration of the proposed interrogation scheme in a laboratory experiment with representative key elements (cell, laser). Objective 2: Confirmation of achievable performances (sensitivity, accuracy, drift) Objective 3: refinement of the high-level architecture and update of the system requirements
B	Elegant Breadboard (EBB)	3	4-5	Q1 2027	Q3 2028	Objective 1: Prototype, demonstrator close to the final equipment in terms of mass, volume, power consumption functionality. Objective 2: Preliminary design of the laser, physics and control sub-systems in view of the EM. Objective 3: Evaluation of critical elements in term of environment (radiation, vibration, shock, temperature). The Material, Parts and Processes Evaluation will be conducted in this phase as continuation of the derisk activity.
C1	Engineering Model (EM)	4-5	6	Q4 2028	Q2 2030	Objective 1: Engineering Model design and MAIT. EM will be form fit and function identical to the FM. Preliminary environmental test will be conducted with EM. Objective 2: QM/FM design.
C2	Engineering Qualification Model (EQM) or Qualification Model (QM)	6	7	Q3 2030	Q1 2032	Objective 1: One QM Model identical to the FM that will be submitted to a test campaign with environmental constraints higher than expected in the reality. Objective 2: One EQM for long-term testing. EQM's may use not qualified EEE parts (mainly for schedule reason) but the selected replacement parts must be in the same packaging and with same performances. Objective 3: The product qualification review will be conducted at the end of this phase. Full qualification of the product will be conducted after successful FDM operation in orbit.

Table 4-1: Summary table of the development phases

4.2 Development plan

In this paragraph, a preliminary development plan is proposed to reach TRL 7. The timeline can nevertheless be adapted depending on the effective effort put on the development in case an earlier availability of the product is needed *e.g.* for a dedicated magnetometry mission.

4.2.1 De-risk

Phase start date	Q1 2026	TRL start	2-3
Phase end date	Q4 2026	TRL end	3
Objectives	Objective 1: Demonstration of the proposed interrogation scheme in a laboratory experiment with representative key elements (cell, laser). Objective 2: Confirmation of achievable performances (sensitivity, accuracy, drift) Objective 3: refinement of the high-level architecture and update of the system requirements Inputs: AMARETTO projects results / ESA SoW Outputs: De-risking activities results and recommendations for EBB and updated high-level design and requirements. Closure meeting: System Requirements Review (SRR)		
Model(s)	n/a		
Associated milestone	n/a		
Deliverables	No H/W or S/W. Documentation including test data (raw)		
ROM cost estmiate	650’000€[3]		

4.2.2 Phase B

Phase start date	Q1 2027	TRL start	3
Phase end date	Q3 2028	TRL end	4-5
Objectives	Objective 1: Prototype, demonstrator close to the final equipment in term of mass, volume, power consumption functionality. Objective 2: Preliminary design of the optical bench (physic package) and of the electronic (EM design). Objective 3: Evaluation of crucial elements in term of environment (radiation, vibration, shock, temperature). The Material, Parts and Processes Evaluation will be conducted in this phase as continuation of derisk activity.. Inputs: DR conclusions / ESA SoW Outputs: preliminary design, updated requirements. Closure meeting: Preliminary Design Review (PDR)		
Model(s)	EBB		
Deliverables	EBB and EGSE to interface it including related S/W. Documentation including test data (raw), PDR data package.		

4.2.3 Phase C1

Phase start date	Q4 2028	TRL start	4-5
Phase end date	Q2 2030	TRL end	6
Objectives	Objective 1: Engineering Model which will be form fit and function identical to the FM. If the FM included redundancy, the EM does not necessary include it. Preliminary environmental test will be conducted with EM. Objective 2: QM/FM design updated. Outputs: DPL, DML, STM, ICD with test measurements Closure meeting: Critical Design Review (CDR)		
Model(s)	EM, SM		

---

[3] Note that the cost can be adjusted in function of the tasks actually foreseen in the activity and that this value is provided without any guarantee.

Deliverables	SM and EM with EGSE to interface it including related S/W, PDR data package

4.2.4 Phase C2

Phase start date	Q3 2030	Clock TRL start	6
Phase end date	Q1 2032	Clock TRL end	7
Objectives	Objective 1: One QM Model identical to the FM that will be submitted to a test campaign with environmental constraints higher than expected in the reality. This model will be submitted to radiation test at clock level. Objective 2: Five EQM's for long-term testing. EQM's may use not qualified EEE parts (mainly for schedule reason) but the selected replacement parts must be in the same packaging and with same performances. The long-term test campaign will start after 9 months in the C2 phase (for EQM manufacturing) for a minimum duration of 2 years (extendable to possibility 3.5 years if run in parallel with D1 phase for a full 15 years demonstration). Objective 3: The product qualification review will be conducted at the end of this phase. Full qualification of the product will be conducted after successful FDM operation in orbit. Inputs: Phase C1 results, ESA SoW Outputs: DPL, DML updated with all elements qualified Closure meeting: Qualification Review (QR)		
Model(s)	Engineering Qualification Model (EQM) or Qualification Model (QM)		
Deliverables	EQM or QM, CDR data package		

5 CONCLUSION

A state-of-the-art review of OPM magnetometers and scientific spaceborn earth observation magnetometry has been realized. Based on these reviews, observation scenarios have been identified, and performance requirements have been deduced for earth observation.

Instrument-level requirements have then been gathered for two types of OPMs (vector and scalar) following the common approach of space magnetometry missions. These requirements include performance requirements deduced from the observation scenarios already identified and from the possible performance identified in the state-of-the-art review. Size, weight, power consumption as well as environmental requirements have also been identified.

Proposal for a single physics package, dual use scalar-vector OPM is described with the goal of reducing the SWaP compared to separated OPMs approach. To reduce systematics, a set of 3 orthogonal ZFN OPMs operated in one vapor-cell filled with ^{87}Rb and N_2 buffer gas is suggested with the advantage of allowing a systematics-free measurement in all directions. In this configuration, the 3 orthogonal OPMs can be operated sequentially in burst mode. Regular salibration of the physics package in scalar FID mode is done regularly.

Feasibility of this concept in practise is assessed. Apart from the PCB coils whose compliance with the sensor homogeneity requirements needs to be verified, all other potential components to realize a prototype have been identified and are either commercially available or can be, as the vapor-cell for example, manufacture.

A preliminary SWaP was derived and promisingly shown to be close or below the sum of the required SWaPs for two separate scalar of vector OPMs. Ideas for reducing the SWaP have already been suggested.

Finally, a roadmap is proposed to reach TRL 7 by 2032.

6 ANNEXES

6.1 List of consortium meetings and keys results

In the following table, the consortium meetings and key results are summarized.

Date	Key results / discussions
12.11.2024	**Kick-off meeting**
12.12.2024	Presentation by ICFO on OPM technologies. Technology is reviewed and discussed.
26.02.2025	Presentation by GFZ on earth observation of magnetic field
19.02.2025	Discussion on the SOA results from ICFO and GFZ Decision to generate common definitions for the project (section 2.1.1) to facilitate the understanding of each-other's vocabulary for specialists coming from different fields
03.04.2025	**MTR review**
25.04.2025	Vector-only OPM scenario is discussed but quickly discarded: no current source is as stable as 12ppm/20 years. Three scenarios: 1) add separate scalar OPM, 2) add separate current reference with He, 3) dual-use physics package. Influence of deadtimes for solution n°3 is immediately raised and discussed. GFZ is tasked to evaluate maximum allowed deadtimes. CSEM and ICFO are tasked to evaluate how fast one could change from one regime to another.
09.05.2025	Technology for vector OPM – zero field nulling – is chosen. ICFO presents principle and expected performances. Issue of vector light-shift mentioned and discussed. GFZ provides simulations about maximum allowed deadtimes in sequential scalar-vector scenario. Approach seems feasible; efforts will be directed in this direction.
23.05.2025	First high-level design of dual-use OPM is proposed with only one axis. Influence of vector light-shift and requirements on laser frequency stability and buffer-gas filling accuracy are presented. First rough SWaP estimate.
16.06.2025	Challenges of ZFN vector OPM are discussed again. CSEM estimates that buffer-gas filling accuracy requirement is hard to meet. Discussion about on-ground calibration of buffer-gas shift is made to circumvent this problem. Still one axis.
20.06.2025	Early CAO model for OPM is presented following discussed high-level design. Still one axis.
27.06.2025	Decision to have three orthogonal cavities as solution to remove systematics. ICFO presents viable 3-axis recalibration process. Final architecture decided.
15.08.2025	Discussion about how to address ESA's preliminary remarks
09.09.2025	**FR meeting**